Parametric Optimization of Inductively Driven Liner Compression Driver System

Akihisa Shimazu

A thesis submitted in partial fulfillment of the
requirements for the degree of

Master of Science in Aeronautics & Astronautics

University of Washington

2016

Reading Committee:

John Slough, Chair

Richard Milroy

Program Authorized to Offer Degree:
Aeronautics & Astronautics

University of Washington

Abstract

Parametric Optimization of Inductively Driven Liner Compression Driver System

Akihisa Shimazu

Chair of the Supervisory Committee:
Professor John Slough
William E. Boeing Department of Aeronautics & Astronautics

The performance of an Inductively Driven Liner Compression (IDLC) driver system for the Fusion Driven Rocket (FDR) application is optimized in this study by performing a parametric analysis of the IDLC driver configurations. The FDR is a novel concept developed by MSNW LLC, which directly converts fusion energy into propulsive energy, where the fusion energy is produced by an inductively driven metal liner compression of a Field Reversed Configuration (FRC) plasmoid. To identify the optimum system configuration for the IDLC driver system for the FDR, a 1D liner code is developed in this study to run different test configuration cases and to identify the optimum system configuration. The results from the 1D liner code is verified against a commercial SPICE circuit solver and a commercial explicit structural dynamics code to verify that the 1D liner code correctly captures the essential liner dynamics for performance tuning. The parametric analysis results from the 1D liner code showed that the IDLC driver system prefers higher voltage to capacitance for a fixed capacitor bank energy. A slightly negative initial seed flux is also seen to improve the liner compression performance. For the optimized design point identified in this study, an energy coupling between the liner kinetic energy and the bank capacitive energy of 69 % is obtained for a fixed capacitor bank energy of 1.8 MJ.

TABLE OF CONTENTS

LIST OF FIGURES

Figure Number Page

LIST OF TABLES

Chapter 1

INTRODUCTION

Nuclear fusion is often considered as a next generation advanced energy source for both terrestrial and space uses. On earth, with increasing demands for clean, cost effective, and abundant energy source, nuclear fusion is often seen as a next generation solution to fix world's upcoming energy crisis. For space, nuclear fusion is seen as a next generation propulsion system that fixes both the energy limit of typical chemical propulsion systems and the power limit of typical electrical propulsion systems [7]. In particular for space, the current physical limits of chemical and electrical propulsion systems restrict human space exploration beyond the earth's sphere of influence.

With the current technology, a manned mission to Mars takes too long. As a result, the entire mission is too costly both for the actual funding of the project and for the astronauts' health. The negative effects of the low gravity environment on the human health have been greatly studied in the past human space programs and have been known to be an issue for missions longer than several months' durations [6]. The potential damages caused by being enclosed in a small spacecraft for many weeks also cannot be neglected in such long manned missions. Furthermore, the risks associated with the space radiation environment cannot be neglected in long manned missions [5].

All of the negative effects discussed in the previous paragraph can be significantly reduced, if the mission time is short. For example, with the current technology, a one-way trip to Mars takes approximately 180 to 240 days [5]. This calls for a total round trip mission transit time of approximately 400 days. If the total mission time can be reduced to half, then the mission time is approximately equal to the typical time that the astronauts current spend in the International Space Station (ISS) in a one tour. The feasibility of such a mission is much greater than the potential 400 day trip to Mars, since it has already been demonstrated in the ISS that humans can spend several months in space without fatally damaging their bodily functions.

Since fusion has both high specific power and high specific energy, the typical power supply penalty experienced in the electric propulsion systems can be avoided [7]. However, the conventional approaches to fusion energy, the magnetic confinement fusion and the inertial confinement fusion, has significant challenges for an application in space propulsion. For the magnetic confinement fusion, the confinement device tends to be very large and massive (e.g. ITER), which is ill suited for the space application, where the launch cost per mass from earth is very high. For the inertial confinement fusion, again, the facility tends to be very massive due to the requirement for large and precise laser system (e.g. National Ignition Facility). The efficiency of the lasers is also generally small, making it unattractive for space propulsion uses.

There are a third path to fusion, which is more suitable for space applications, called magneto-inertial confinement fusion, which combine both the magnetic and the inertial confinement fusion concepts. Addition of the two confinement schemes can greatly reduce the thermal transport loss, due to creation of a magnetic buffer insulation. The magneto-inertial system generally operates at a higher density than the magnetic confinement fusion, which allows for a more compact system. Furthermore, due to the improved thermal insulation, magneto-inertial systems do not require as high of a plasma density as the inertial confinement system, allowing for operations without the use of inefficient lasers.

1.1 Fusion Based on Inductively Driven Liner Compression

One such magneto-inertial confinement fusion concept that is applicable for space use is the concept of a fusion based on an inductive driven liner compression (IDLC) where a thin metallic cylindrical shell (liner) is inductively compressed (imploded) on to a Field Reversed Configuration (FRC) plasmoid. The implosion of the liner compresses the magnetic flux confined by the liner cross-section, increasing its magnetic field. The increased magnetic field value together with additional confinement offered by the liner inertia allow the FRC to compress down to a fusion condition.

The dynamics of the liner is approximately governed by the force balance of the magnetic pressure, where

$$m_l \frac{d^2 r}{dt^2} = 2\pi r w \left(\frac{B_{in}^2}{2\mu_0} - \frac{B_{out}^2}{2\mu_0} \right) \tag{1.1}$$

where m_l is the liner mass, w is the liner axial length, B_{in} and B_{out} are the magnetic field inside and outside the liner, respectively, and r is the liner mean radius [17]. The imbalance in the magnetic pressure produces an implosion effect of the liner and allows transfer of the magnetic inductive energy to the liner kinetic energy.

The liner kinetic energy is eventually converted into a compressional work on the FRC that is injected inside the converging liners. The compressional work on the FRC from the liner allows the FRC to reach fusion conditions and produce fusion energy. Under the assumptions of (1) adiabatic scaling laws for the FRC dynamics, (2) the FRC energy being dominated by the pressure balance with the edge magnetic field at the peak compression, (3) the liner dwell time being $2r_0/v_l$ where r_0 is the liner final radius and v_l is the liner peak velocity, and (4) the optimum D-T fusion cross section of $\langle \sigma v \rangle = 1.1 \times 10^{-31} \mathrm{T}^2$, one can derive a rather simple relationship for the estimated fusion gain for the IDLC fusion concept to be

$$G \approx 4.3 \times 10^{-8} \sqrt{m_l} E_l^{11/8} \tag{1.2}$$

where E_l is the peak liner kinetic energy [17].

Using this approach for fusion, a concept for a fusion based space propulsion system has been developed by MSNW LLC and it is named the Fusion Driven Rocket (FDR). The key features of the FDR is a direct conversion of the fusion energy to the propulsive jet energy. In the next section, the proposed FDR concept is discussed.

1.2 The Fusion Driven Rocket

The Fusion Driven Rocket (FDR) is a fusion propulsion concept that implements the IDLC fusion concepts for the direct conversion of the fusion energy to the propulsive energy. The schematics of the FDR operational sequence is shown in Fig. 1.1 to illustrate the basic operational principle of the FDR. Thin liners are driven independently at an angle to allow for an uniform liner convergence at the thruster throat. The FRC plasmoid is created and injected separately to merge with the converging liners and to be captured by the liner implosion. The inertia of the imploding liner sufficiently compresses the captured FRC, such that the FRC can reach fusion conditions. The fused FRC releases fusion energy, and it heats and vaporizes the liner metal in the magnetically insulated nozzle. The hot exhaust from the fusion process is then expanded in the magnetically insulated nozzle to convert thermal fusion energy directly to propulsive kinetic energy [17].

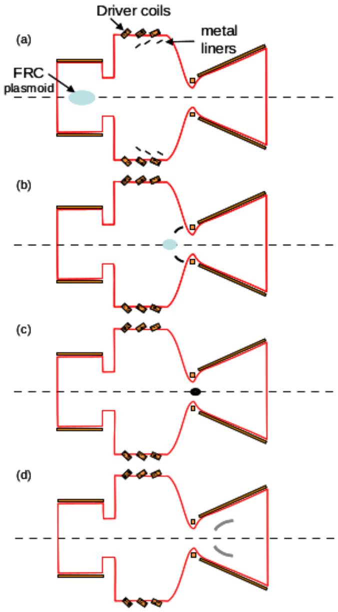

Figure 1.1: Schematic of the Fusion Driven Rocket operation sequence (from Ref [17]).

One of the most advantageous feature of the FDR is the direct conversion of fusion thermal energy to directed propulsive kinetic energy in the magnetically insulated nozzle. This is very similar in operation to typical chemical based rockets, where the hot exhaust from the chemical reaction process is converted to directed kinetic energy through a nozzle. While the conversion efficiency of the magnetically insulated nozzle is still limited by the usual frozen flow losses, additional energy conversion processes are avoided to both simplify the thruster system and to minimize the conversion losses [17].

The key in improving the performance of the FDR is to improve the efficiency of the energy coupling in the IDLC driver system. Understanding and being able to evaluate the liner compression behavior is a key in the accurate prediction of the FDR performance. The improved energy coupling is also important to make the FDR thruster compact for space applications. This paper will study and parametrically optimize the IDLC driver system for the proposed FDR concept.

Chapter 2

THEORY OF INDUCTIVELY DRIVEN LINER COMPRESSION

2.1 Introduction

The inductively driven liner compression (IDLC) process takes advantage of the physics of the magnetic flux compression (also called the magnetic cumulation), where a magnetic flux is trapped inside a hollow conductor while the conductor cross-section changes. Using the definition of the magnetic flux

$$\Phi = \int_S \mathbf{B} \cdot d\mathbf{S} \tag{2.1}$$

where Φ is the magnetic flux, $\mathbf{B}$ is the magnetic field, and $\mathbf{S}$ is the conductor cross-section, if a constant magnetic flux is trapped in the conductor while the conductor cross-section decreases, then the magnetic field must increase. This effect is a result of Lenz's law, where an induced current is generated to resist the change of the initial flux value. The induced current continues to prevent the flux from leaking for the resistive decay time of the induced current. Thus, if the change in the cross-section of the conductor occurs faster than the resistive decay time of the conductor, then a high magnetic field value can be obtained from the initial seed flux trapped in that conductor cross-section.

The ability to obtain high magnetic field values through magnetic flux compression processes has been known to be possible since 1940's. In late 1940's and early 1950's, in both the USA and Russia, magnetic flux compression systems had been tested successfully using explosives as a compressional energy source for imploding metallic liners with initial seed magnetic flux [8]. It was not until the 60's with pioneering work of Cnare in the USA (ref [3]) and of Alikhanov in Russia (ref [1]), that electromagnetic approaches without the use of explosives was tested. Cnare studied the inductive method extensively, while

Alikhanov instead pursed a z-pinch like approach after some initial tests using the inductive method [14]. In recent years, Canre's inductive method has been successfully applied in high magnetic field experiments in solid states physics. In Japan, Miura has successfully developed a semi-nondestructive high magnetic field materials testing facility using Cnare method and succeeded in obtaining fields exceeding 500 T [11]. In later experiments, an indoor nondestructive magnetic field record of 600 T was obtained by Matsuda [9], and later, it was succeeded again by a record field approaching 730 T by Takeyama [20].

2.2 Physics of Inductively Driven Magnetic Flux Compression

The inductively driven magnetic flux compression is a consequence of Lenz's law. In the inductively driven magnetic flux compression system, one has a main driver coil, which is connected to the main capacitor bank. Inside the driver coil, a thin metallic cylinder (liner) is placed. The capacitor bank is then fired, producing a mega-ampere current through the driver coil. Due to Lenz's law (which is a consequence of Faraday's Law), a large induced current flows in the liner, shorting out the driver coil and causing a development of a high magnetic field between the liner and the driver coil. The liner experiences high magnetic pressure which causes it to collapse rapidly inwards, compressing any magnetic flux that is present inside the liner. The inertia of the liner continues to implode the liner radially inward, causing the magnetic flux inside the liner to be compressed, until the liner eventually comes to rest due to the increasing magnetic pressure inside the liner.

One can characterize the liner implosion process as a circuit model, to estimate the implosion process from energy based models. Based on a simplified theory by Knoepfel, one can define the total time dependent inductance of the coil-liner system as

$$L(t) = L_c(t) + L_L \tag{2.2}$$

where $L_c(t)$ is the time dependent compression inductance and L_L is the load inductance [8].The inductive compression process can be modeled as a consequence of the time dependent change in the compression inductance. In a more detailed circuit model for the inductively driven liner compression process, one can define a mutual inductance between the driver coil and the liner, and model the implosion process as a change in the coupling between the driver coil and the liner.

2.3 Stages of Liner Implosion

The liner implosion process can be loosely divided into three phases: acceleration, coasting, and deceleration. The acceleration phase is when the liner is initially being accelerated by the magnetic field pressure in the shorted region. The liner is highly coupled to the driver coil in this phase, and the performance of the initial launch of the liner strongly dictates the later behavior of the liner dynamics. This phase is most critical for converting the capacitive energy stored in the capacitor bank to the liner kinetic energy due to the large coupling.

The coasting phase of the liner implosion occurs when the shorted magnetic field decays to a negligible magnetic pressure. This occurs after the liner has moved off far enough away from the driver coil wall such that the coupling between the liner and the driver coil is small. In the coasting phase, the liner velocity is approximately constant, as the magnetic field in neither inside nor outside liner section is large enough to change the liner motion. Thus, it is the inertia of the liner and the initial acceleration that dictates the behavior of the liner in this phase.

Finally, the deceleration phase occurs when the liner is being stopped due to a rapid increase in the magnetic field of the liner's inner region when the final magnetic flux compression occurs. A high heating takes place in the liner inner surface, as a large surface current flows on the liner surface because of the large magnetic field gradient. There is a large magnetic diffusion in this phase, as the magnetic field penetrates into the metal liner itself. The phenomena of liner deceleration and stopping (bounce) are heavily influenced by the material property of the liner, namely the compressibility and the electrical conductivity.

Chapter 3

THE 1D LINER CODE

3.1 Introduction

To optimize the system design of the Inductively Driven Liner Compression (IDLC) driver system, a model that captures the important physics of the liner implosion dynamics is required. At the same time, this model must also incorporate the driver circuit associated with the capacitor bank that is fired to drive the liner compression. Furthermore, the model must also be computationally cheap, such that many parametric design points can be ran in relatively short amounts of time, to serve as a first order design tool to aid in the future designs of the IDLC driver system.

In order to meet these design goals, a pseudo-1D model for the liner implosion dynamics is coupled with a circuit solver to capture the full IDLC driver system behavior. The driver circuit, magnetic field, Joule heating, and liner dynamics calculations are performed at each time step in sequence to couple these effects into the code. A 1D incompressible model is used for the liner dynamics to reduce the computational cost, while capturing the key dynamic behavior of the imploding liner. To obtain a more realistic magnetic field for a given driver coil geometry, 2D and 3D effects are incorporated into the 1D field calculation through the use of a correction factor table lookup approach.

Similar 1D approach to the modeling of the IDLC driver system has been used successfully in the past to analyze the behavior of the liner implosion process with a decent agreement to the experimental results [15,17]. However, in the previous work, an infinitely long cylindrical model was used in the magnetic field calculation, which resulted in an over approximation of the efficiency of the liner driver system. This effect was especially pronounced for a hoop-like liner with a large radius compared with its height. The energy conservation was also not strictly enforced in the coupling of the circuit and the coil-liner system calculation in the previous work.

The present model attempts to fix these short coming by enforcing a stricter energy conservation between the coupled solvers and by using a correction factor approach to the 1D calculation to retain the computational advantage of the 1D model, while correcting for some 2D and 3D geometric effects. This allows the code to not require a full 2D or 3D magnetic field calculation at each time step, which is computationally expensive since the domain must be re-meshed every time the liner geometry changes significantly. By pre-tabulating the approximate magnetic field correction required at each liner geometries, some geometric effects can be captured, while taking advantage of the fast 1D calculations.

The results from the functional earlier version of the present code has been published in the past, and the code has been used successfully to optimize the design of the possible next step verification experiment for the fusion driven rocket [13, 18]. The details of the solver routine for the earlier version of this code can be found in the appendix of ref [18]. The earlier version of this code had an issue with under-predicting the performance and the efficiency of the driver circuit, due to a more conservative model for energy transfer process by the circuit to the coil-liner system. This short coming is fixed in the present version of the 1D liner code. The description of the most recent implementation of the 1D liner code is given in this chapter.

3.2 Overview of the 1D Liner Code

The 1D liner code is designed to take advantage of more advanced commercially available solvers to add 2D and 3D corrections and to serve as a verification tool. How the 1D liner code couples with external data and external solvers are illustrated in Fig. 3.1. To obtain the field, flux, and inductance data for the coil-liner magnetic field calculation, ANSYS Maxwell 3D® solvers is used. To verify the liner dynamics, the pressure loads predicted by the 1D liner code is input into ANSYS Explicit Dynamics® solver to verify that the liner dynamics computed by the 1D liner code agrees with the liner implosion dynamics computed by the commercial explicit dynamics solver, which accounts for the losses associated with the internal mechanical energy and the plastic deformations. A commercial SPICE solver is used to verify the 1D liner circuit solver.

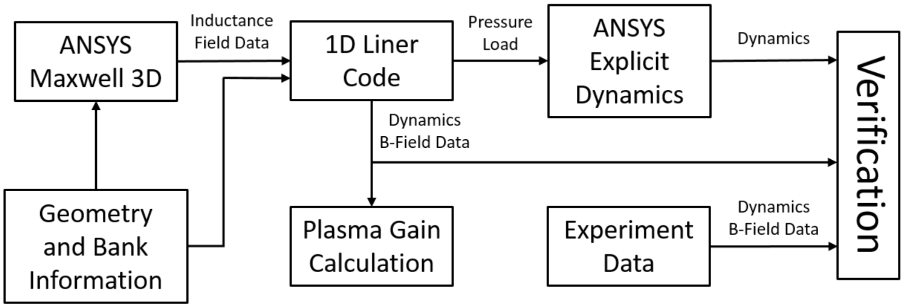

Figure 3.1: Coupling of the 1D liner code with external data and solvers

The flowchart of the implemented 1D liner code is shown in Fig. 3.2. It is important to note that the 1D liner code is composed of two solvers coupled together: the circuit solver and the coil-liner system internal calculations. Two solvers are coupled together in an energy conserving manner to enforce a global energy conservation. The details of the implementation for the various section of the code is discussed in the subsequent sections.

3.3 The Circuit Model

The capacitor bank system and the associate driver circuit is assumed to be an ideal crowbar circuit, where the crowbar switch is closed permanently when the voltage across the switch becomes negative. This circuit system is commonly used in inductively driven liner experiments. In a real experiment, crowbar switch is triggered at some predetermined time, but generally, the exact timing is determined a priori to achieve a condition close to the ideal crowbar condition. Thus, modeling the driver circuit as an ideal crowbar circuit should predict a condition close to the real experiment. The circuit diagram of the ideal crowbar circuit used in the code is shown in Fig. 3.3.

In Fig. 3.3, the stray resistances associated with the capacitor bank, switches, and cables

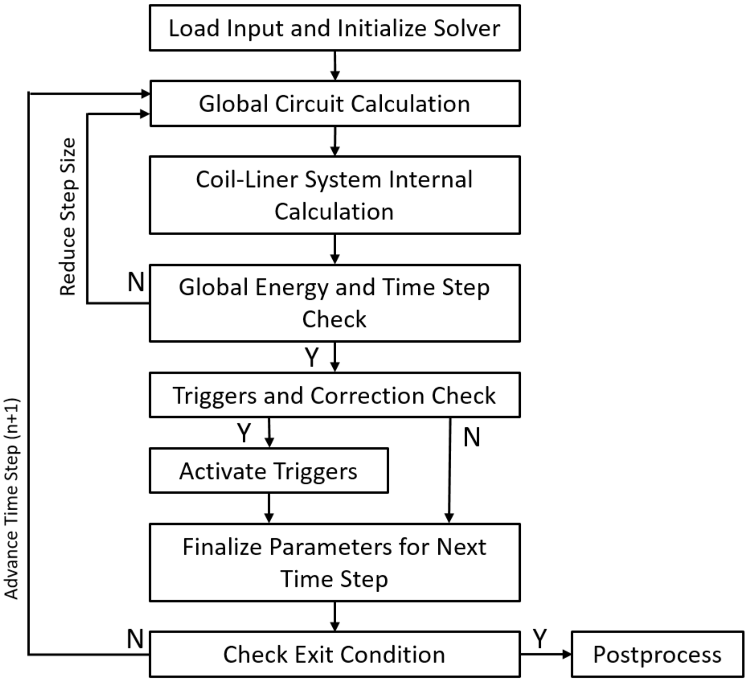

Figure 3.2: Flowchart of the 1D Liner Code.

are captured in R_1, R_2, and R_3, and the stray inductances in L_1, L_2, and L_3. The Stray capacitance is neglected in the circuit calculation, since the capacitance of the bank, C, typically dominates the circuit capacitive behavior. The coil-liner system is modeled as a resistor (R_{sys}) and an inductor (L_{sys}) in series. The effective inductance of the coil-liner system is used for circuit calculation, which in the limit of the flux conserving liners is equivalent to the shorted inductance of the coil. Since the liner dynamics will alter the geometry and the energy loss rate of the coil-liner system, both the system inductance and resistance are time dependent quantities such that

$$L_{sys} = L_{sys}(t) \tag{3.1}$$

$$R_{sys} = R_{coil} + R_{an}(t) \tag{3.2}$$

where R_{coil} is the static resistance associated with a current flow through the driver coil and

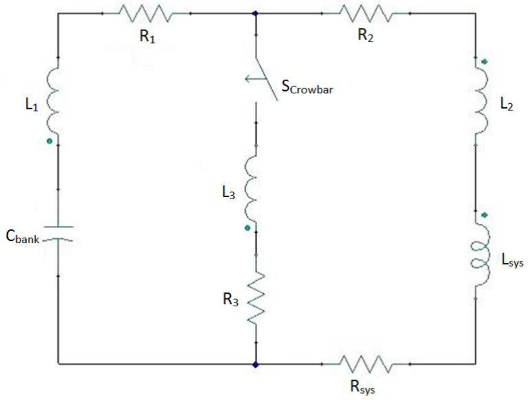

Figure 3.3: Circuit diagram of the crowbar circuit used in the code.

R_{an} is the time dependent resistivity associated with a circuit energy loss due to the internal dynamics of the coil-liner system. R_{an} serves as a coupling coefficient between the 1D liner dynamics solver and the circuit solver to satisfy the global energy conservation.

Since the system inductance is approximately equal to the shorted inductance of the driver coil, it is assumed that the coil-liner system inductance is only a function of the liner outer radius. Using this assumption, the effective inductance of the coil-liner system can be tabulated a priori through the actual inductance measurement of the driver coil or through the use of a low-frequency electromagnetic solver for the different coil-liner geometry. Thus, the effective system inductance can be obtained simply through a table lookup approach in the execution of the code. The latter approach using a low-frequency electromagnetic solver is used to compute the effective coil-liner system inductance in this work, and a commercial low-frequency electromagnetic field solver called ANSYS Maxwell 3D$^{®}$ is used. The details on calculating system inductance are discussed later in this chapter.

To solve the ideal crowbar circuit, Kirchhoff's circuit laws are used. In Fig. 3.3, defining I_1 as the current flowing through the capacitor bank section in a clockwise direction, I_2 as the current flowing through the coil-liner system in a clockwise direction, I_3 as the current flowing through the crowbar switch in an upward direction, and V_c as the capacitor bank voltage, when the crowbar switch is open, the dynamics of the circuit is described by the following four equations:

$$I_3 = 0 \tag{3.3}$$

$$I_2 = I_1 \tag{3.4}$$

$$V_c = V_0 - \frac{1}{C}\int_0^t I_1\, dt \tag{3.5}$$

$$V_c = R_1 I_1 + L_1 \frac{dI_1}{dt} + (R_2 + R_{sys}) I_2 + L_2 \frac{dI_2}{dt} + \frac{d(L_{sys} I_2)}{dt} \tag{3.6}$$

where V_0 is the initial capacitor bank voltage.

The above equations are solved using a forward time difference method as

$$I_1^n = I_2^n = \frac{V_c^{n-1}\Delta t + I_1^{n-1} L_{tot_1}}{(\Delta t)^2/C + R_{tot}\Delta t + 2L_{tot_1} - L_{tot_2}} \tag{3.7}$$

$$V_c^n = V_c^{n-1} - \frac{I_1^n \Delta t}{C} \tag{3.8}$$

where the superscript n indicates the value at the present time step, and

$$R_{tot} = R_1 + R_2 + R_{sys}^{n-1} \tag{3.9a}$$

$$L_{tot_1} = L_1 + L_2 + L_{sys}^{n-1} \tag{3.9b}$$

$$L_{tot_2} = L_1 + L_2 + L_{sys}^{n-2} \tag{3.9c}$$

When the crowbar switch is closed, the dynamics of the circuit is now described by the following four equations:

$$I_3 = I_2 - I_1 \tag{3.10}$$

$$V_c = V_0 - \frac{1}{C}\int_0^t I_1\, dt \tag{3.11}$$

$$V_c = R_1 I_1 + L_1 \frac{dI_1}{dt} + (R_2 + R_{sys}) I_2 + L_2 \frac{dI_2}{dt} + \frac{d(L_{sys} I_2)}{dt} \tag{3.12}$$

$$0 = (R_2 + R_{sys}) I_2 + L_2 \frac{dI_2}{dt} + \frac{d(L_{sys} I_2)}{dt} + R_3 I_3 + L_3 \frac{dI_3}{dt} \tag{3.13}$$

Similar to the previous case, the above equations are solved using a forward time difference method as

$$I_1^n = \frac{A_{22}b_1 - A_{12}b_2}{A_{11}A_{22} - A_{12}A_{21}} \tag{3.14}$$

$$I_2^n = \frac{A_{11}b_2 - A_{21}b_1}{A_{11}A_{22} - A_{12}A_{21}}; \tag{3.15}$$

$$I_3^n = I_2^n - I_1^n; \tag{3.16}$$

$$V_c^n = V_c^{n-1} - \frac{I_1^n \Delta t}{C} \tag{3.17}$$

where

$$A_{11} = -R_3\Delta t - L_3 \tag{3.18a}$$

$$A_{12} = (R_2 + R_3 + R_{sys}^{n-1})\Delta t + L_2 + L_3 + 2L_{sys}^{n-1} - L_{sys}^{n-2} \tag{3.18b}$$

$$A_{21} = \frac{(\Delta t)^2}{C} + R_1\Delta t + L_1 \tag{3.18c}$$

$$A_{22} = (R_2 + R_{sys}^{n-1})\Delta t + L_2 + 2L_{sys}^{n-1} - L_{sys}^{n-2} \tag{3.18d}$$

$$b_1 = (L_2 + L_3 + L_{sys}^{n-1})I_2^{n-1} - L_3 I_1^{n-1} \tag{3.18e}$$

$$b_2 = V_c^{n-1}\Delta t + L_1 I_1^{n-1} + (L_2 + L_{sys}^{n-1})I_2^{n-1} \tag{3.18f}$$

To ensure that the energy is conserved between the circuit solver and the coil-liner system calculation, the circuit energy is calculated at the end of the circuit solver. In the circuit equation, the energy stored inside the coil-liner system (E_{sys}) is represented by the inductive and the resistive energy of the system components, such that

$$E_{sys}(t) = \frac{1}{2}L_{sys}I_2^2 + \int_0^t \left(\frac{1}{2}\frac{dL_{sys}}{dt} + R_{an}\right) I_2^2\, dt \tag{3.19}$$

where the first term represents the effective static magnetic field energy stored in the coil-liner system, the second term is the dynamic inductance energy component, which accounts for a change in the coil-liner system energy due to a change in the system geometry, and the third term is the coupling term to ensure that the change in the stored energy of the coil-liner system is reflected properly in the circuit calculation. The sum of the first two terms is equivalent to the energy in the coil-liner system driven by Faraday's Law. All other change in the coil-liner system energy is modeled as a resistive term in the circuit. In the coil-liner system internal calculation, R_{an} is determined such that the total energy of the system will be conserved during the liner implosion process.

3.4 Coil-Liner System Internal Calculation

For the internal calculation of the coil-liner system, a simplified 1D model for the coil-liner system is used. The simplified 1D coil-liner system model is shown in Fig. 3.4. The system is divided into a three distinct region: the outer (shorted) region, the inner region, and the liner (solid) region. During the implosion process of the liner, the width (w) of the liner is assumed to be constant (note that width of the liner is modeled to be equal to the width of the driver coil in the figure, but this is not a required condition). Due to the incompressible liner assumption, the outer and the inner radius of the liner (r_{out} and r_{in}) are coupled by the liner volume conservation condition.

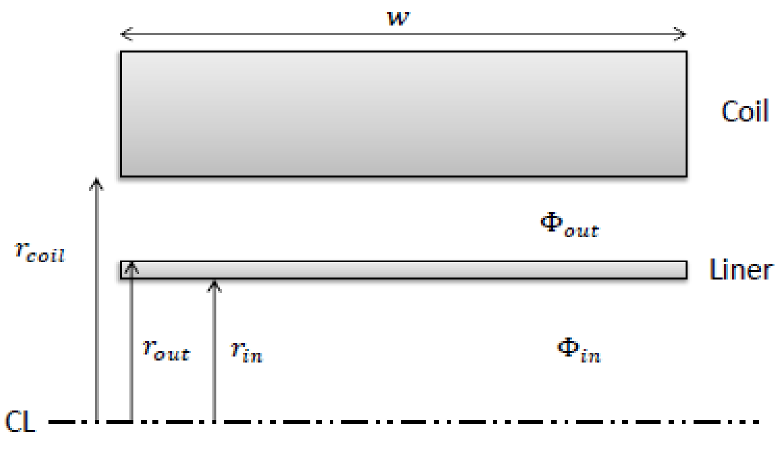

Figure 3.4: Simplified 1D model of the coil-liner system with two distinct regions

A flow chart of the coil-liner system internal calculation steps is shown in 3.5. The details of the each step in the solver is discussed in the subsequent subsections.

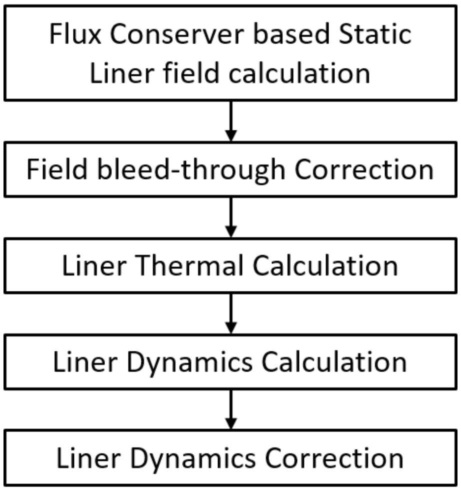

Figure 3.5: A flowchart of the coil-liner system internal calculations

3.4.1 Flux based Calculation

The internal calculation of the coil-liner system is formulated using a flux based approach. This has an advantage such that the dimensionality of the problem is reduced to macroscopic lumped parameters that can be tabulated as a function of the system geometry. Furthermore, since the effective flux through the coil-liner system is what is captured by the circuit calculations, this allows for more direct way to couple the dynamics solver to the circuit solver. The effective magnetic flux injected at any time step can be related to the circuit parameter as

$$\Delta\Phi_{inj} = L_{sys}\Delta I_2 \tag{3.20}$$

To simplify the model, the magnetic flux is assumed to be stored only in the outer and the inner regions. The magnetic flux in the solid region is neglected, since the magnetic flux stored in the liner is small for a majority of the implosion process. The magnetic flux diffusion into the the solid region becomes important as the liner radius decreases, but for a majority of the compression, this effect is negligible. Using the result from Knoepfel, it can be concluded that the assumption of a negligible flux loss into the solid region is valid, if the liner radius is greater than r_{md}, which is defined to be

$$r_{md} = \frac{\kappa_0}{v} = \frac{\eta}{\mu_0 \mu_r v} \tag{3.21}$$

where η is the electrical resistivity, μ_r is the relative permeability, and v is the liner velocity [8]. For most case of interest, r_{md} is small, and the peak liner velocity is obtained before the liner reaches r_{md}. Thus, for the optimization of the energy coupling between the circuit and the coil-liner system, this effect can be safely neglected.

In the flux based calculation, the magnetic flux can be related to the effective 1D magnetic field as

$$\overline{B}_{out}(r,t) = C_A(r,t)\Phi_{out}(t) \tag{3.22}$$

$$\overline{B}_{in}(r,t) = C_B(r,t)\Phi_{in}(t) \tag{3.23}$$

where $\overline{B}_{out}$ and $\overline{B}_{in}$ are the liner width averaged magnetic field in the outer and inner region, respectively. C_A and C_B are the flux-field geometric parameter with unit of T/Wb, which contains the relationship between the magnetic flux and the liner width averaged magnetic field at some radius and time, r and t. Since the flux-field parameter is largely driven by the geometry of the coil-liner system, the temporal dependence of the flux-field parameter can be approximated to be only a function of the liner position such that $C_A(r,t) = C_A(r, r_{liner}(t))$ and $C_B(r,t) = C_B(r, r_{liner}(t))$. Since C_A and C_B are only a function of the liner radius, their values can be tabulated a priori for various liner positions. Interpolation of the tabulated data can be used during the calculation to relate the magnetic field to the magnetic flux, where necessary.

For 1D ideal infinitely long cylinder case, C_A and C_B are constant for some fixed liner position, and it can be evaluated analytically to be

$$C_A(r_{liner}) = \frac{1}{\pi(r_{coil}^2 - r_{liner}^2)} \tag{3.24}$$

$$C_B(r_{liner}) = \frac{1}{\pi r_{liner}^2} \tag{3.25}$$

which are simply the inverse of the cross-sectional area of the outer and inner region, respectively. The factors C_A and C_B are simply an extension of the analytical result in the ideal 1D case to incorporate potential 2D and 3D geometrical effects in the relationship between the magnetic flux and the magnetic field.

3.4.2 Static Liner Calculation

Before the liner dynamics can be calculated, the influence from the driver circuit in the providing magnetic flux must be considered. Using Eq. 3.20, the flux injected by the circuit to the coil-liner system can be evaluated. Since the effective coil-liner system inductance used in the circuit calculation is approximately equal to the shorted inductance of the driver coil, the flux injection process can be approximated as if the liner is a perfect flux conserver and all of the injected flux is added to the shorted region. Since the magnetic field equilibration process occurs on much smaller time scale (governed by the speed of light) than the time scale of the liner motion, the liner can be assumed to be static during the flux injection calculation.

The flux in the shorted region is then

$$\Phi'_{out} = \Phi_{out}^{n-1} + \Delta\Phi_{inj} \tag{3.26}$$

where Φ'_{out} is the new shorted magnetic flux after the flux injection. The new magnetic field on the outer region can also be calculated using the geometric relationship parameter as

$$B'_{out} = C_A^{n-1}\Phi'_{out} \tag{3.27}$$

3.4.3 Flux Diffusion Correction

Due to the finite resistivity of the liner, the liner will not behave exactly as a perfect flux conserver as assumed in the previous subsection, and instead, allows a finite bleed-though (diffusion) of magnetic flux to the inner region, due to the resistive decay of the induced current at the interface. Thus, the magnetic flux in the two region must be corrected to account for the flux bleed-through phenomena.

If the liner is assumed to be thin and long and if the current density is assumed to be constant in the liner, a general solution for the magnetic diffusion can be obtained. Using the result from Knoepfel, the diffusion of the magnetic field through the liner can be approximated to be

$$\tau_B \frac{dB_{in}}{dt} = B_{out} - B_{in} \tag{3.28}$$

where τ_B is the magnetic diffusion time, and magnetic fields are measured at the liner interface [8]. For the case when the liner is very long, the magnetic diffusion time constant can be calculated analytically, and it is calculated by Knoepfel to be

$$\tau_B = \frac{\mu_0 r_0 \delta}{2\eta} \tag{3.29}$$

where r_0 is the liner mean radius, δ is the liner thickness, and η is the electrical resistivity of the liner [8].

Re-organizing this simple result for the 1D infinitely long cylinder case, it can be shown that

$$\tau_B = \frac{w\delta}{2\pi r_0 \eta} \frac{\mu_0 \pi r_0^2}{w} = \frac{L_{liner}}{R_{liner}} \tag{3.30}$$

where the last expression is obtained by using the analytical expression for the inductance and the resistance of a long thin cylinder with a length w. It can be concluded from this simple 1D result that for the case of thin liner, the magnetic field diffusion is governed by the L/R time constant of the liner. Physically, since the current in the liner is induced and driven by the gradient in the magnetic field (inductive effect) and the magnetic field penetration through the liner is driven by the finite liner resistance (resistive effect), it is expected that the current decay and the magnetic field diffusion is governed by the inductive time scale. Thus, the simple expression derived by Knoepfel for thin long liner can be extended for shorter liners by the use of L/R time constant rather than the simpler result given by Knoepfel.

Using the flux-field parameter, the statement for the diffusion of magnetic fields can be converted into an expression for the magnetic flux bleed-through correction. After application of the finite differencing, at some time step n, if $B'_{out} > B_{in}^{n-1}$, the bleed-through flux is

$$\Delta\Phi_B = \frac{\Delta t}{\tau_B C_A^n(r_{out})} \left[B'_{out}(r_{out}) - B_{in}^{n-1}(r_{in})\right] \tag{3.31}$$

since the shorted region is driving the bleed-through phenomena, while if $B'_{out} < B_{in}^{n-1}$, the bleed-through flux is

$$\Delta\Phi_B = \frac{\Delta t}{\tau_B C_B^n(r_{out})} \left[B'_{out}(r_{out}) - B_{in}^{n-1}(r_{in})\right] \tag{3.32}$$

since the inner region is driving the bleed-through phenomena. After the bleed-through correction, the magnetic flux in the inner and the outer region of the coil-liner system can be expressed as

$$\Phi_{out}^n = \Phi'_{out} - \Delta\Phi_B \tag{3.33}$$

$$\Phi_{in}^n = \Phi_{in}^{n-1} + \Delta\Phi_B \tag{3.34}$$

and the effective magnetic field magnitude can be computed to be

$$B''_{out} = C_A^{n-1}\Phi_{out}^n \tag{3.35}$$

$$B'_{out} = C_B^{n-1}\Phi_{in}^n \tag{3.36}$$

3.4.4 Thermal Calculation

Since a finite resistivity of the liner is assumed, the ohmic energy loss in the liner due to Joule heating must be accounted. Assuming a thin liner, since the current flowing through the liner is driven by the gradient in the magnetic field at the interface, from Ampere's Law, the liner current can be calculated to be

$$I_{liner} = \frac{w}{\mu_0}\left[B''_{out}(r_{out}) - B'_{in}(r_{in})\right] \tag{3.37}$$

and the resulting Joule heating loss in the liner is then calculated for the given time step to be

$$\Delta U^n_{th} = R^n_{liner}\left(I^n_{liner}\right)^2 \Delta t \tag{3.38}$$

Since for most conductor, the ratio of the electrical skin depth to the thermal skin depth (δ_{el}/δ_{th}) is much greater than unity [8], the effect of the thermal conduction can be neglected in the calculation of the temperature increase in the liner due to Joule heating effect. Thus, a locally adiabatic approximation can be used to calculate the heating of the liner due to the induced liner current. The temperature increase is calculated as

$$\Delta T^n = \frac{\Delta U^n_{th}}{c_v m_h} \tag{3.39}$$

where c_v is the specific heat at a constant volume and m_h is the heated mass of the liner. Since the current density in the liner has $\mathrm{e}^{-r/\delta_{el}}$ dependence and since Joule heating goes as the current squared, the heated mass of the liner is approximately governed by the heat penetration depth $2\delta_{el}$. If the liner thickness is smaller than the heat penetration depth, then the heated mass is the total mass of the liner. If the liner thickness is greater than the heat penetration depth, then the heated mass is the mass of the liner with thickness equal to the heat penetration depth. When the temperature reaches the melting point of the material, then the energy from Joule heating is converted into a latent heat, rather than to increase the liner temperature, until the phase transition completes.

Since resistivity of the liner is a function of the liner temperature, from the calculated temperature of the liner, the resistivity of the liner at the updated condition is calculated. For most conductors, the temperature dependence of the electrical resistivity is approximately linear for one phase condition, and it discontinuously jumps when the liner transitions into a difference phase. While empirically measured constants exist for relationship between the conductor temperature and the resistivity for many common materials, a table lookup and interpolation approach is used in the code to calculate the temperature dependent resistivity of the liner. The data for the temperature dependent resistivity for various conductors are shown in Fig. 3.6.

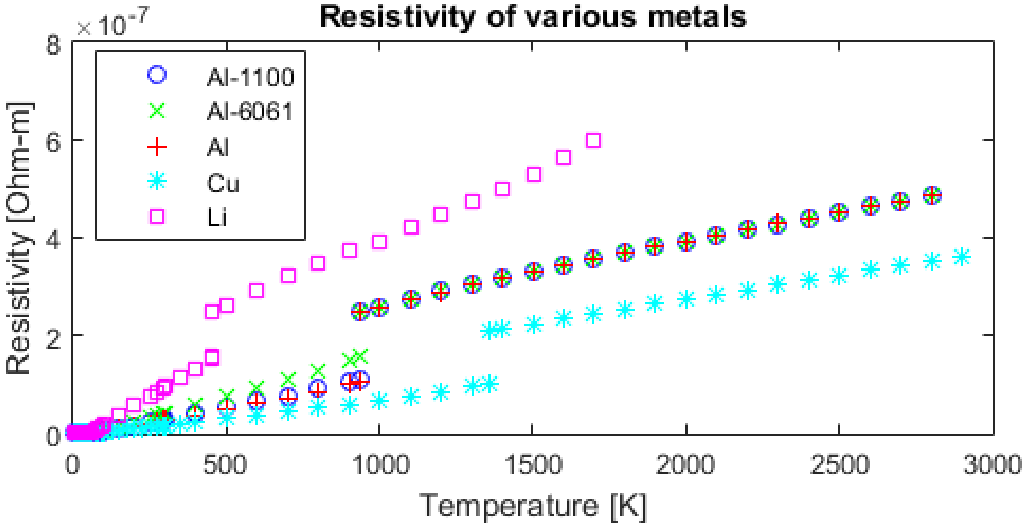

Figure 3.6: Resistivity of various conductors. Resistivity data are obtained from ref [2] for Lithium, ref [10] for Copper, and ref [4] for aluminum. Data for Al-1100 and Al-6061 is obtained from scaling the resistivity data of the pure aluminum to match the room temperature resistivity of these aluminum alloys.

3.4.5 Liner Dynamics Calculation

If the liner is assumed to be a volume conserving fluid with no axial deformation and no internal mechanical impedance, the dynamics of the liner implosion can be approximated as

$$m_l \frac{dv_l}{dt} = 2\pi w \left(\frac{B_{in}^2 r_{in}}{2\mu_0} - \frac{B_{out}^2 r_{out}}{2\mu_0} \right) \tag{3.40}$$

$$\frac{dr_l}{dt} = v_l \tag{3.41}$$

where m_l is the liner mass, v_l is the liner velocity, and r_l is the liner radius. Since the edge effects are neglected, the liner dynamics are driven purely by the net radial force exerted by the imbalance of the magnetic pressure at the liner interface.

Using a first order explicit discretization, the previous expression becomes

$$v_l^n = v_l^{n-1} + \frac{\pi w \Delta t}{\mu_0 m_l} \left[(B''_{out})^2 r_{out}^n - (B'_{in})^2 r_{in}^n \right] \tag{3.42}$$

$$r_{out}^n = r_{out}^{n-1} - v_l^n \Delta t \tag{3.43}$$

where the substitution $r_l \approx r_{out}$ is made from the assumption that the liner thickness is small compared with the outer radius of the liner. The approximation where $r_l \approx r_{out}$ can be obtained from the definition of r_l:

$$r_l = \frac{2}{3} \left(\frac{r_{out}^3 - r_{in}^3}{r_{out}^2 - r_{in}^2} \right) = \frac{2}{3} \left[\frac{1 - (1 - \delta/r_{out})^3}{1 - (1 - \delta/r_{out})^2} \right] r_{out} \tag{3.44}$$

and the liner volume conservation condition

$$V_l = \pi w (r_{out}^2 - r_{in}^2) = \pi w r_{out}^2 (1 - \delta/r_{out})^2 = \text{Const.} \tag{3.45}$$

Assuming the limit where $\delta/r_{out} \gg 1$, then a binomial expansion can be used to prove that $r_l \approx r_{out}$.

Once the new liner outer radius is known, r_{in}^{n} and δ can be solved from the liner volume conservation condition. Once the new geometry of the coil-liner system is obtained from the dynamic calculations, values of L_{sys}, L_{liner}, C_A, and C_B can be computed from a table lookup.

3.4.6 Liner Dynamics Correction

Due to the dynamic motion of the liner, the coil-liner system property must be corrected to ensure an internal energy conservation in this time step. In the coil-liner system, the main reservoir of energy is the magnetic field energy in the outer and the inner region (E_{out} and E_{in}, respectively), the kinetic energy of the liner (E_{KE}), and the energy lost to the internal energy of the liner (E_l). In each time step, sum of the change in the energy must be exactly balanced by the energy injected into the system by the circuit calculation (E_{sys}) to ensure that the global energy conservation is enforced between the two coupled solver.

When the change in the kinetic energy of the liner is positive, then it is the circuit that is driving the change in the kinetic energy of the liner (through magnetic field in the shorted region). Thus, the increase in the kinetic energy must be balanced by the energy associated with the dynamic inductance or through the coupling resistance R_{an}. Since R_{an} is the only free coupling parameter, this value must be adjusted accordingly to ensure energy conservation at each time step.

On the other hand, when the change in the kinetic energy of the liner is negative, then the circuit no longer governs the motion of the liner implosion. Rather, it is the magnetic field in the internal region which governs the liner dynamics. Thus, under this condition, a contribution to the coupling resistance R_{an} by the kinetic energy becomes zero, since the circuit is no longer coupled to the liner motion. As a result, any change in the kinetic energy of the liner must be balanced either by a decrease in the magnetic field energy of the inner region (through flux decay) or by an increase in the liner internal energy.

Similar to the kinetic energy, the coupling of the Joule heating loss in the liner to the circuit is also governed by the coil-liner system condition. If the field in the outer region is greater than that of the inner region, then it is the bleed-through of the magnetic field from the outer region that governs the induced current in the liner. Thus, the Joule heating loss in the liner is coupled directly to the circuit, and the coupling resistance R_{an} must be modified to ensure the global energy conservation. On the other hand, if the field in the inner region is greater than that of the outer region, then it is the bleed-through of the magnetic field from the inner region that governs the induced current in the liner. Thus, the Joule heating loss in the liner must be balanced by a decrease in the magnetic field energy of the inner region or by a decrease in the liner kinetic energy.

3.5 Triggers and Additional Corrections

Due to a rapid increase of the inner magnetic field near the end of the flux compression process, an adaptive Lagrangian time stepping is used when the change in the magnetic field or the temperature of the liner surpasses the preset allowable limit. The time step is then repeated with the modified step size to recover the correct liner dynamics near the end of the implosion process. It was seen that without this correction, the liner is free to overshoot and become a negative radius, due to lack of a material contact model in the code. With the Lagrangian time step control, it was seen that the liner can be fully stopped by the increasing inner magnetic field, as expected.

As an experimental feature, the injection of a FRC into the liner is also modeled crudely as an instantaneous increase in the magnetic flux of the inner region. The additional magnetic flux injection is triggered at a preset FRC injection time. This feature is highly simplified model of the FRC compression, so the true physics of the liner based FRC compression process is not modeled. However, it allows for insight on the relationship of the liner stop radius and the final magnetic field to the increased inner magnetic field when FRC is injected.

3.6 Determination of Inductance and Flux-Field Geometric Parameter

As discussed earlier in this chapter, the inductance and the flux-field geometric parameters are obtained external to the 1D liner code. To obtain field and inductance data, commercial low frequency electromagnetic solver, ANSYS Maxwell 3D®, is used. The eddy current (AC) solver is used, where the magnetic field is solved under the assumption that all electromagnetic fields pulsate with the same frequency (specified by the user) and have a magnitude and an initial phase angle calculated by the solver. This solution process effectively solves the problem region as an AC steady state magnetic problem. While the nature of the liner compression process is transient, the AC solver can sufficiency capture the effect of the inductance shorting and the magnitude of the shorted field for the coil-liner system, given user defined characteristic frequency of the liner implosion process.

The characteristic frequency of the liner implosion process generally varies as a function of time and is generally driven by the exact physics of the liner implosion process. For example, during the acceleration phase, the characteristic frequency is generally governed by the rise time of the driver coil current due to the large coupling between the driver circuit and the liner. During the coasting and the deceleration phase, the coupling between the driver circuit and the liner is small, thus the characteristic frequency is governed more strongly by the actual dynamics of the liner. However, for typical liner implosion cases where the rise time is of order few tens of µsec with the liner speed of order few km/sec, effect of the frequency on the inductance and the flux-field geometric parameter is small. Thus, for the purpose of obtaining data from Maxwell 3D solver, the characteristic frequency is defined using the characteristic time scale of the driver circuit, and it typically ranges in the order of tens of kHz.

For cases where the design of the driver coil is known a priori, the exact geometry of the driver coil and the liner can be imported into Maxwell 3D solver to compute the inductance and the geometric parameter associated with the given design. An example model of the coil analyzed in Maxwell 3D solver that was based on the design of the actual coil used in the experiment is shown in Fig 3.7. The input current is fed into the driver coil through the feedplate, and the eddy current setting is used to automatically compute the resulting eddy current that develops in the liner. The inductance of the coil-liner system is calculated automatically by the Maxwell 3D solver. The geometric parameter for coil-liner system is computed using the equation

$$C_A(r_{liner}) = \frac{\frac{1}{S_{lo}}\int_{S_{lo}} |B|\, dS}{\int_{S_{out}} \mathbf{B}\cdot d\mathbf{S}} = \frac{\langle B\rangle|_{S_{lo}}}{\Phi_{out}} \tag{3.46}$$

where S_{lo} is outer liner surface, S_{out} is cross-section of the outer region, and $\langle B\rangle|_{S_{lo}}$ is the surface averaged magnetic field on the liner outer surface.

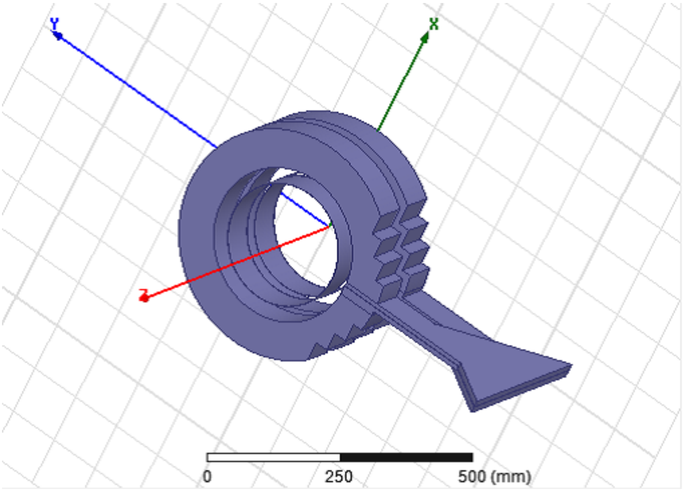

Figure 3.7: Example 2-turn series coil-liner system model used in ANSYS Maxwell 3D® eddy current solver.

A parametric solver setting is used in Maxwell 3D solver to sweep through various liner radius, thickness, and initial liner position, assuming constant liner axial length and constant liner volume. The result for the coil-liner system inductance and the flux-field parameter is tabulated so it can be imported into the 1D liner code.

A similar process is repeated for the model with the liner alone to compute the self inductance and the flux-field parameter for the liner. The geometric parameter for the liner is computed using the equation

$$C_B(r_{liner}) = \frac{\frac{1}{S_{li}}\int_{S_{li}} |B|\, dS}{\int_{S_{in}} \mathbf{B}\cdot d\mathbf{S}} = \frac{\langle B\rangle|_{S_{li}}}{\Phi_{in}} \tag{3.47}$$

where S_{li} is inner liner surface, S_{in} is cross-section of the inner region, and $\langle B\rangle|_{S_{li}}$ is the surface averaged magnetic field on the liner inner surface. Example results for the inductance of the coil-liner system and the liner computed from Maxwell 3D solver is shown in Fig. 3.8. Such tabulated result for the inductance is imported into the 1D liner code.

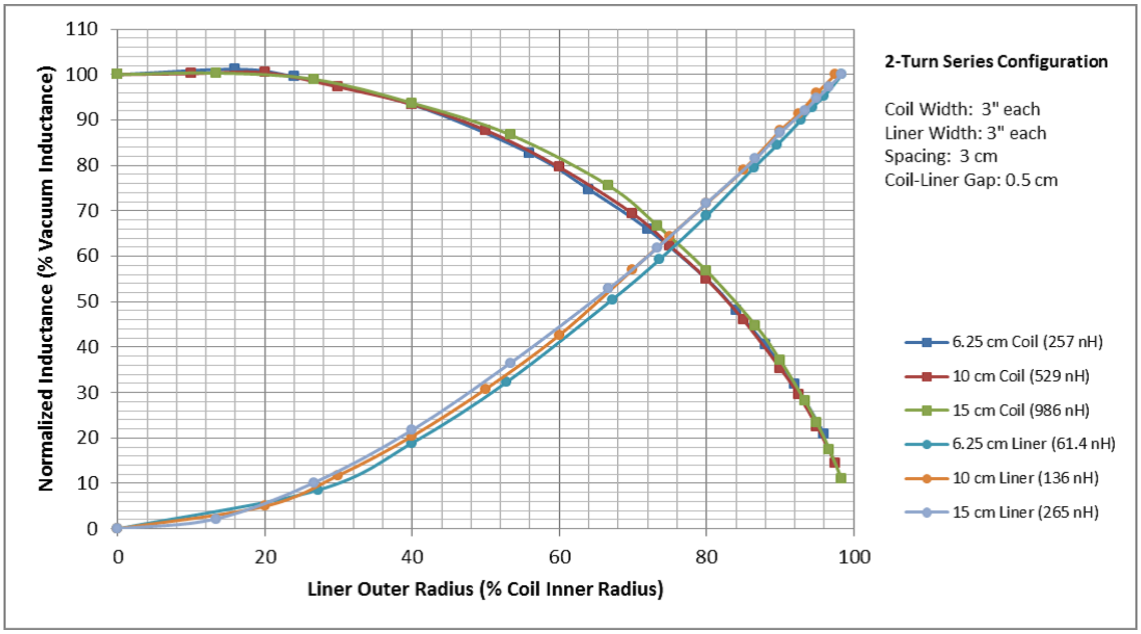

Figure 3.8: Example result of inductance calculated by ANSYS Maxwell 3D® eddy current solver as a function of the liner outer radius.

Chapter 4

VERIFICATION OF THE 1D LINER CODE

In this chapter, the 1D liner code is ran against commercial solvers to verify that each component of the code is capturing correct physics. The circuit solver is compared against a commercial SPICE circuit solver, Intusoft ICAP/4. The liner implosion dynamics is compared against the result from ANSYS® Explicit Dynamics solver predictions.

4.1 Verification of Circuit Calculation using Intusoft ICAP/4®

A commercial SPICE solver is used to verify the validity of the circuit calculation in the 1D liner code. An ideal crowbar circuit is used in both SPICE and the 1D Liner code, and the resulting currents and the capacitor bank voltage is monitored. The vacuum (no liner) case is used in the 1D liner code, such that only the circuit solver is advanced in time. The SPICE circuit diagram of the ideal crowbar circuit is shown in Fig. 4.1. The circuit solver in the 1D liner code is setup to use the same circuit configuration as SPICE.

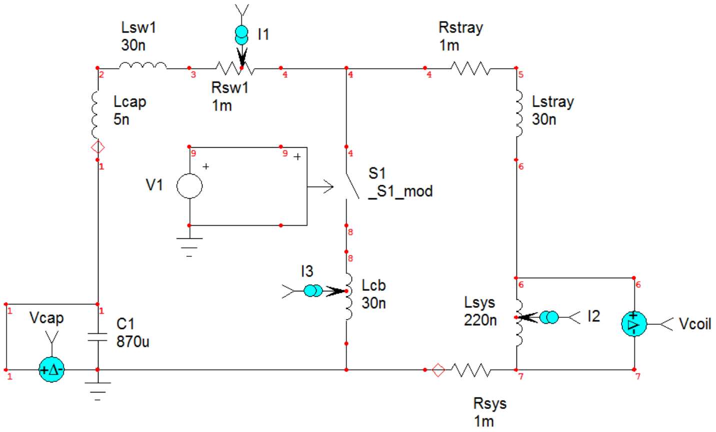

Figure 4.1: SPICE circuit diagram for ideal crowbar circuit for vacuum case

The resulting current flowing in the three sections and the capacitor bank voltage as function of time calculated from the SPICE and the 1D liner circuit solver is shown in Fig. 4.2. It can be seen from the figure that the 1D liner circuit solver agrees very well with the SPICE calculation, and the two results agree almost perfectly. While a slight deviation can be seen in the ringing section after the firing of the crowbar, this is caused by a small difference in the crowbar switch firing time for the two solver. This error is caused by a small difference in how the switch firing is modeled in the two solver, so slight deviation should not be a concern. The result from the SPICE solver verifies that the 1D liner circuit solver correctly solves the ideal crowbar circuit in the vacuum condition.

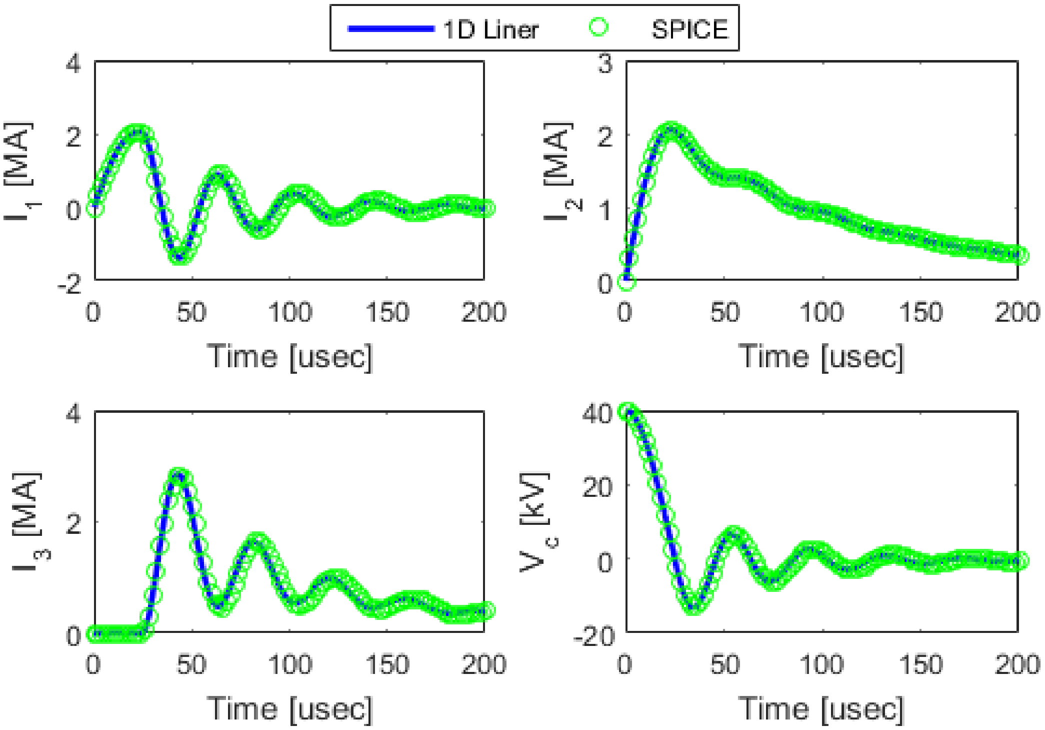

Figure 4.2: Comparison of the calculated current for vacuum case

To test if the circuit model is solved correctly for the case of a dynamic inductance and resistance associated with the coil-liner system, an analysis with a dynamic liner is carried out in the 1D liner code. The resulting dynamic inductance and resistance profile is then exported to the SPICE solver to model case with a dynamic inductance and resistance in the SPICE solver. The profile of the dynamic resistance and inductance calculated by the 1D liner code and the fitted dynamic data imported into the SPICE solver is shown in Fig. 4.3.

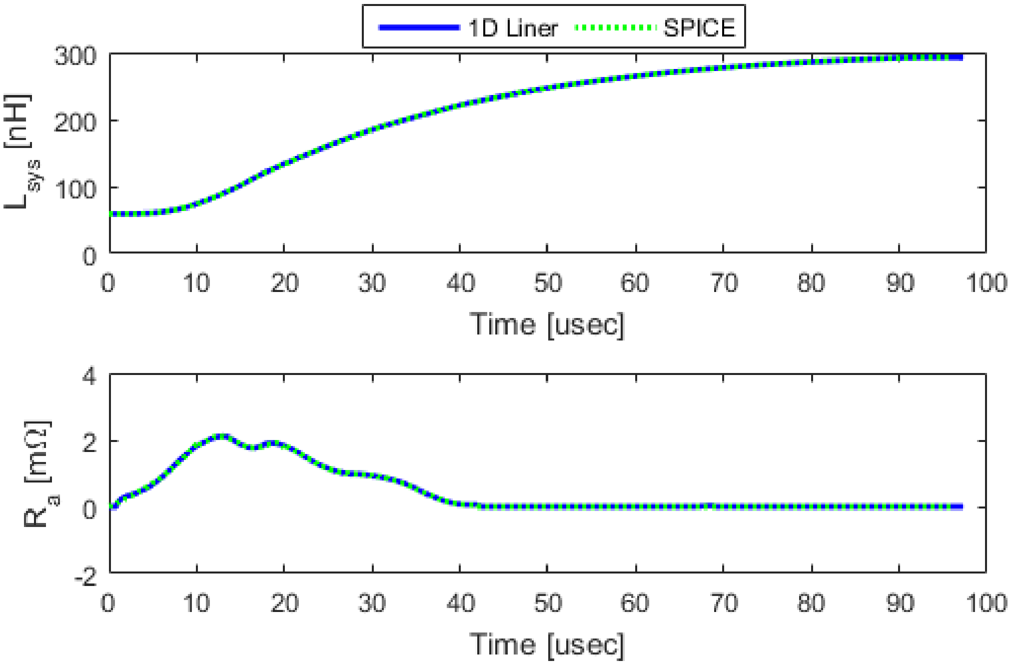

Figure 4.3: Profile of coil-liner system dynamic inductance and resistance

The resulting current flowing in the three sections and the capacitor bank voltage as function of time calculated from the SPICE and the 1D liner circuit solver is shown in Fig. 4.4. It can be seen from the figure that the 1D liner circuit solver agrees well with the SPICE calculation, even for the case of a dynamic coil-liner system impedance. Since there is a finite error in the fitting on the dynamic coil-liner system impedance and since the SPICE model is ran in a piecewise fashion in ICAP/4 to mitigate solver limitations, the two result does not agree perfectly. However, even with these limitations, the solution profile agrees very well with each other. The SPICE results predicts a slower crowbar decay due to a larger peak current flowing through the crowbar switch, but the difference is small. This is most likely caused by slight deviation in the resistivity of the coil-liner system between the two solver, due to imperfect fitting. Since the error due to these effects are small, the result from the SPICE solver verifies that the 1D liner circuit solver is correctly capturing the effects of a dynamic resistance and inductance of the coil-liner system.

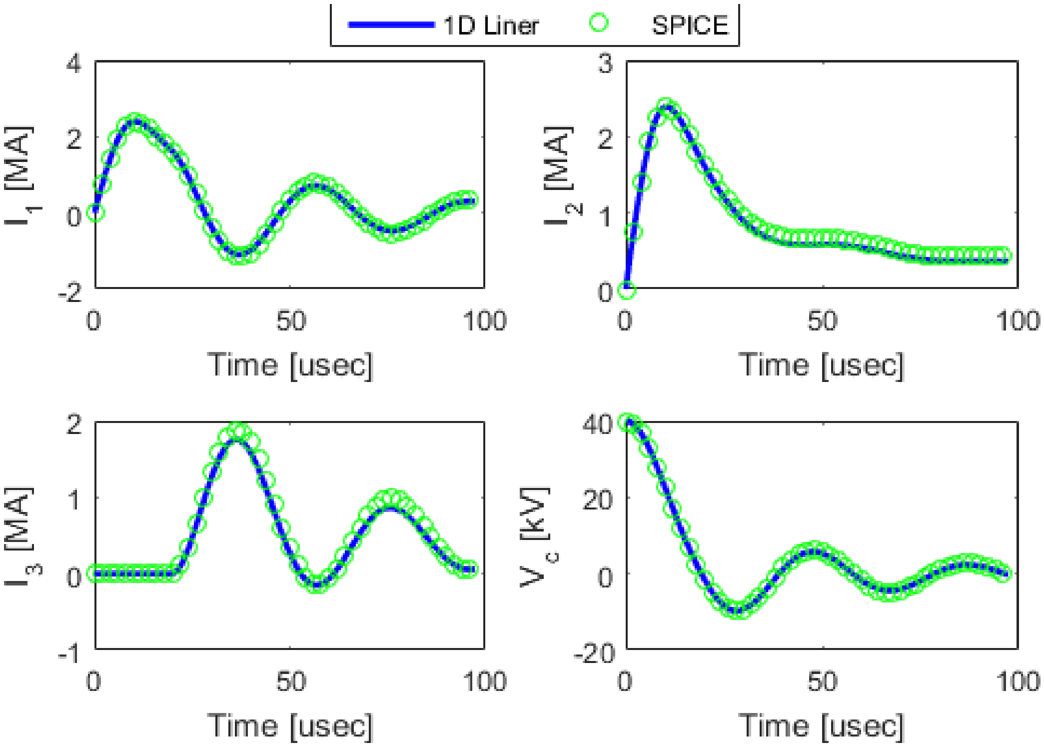

Figure 4.4: Comparison of the calculated current and voltage for the dynamic impedance case

4.2 1D Dynamics Verification using ANSYS Explicit Dynamics®

ANSYS Explicit Dynamics® solver is used to compute the dynamic evolution of the liner, using the time dependent magnetic pressure data obtained from the 1D liner code. In the past, the result from ANSYS Explicit Dynamics® solver were shown to agree well with the experimentally measured behavior of the liner [17, 18], thus it should give a reasonable measure of accuracy of the liner dynamics calculated by the 1D liner code.

For this test, outer radius of 14.5 cm, thickness of 30 mil, and axial length of 10 cm is assumed for the liner geometry. The liner is assumed to be made of Aluminum 1100-O, which uses Steinberg Guinan strength model [19]. The liner self-contact is assumed to be frictionless in the analysis. The mesh with 91200 Hex8 element (with element midside node dropped) is used in the explicit dynamics solver. The pressure is assumed to be axially uniform on the liner surface. The resulting dynamics of the liner calculated by the explicit dynamics solver is shown in Fig. 4.5 in 30 µsec interval.

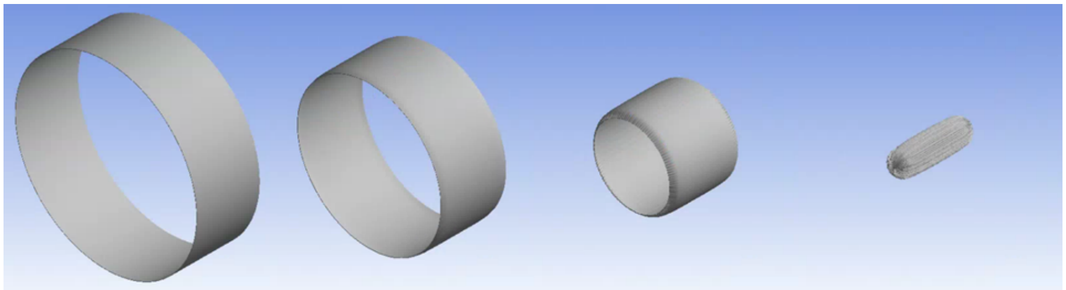

Figure 4.5: Time evolution of liner in 30 µsec interval calculated using ANSYS Explicit Dynamics® solver

The resulting kinetic energy of the liner and the time dependent liner radius is shown in Fig. 4.6. It can be seen that the liner dynamics predicted by the 1D liner code agrees in general with the more accurate result calculated by the explicit dynamics code, which accounts for true material property and internal mechanical energy losses. The time evolution of the liner radius computed from the explicit dynamics solver matches very well with that computed from the 1D liner code. The divergence in the data for the minimum radius computed from the Explicit Dynamics solver is caused by the barrel distortion of the liner ends, where the ends collapse faster than the center of the liner. However, for majority of the liner, the result from two solvers agreed very well with each other.

As it can be seen from Fig 4.6, the biggest divergence in the kinetic energy results occurs during the final deceleration phase of the implosion process. This is caused by the increasing loss from the plastic hardening of the liner, as the liner is forced to a smaller circumference.

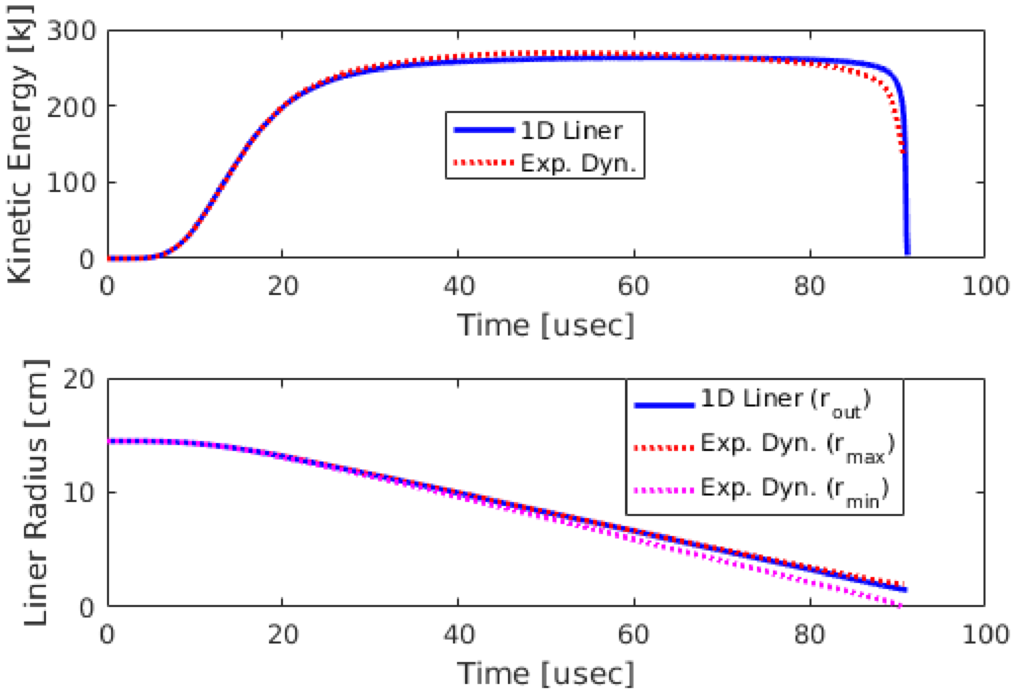

Figure 4.6: Comparison of liner radius and kinetic energy as function of time calculated by the 1D liner code and ANSYS Explicit Dynamics® solver

This effect causes the liner to begin decelerating faster than the more sudden deceleration process predicted by the 1D liner code. The loss of the liner energy to the internal energy can be seen in Fig. 4.7, where the ratio of the liner kinetic energy to the liner total energy is plotted as a function of time. As it can be seen, near the end of the compression process, the internal energy loss begins to dominate the total energy.

However, this is does not invalidate the usefulness of the 1D liner code, as the code is designed only to capture the initial acceleration phase of the implosion process. As it can be seen from Fig 4.6, the 1D liner code correctly capture the maximum kinetic energy that the liner can attain from the driver circuit. The initial acceleration phase of the implosion also is captured very well by the 1D liner code. Thus, the result from the explicit dynamics code verifies that the simplifying assumption made in 1D liner code where material mechanical properties are neglected is approximately correct, because the internal mechanical losses are small in the acceleration phase. At the location of the maximum kinetic energy, the energy loss to the internal energy is found to be about 3% of the total energy, which is only small deviation from the idealized result.

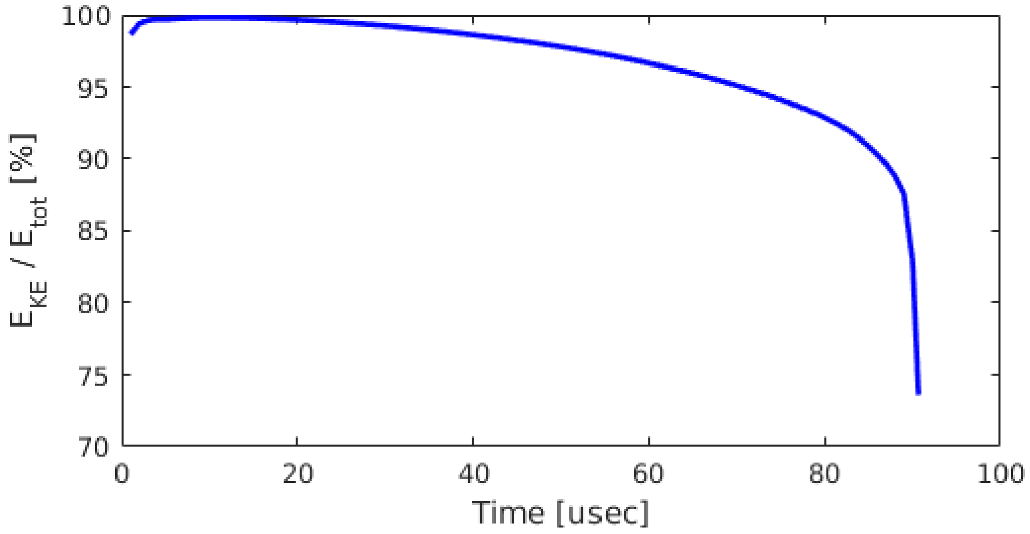

Figure 4.7: The ratio of liner kinetic energy and total energy computed by ANSYS Explicit Dynamics® solver

Chapter 5

PARAMETRIC OPTIMIZATION OF INDUCTIVE COMPRESSION DRIVER SYSTEM

5.1 Introduction

Using the 1D liner code discussed in Chapter 3, a parametric analysis is conducted to optimize the inductive compression driver system to maximize performance of the inductively driven liner compression (IDLC) system for the application to the Fusion Driven Rocket (FDR), while keeping parameters realistic. To obtain the optimized value for a realistic design, a parametric sweep is taken about some default configuration that is based on the proposed FDR design.

For the default configuration for the proposed FDR design, the design of the FDR discussed in the Fusion Driven Rocket phase 1 and phase 2 final report is used (in ref [16,18]). For required values that are not discussed in the two references, a realistic value based on previous IDLC experiments are used. Using designs of the FDR discussed in the two reports not only ensures realistic values for the optimized design, but also ensures that the optimized design are compatible with all of the previous mission analysis work that has been conducted for the potential application of the FDR for a round trip Mars mission. By maintaining the optimized design to be within the design envelop developed in the two reports, all of the previous mission design, orbital trajectory analysis, detailed spacecraft mass breakdown, and spacecraft power balance is applicable to the optimized design of the IDLC driver system.

5.2 Analysis Setup

Based on results from ref [18] and ref [16], the capacitor bank energy of 1.8 MJ is assumed to ensure that it is compatible with the estimated power requirement and the estimated total mass of the spacecraft for the capacitor banks and the required solar panels. The driver coil inner radius of 1 m is assumed to ensure that it is compatible with the proposed dimension of the FDR thruster system. Lithium liners are assumed as discussed in ref [18] and [16].

To define the default values for quantities that are not explicitly fixed in ref [18] and ref [16], an estimated value based on previous studies or a good engineering judgment is used. The liner initial radius is assumed to be 99 cm, since typically, some clearance is required to maintain a vacuum wall and an insulation between the driver coil and the liner. An assumed gap spacing of 5 mm has been used in the past [18], but for conservative estimate, 1 cm gap is reasonable. A greater gap size is possible, but since the driver performance diminishes as gap size is increased, no further safety margins are taken. The Liner axial length of 15 cm is also assumed based on the previous IDLC design from ref [18]. Default liner thickness of 30 mil is also assumed, but the liner thickness is taken to be a parameterizable variable that is swept in the parametric analysis. A default temperature of 300 K is used for the liner, and no bias field is applied in default configuration.

For the driver circuit, a stray inductance of 20 nH and a stray resistance of 1 mΩ associated with co-ax wires and switches are assumed per section in the crowbar circuit (shown in Fig. 3.3). The assumed values for the stray are estimated based on past IDLC design works. The capacitor bank is assumed to have stray inductance of 5 nH and negligible stray resistance, which is not too far from realistic values. In reality, the stray value associated with wires, switches, and capacitors can be changed relatively easily by using massively parallel circuit designs. In the parametric analysis, a multiplicative factor (stray multiplier) is applied to the stray values to determine whether additional efforts required to parallelize the driver circuit is necessary for the optimized operation of the IDLC driver coil.

The inductance of the coil-liner system is obtained using ANSYS Maxwell 3D® Eddy Current solver using a simplified driver coil geometry for various liner radius and thickness. The driver coil resistance is estimated to be 0.5 mΩ using the Maxwell 3D solver. The default bank voltage is assumed to be 40 kV, and consequently, the bank capacitance is determined to be 2.25 mF from the capacitor bank energy assumption of 1.8 MJ (using relationship

$E_{cap} = \frac{1}{2}CV^2$, where E_{cap} is the capacitor bank energy, C is the bank capacitance, and V is the bank voltage).

The default parameters used in this analysis are summarized in Table 5.1. The inductance and the flux-field parameter associated with the coil-liner system and the liner itself is determined using ANSYS Maxwell 3D® eddy current solver, and a parametric sweep is run within Maxwell 3D solver such that values at different liner radius is obtained. To make the inductance and the flux-field parameter values consistent with the 1D liner solver assumptions, at different liner outer radius, a volume conservation assumption is used to vary the thickness to preserve the volume of the initial liner configuration. Solver frequency of 15 kHz was used. The resulting value of the inductance and the flux-field parameter after fitting it with a piecewise cubic Hermite interpolating polynomial (PCHIP) in Matlab® is shown in Fig. 5.1. It can see from the figure that the thickness does not affect the inductance or the flux-field parameter significantly, since the skin depth is small for the solved condition and since the thickness of the liner appears to the driver coil as if it is a skin depth thick.

Coil-Liner Geometry	
Parameter	**Default Value**
Driver Coil Radius	100 cm
Initial Liner Radius	99 cm
Liner Axial Length	15 cm
Liner Thickness	30 mil
Liner Material	Lithium
Liner Temperature	300 K
Initial Bias	0 Wb

Circuit Configuration	
Parameter	**Default Value**
Bank Energy	1.8 MJ
Bank Voltage	40 kV
Bank Capacitance	2.25 mF
Bank Inductance	5 nH
Stray Inductance	20 nH
Stray Resistance	1 mΩ
Coil Resistance	0.5 mΩ

Table 5.1: Initial values used in the parametric analysis for the default configuration.

For the optimization, it is assumed that the bank voltage, the liner thickness, the initial bias flux, and the stray multiplier can be adjusted. The bank voltage is swept from 15 kV to 60 kV, which represents a realistic range of capacitor bank voltage to run an IDLC system without requiring a special treatment to prevent a capacitor bank voltage breakdown. The liner thickness is swept from 20 mil to 50 mil, which corresponds to a range of thickness

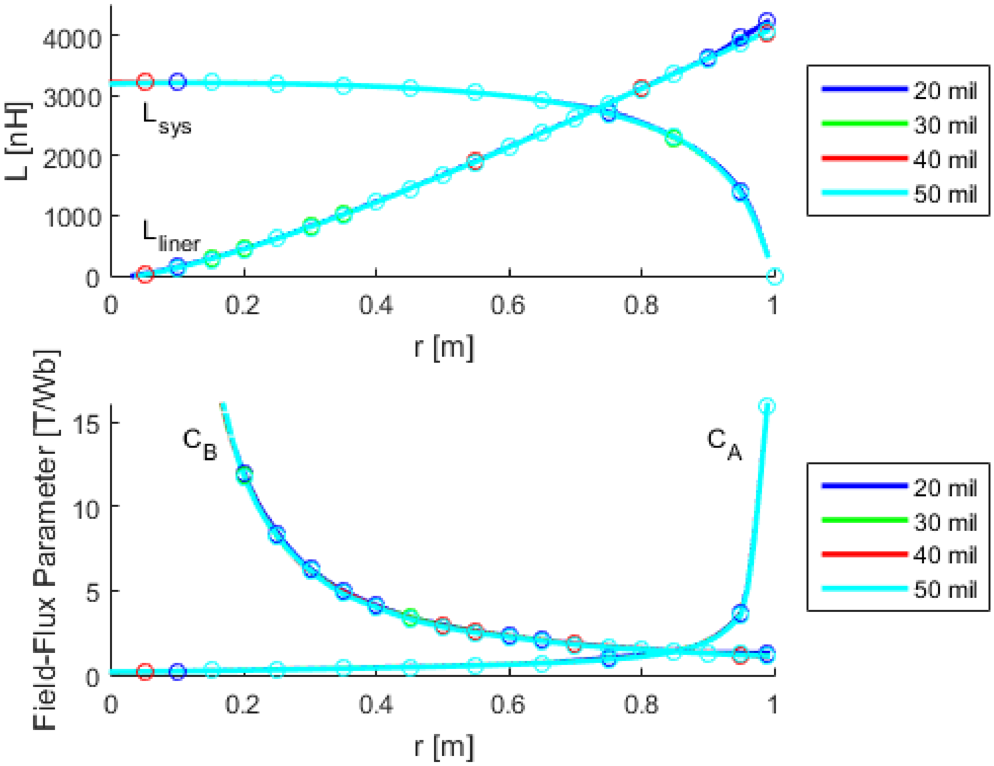

Figure 5.1: (Top) Coil-liner system inductance (L_{sys}) and liner inductance (L_{liner}) calculated by Maxwell 3D eddy current solver for various liner thickness. (bottom) Coil-liner system flux-field parameter (C_A) and liner flux-field parameter (C_B) calculated by Maxwell 3D eddy current solver for various liner thickness.

required for the liner to be close to the optimum range of propellant mass required to achieve the most efficient specific impulse for Mars mission using the FDR thruster (values based on the calculated result in ref [18]). The initial bias flux is swept from -0.5 Wb to 0.5 Wb, which corresponds to a practical limit for injecting seed magnetic flux using externally driven coils. The stray multiplier is swept from 12.5% to 150% which gives good range to test the significant of stray losses for an efficient driver coil energy transfer. The summary of the parametrized variables are given in Table 5.2.

To determine the optimum design point, following design criteria are used: (1) The

Parameter	**Min Sweep**	**Max Sweep**
Bank Voltage	15 kV	60 kV
Liner Thickness	20 mil	50 mil
Initial Bias	-0.5 Wb	0.5 Wb
Stray Multiplier	12.5 %	150 %

Table 5.2: Summary of the parametrized variables.

maximum liner speed must exceed the threshold velocity required to ensure that the liner dwell time exceeds the FRC energy confinement time. To ensure this, minimum peak liner velocity of 2 km/sec is required according the rule of thumb estimate given in ref [18]. (2) The optimized design must maximize energy transfer from the driver circuit to the liner kinetic energy. In particular, the efficiency of the energy transfer from the capacitive energy to kinetic energy must be maximized to ensure good energy coupling. (3) The estimated fusion gain from the liner compression process (computed using eq. 1.2) must be maximized. (4) A premature liner melting during the coasting phase should be avoided if possible. (5) The liner must be able to compress down to a reasonable radius and approach a mega-gauss final magnetic field value at the peak compression.

The first design criterion is straight forward to implement, and it just means that all of the design points which does not allow the liner to reach a peak velocity of 2 km/sec is thrown out. The second and third design criteria are also quantitative, and it is implemented by finding design points that maximizes the energy coupling and the fusion gain. The fourth design criterion is qualitative, but it just means that the design that does not cause the liner to melt during the coasting phase is preferred for liner stability reasons. If the liner melting can be delayed until the final deceleration phase of the implosion process, then that design is preferred. The fifth design criterion is also qualitative, but it is in place to ensure that the liner has enough inertia from the energy transfer such that it can compress the FRC to a point of ignition. Since the present code does not capture the correct physics of the liner-FRC interaction and the liner turnaround phenomena, only qualitative requirement is placed for analyzing fifth design criterion.

For the optimization, first, a sweep in the bank voltage, liner thickness, initial bias, and stray multiplier are made about the default configuration such that the each parametric variables are swept independently of each other. Using the data generated, general performance trends are evaluated. Once the performance trends are determined and the approximate design space to optimize the design is determined, a further parametric runs are conducted inside the identified design space to fully optimize the design.

5.3 *Summary of Results for Parameter Independent Sweep*

5.3.1 Results from Bank Voltage Variation

The results for the case when the bank voltage is varied are shown in Fig 5.2. It can be seen from the figure that the peak liner velocity, energy coupling efficiency, and gain all increases when the bank voltage is increased. The performance increase seems to be slowly saturating, as slope of the performance increases decreases as the bank voltage is increased, but for the range of voltage tested, the performance increase with a higher voltage is still significant such that highest possible voltage is preferred.

The reason for the performance increase when the voltage is increased is due to the reduced LC time constant for the driver circuit, which allows the driver circuit to reach its peak value quicker. Because capacitor bank energy is fixed in this analysis, increase in a bank voltage corresponds to a decrease in the bank capacitance. From the equation for the energy stored in a capacitor, it is well known that for fixed energy bank, when a voltage is doubled, the capacitance is quartered. Thus, LC time constant decreases rapidly as the bank voltage is increased.

Decrease in LC time constant is helpful in improving the performance of the liner compression, since it allows the driver circuit to reach peak current before the liner moves radially inward, and “slips” away from the driver coil. Since the magnetic field in the shorted region is function of both driver coil current and the cross-section of the shorted region, reaching

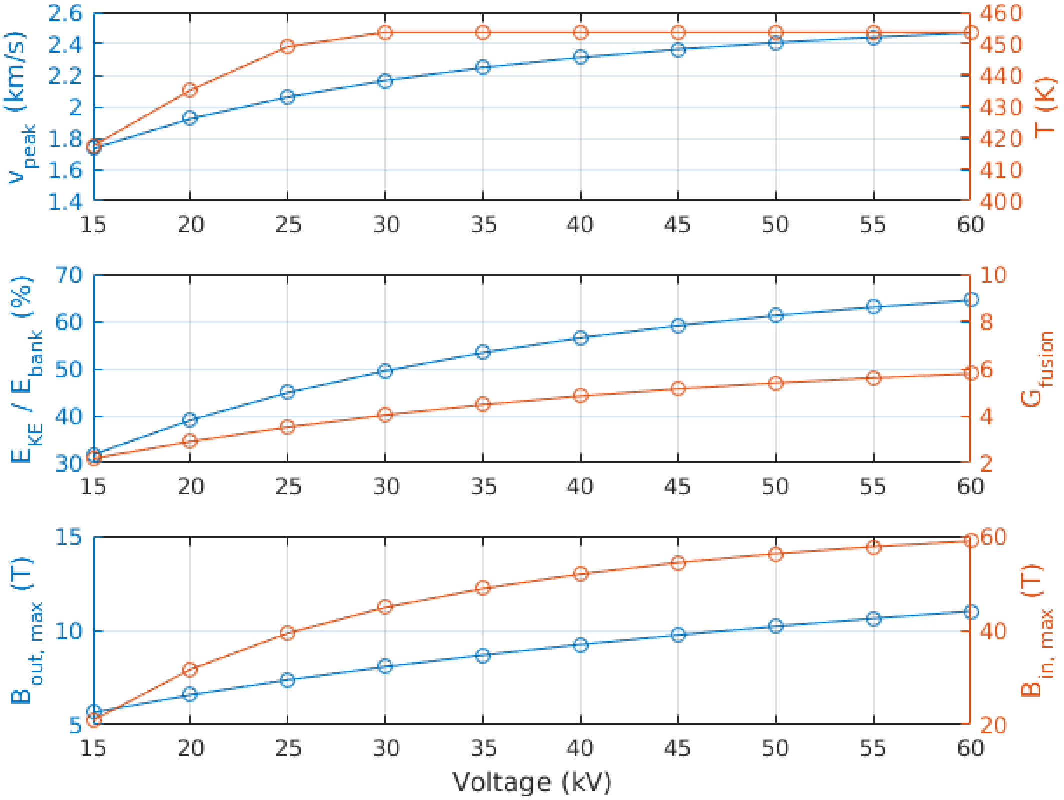

Figure 5.2: Liner performance with bank voltage variation for the default configuration. (Top) Results for peak liner velocity and peak temperature. (Middle) Results for energy coupling and fusion gain. (Bottom) Peak magnetic field in outer and inner region.

peak current before the liner moves significantly and increases the cross section of the shorted region is a key in effective acceleration of the liner (due to the higher peak magnetic field that one can achieve in the shorted region). There is an eventual saturation to this performance improvement, because if the LC time constant is too short, the shorted magnetic field will decay before the liner has chance to begin moving, and will cause an impulse like loading to the liner. Since liner does not have time to move with the applied pressure, the work done by the magnetic pressure is small, and as a result, the performance decreases. For the assumed 1 m driver coil configuration, since the inductance of the shorted driver coil is large, performance increase is seen when LC time constant decreases, and the saturation effect is seen to be small for the voltages tested.

5.3.2 Results from Liner Thickness Variation

The results for the case when the liner thickness is varied are shown in Fig. 5.3. It can be seen in the figure that the peak liner velocity decreases as the thickness is increased. This makes sense since an increase in thickness corresponds directly to an increase in liner mass, which for a fixed kinetic energy, corresponds to a decrease in the liner velocity. However, it can be seen that both energy coupling and fusion gain increases when the liner mass is increased. Thus, while the peak velocity decreases as the liner mass is increased, the final kinetic energy it gains from the driver circuit is higher.

Again, the same phenomena as described in the previous section is the main cause for improved energy coupling. Since the thicker liner has more inertia to resist the change in motion, the liner is allowed to "slip" less during the initial acceleration phase of the compression. Again, since shorted cross-section does not increase if the liner does not move, higher liner inertia allows the shorted magnetic field to reach higher value to push on the liner. Eventually, similar saturation phenomena should be seen, but for the cases tested, it was not observed.

From the energy coupling and the fusion gain optimization perspective, a higher liner mass is preferred. However, it can be seen that for 50 mil, the peak velocity for the liner is below the allowable threshold or 2 km/sec, thus, this suggests that 50 mil liner is too heavy to ensure that the liner dwell time exceeds the FRC energy confinement time. Thus, a thickness of 40 mil is the maximum thickness that can be used for the liner while still satisfying the allowed limit.

5.3.3 Results from Initial Bias Variation

The results for the case when the initial magnetic seed bias flux is varied are shown in Fig. 5.4. It can be seen that there exists some optimal value for bias flux, and it tend to occur at a

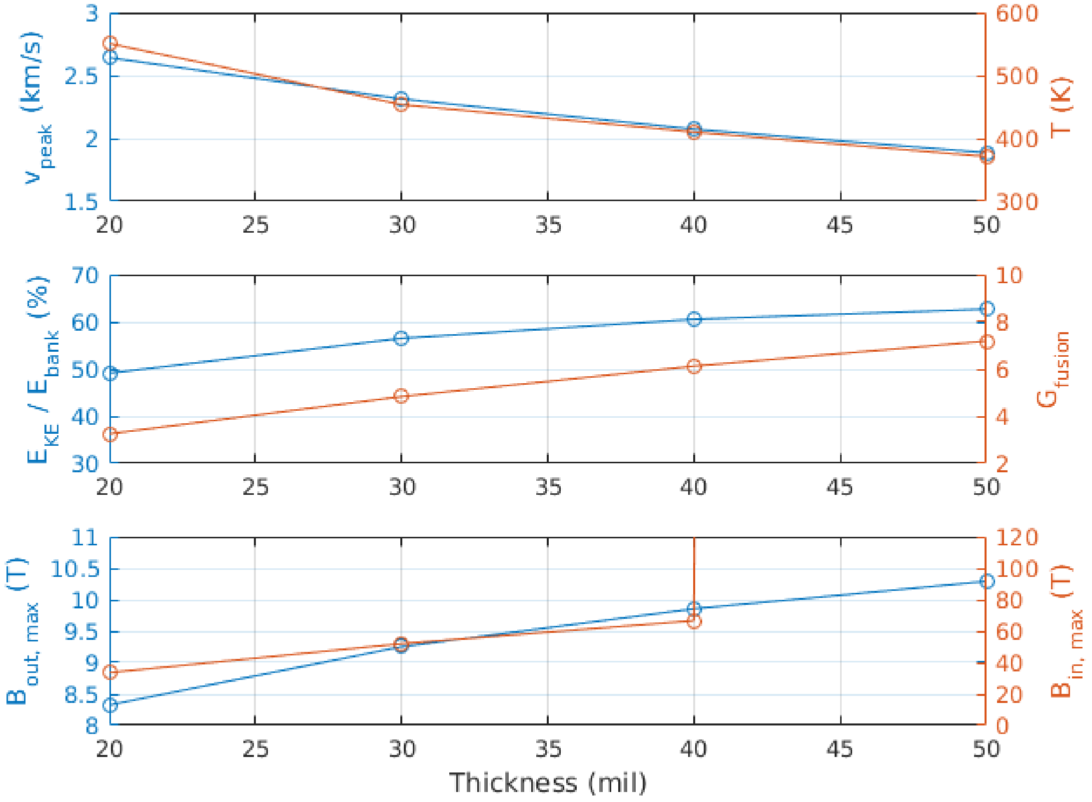

Figure 5.3: Liner performance with liner thickness variation for the default configuration. (Top) Results for peak liner velocity and peak temperature. (Middle) Results for energy coupling and fusion gain. (Bottom) Peak magnetic field in outer and inner region.

negative flux value. The initial bias most likely helps by applying radially outward magnetic pressure, which stops the liner from moving before the outer field grows high. Again, this is due to stoppage of the liner "slip" while the driver circuit is reaching its peak value. The eventual performance degradation from further increase in the bias field is due to the same effect discussed before.

The favoring of the negative bias to the positive bias in the liner compression performance is probably caused by the delaying of the push back effect by the inner region magnetic field. Since the magnitude of the magnetic pressure due to the inner region decreases until the

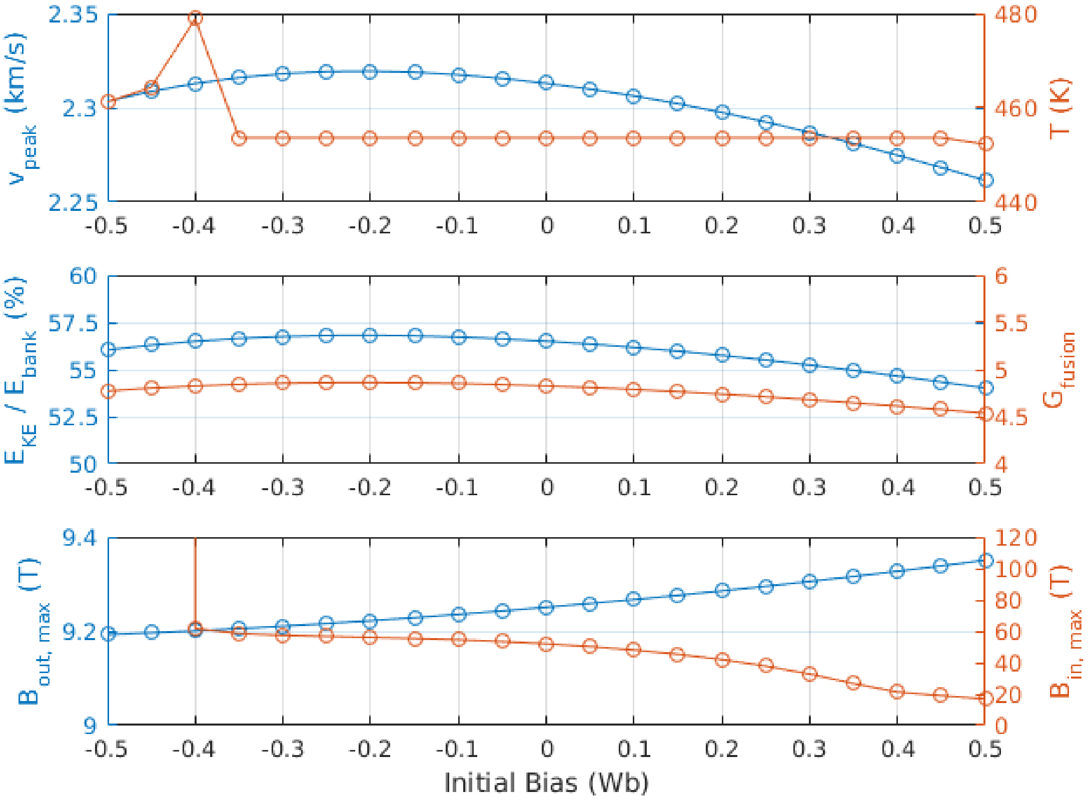

Figure 5.4: Liner performance with initial seed bias flux variation for the default configuration. (Top) Results for peak liner velocity and peak temperature. (Middle) Results for energy coupling and fusion gain. (Bottom) Peak magnetic field in outer and inner region.

field reversal in the inner region occurs, the inner region does not begin to slowing down the liner until later in the liner compression process. The result from the initial bias variation suggests that a negative initial bias should be used for the driver system. However, since performance change due to variation in bias is not very large, neglecting initial bias does not cause too much hit to the performance.

5.3.4 Results from Stray Multiplier Variation

The results for the case when the stray multiplier is varied are shown in Fig. 5.5. It can be seen that there is a linear dependence between the performance and the stray multiplier. Thus, for performance improvement, smallest possible stray multiplier should be used. Because LC time constant is already long for this configuration, any reduction in stray inductance helps in improving performance.

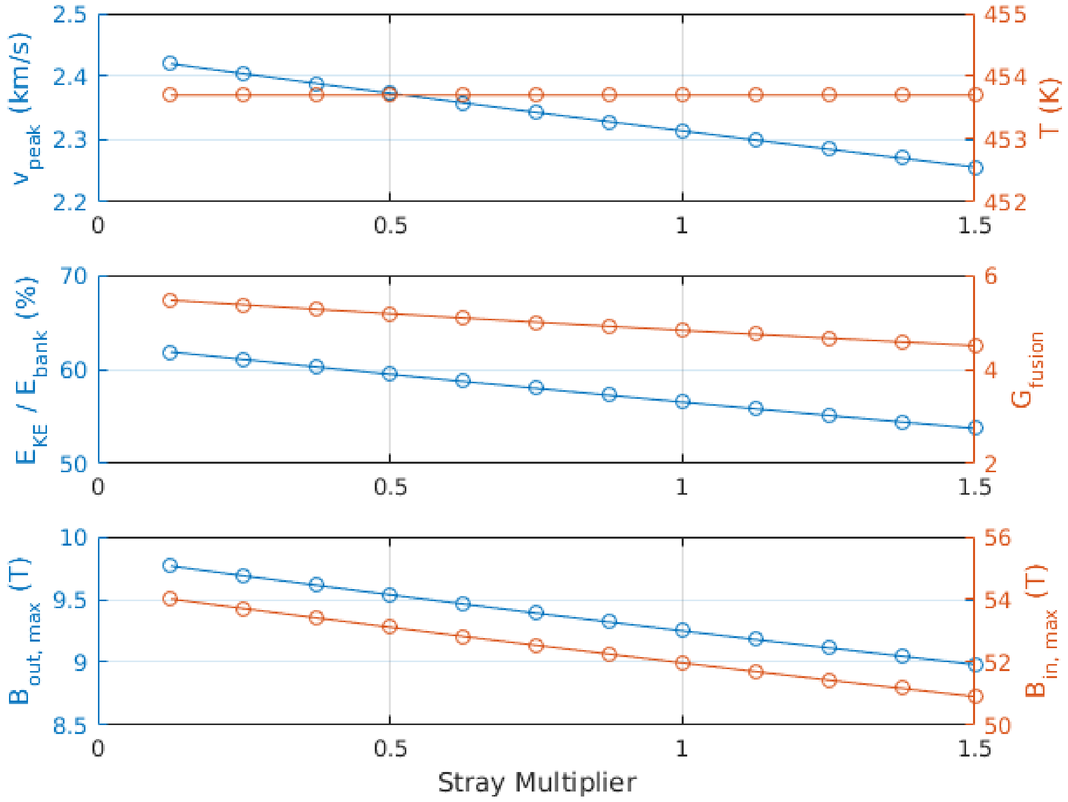

Figure 5.5: Liner performance with stray multiplier variation for the default configuration. (Top) Results for peak liner velocity and peak temperature. (Middle) Results for energy coupling and fusion gain. (Bottom) Peak magnetic field in outer and inner region.

5.4 Optimum Design Space from Parameter Independent Sweep

From the parameter independent sweep analysis, it is seen that the design optimize for higher bank voltage, higher liner thickness, negative initial bias, and smaller stray multiplier. From the driver circuit design considerations, it will most likely be hard to reduce stray multiplier below 0.375, since there is growing complexity associated with more parallelism one adds to the driver circuit.

For the liner thickness, it is seen that for thickness of 50 mil, the liner is too heavy, and it does not satisfy the threshold velocity required to ensure a liner dwell time that exceeds the FRC energy confinement time. Thus, 40 mil seems like a good limit. The liner thickness of 40 mil corresponds to a liner mass of 0.51 kg, which according to rocket propulsive performance calculation done in ref [18], corresponds to a specific impulse of approximately 5000 sec. A specific impulse of 5000 sec was seen to be optimal value in ref [18] for round trip mission to Mars according to detailed trajectory analysis, so a thickness of 40 mil is good choice in the final design.

Thus, to determine the final optimized design, the stray multiplier is fixed to 0.375, and the liner thickness is fixed to 40 mil. Since the voltage and the initial bias may depend on change to the stray multiplier and the liner thickness from the default value, it is swept again to determine the optimal design point. Since it was found previously that the design point optimizes for a higher voltage and a negative bias, design condition in the design space is defined by the bank voltage of 45 kV to 60 kV and the initial bias of -0.5 Wb to 0 Wb.

5.5 Summary of Results for the Optimized Design Point

The results obtained from sweeping through the design space with a liner thickness of 40 mil and a stray multiplier of 0.375 are shown in Fig. 5.6. The voltage sweep is taken in 1 kV increment, and the bias sweep is taken in 0.05 Wb increment. From the figure, it can be seen that the general trend observed in the previous sections holds true in this parameter space. The peak velocity, energy coupling, and fusion gain all increases with higher voltage, and optimize at slightly negative bias. It can be seen that for the range of voltages tested, performance optimizes around bias values of -0.2 to -0.15 Wb. For higher voltage, lower initial bias magnitude seems to be preferred. The performance begins to decrease rapidly as bias magnitude is increased beyond the optimal value.

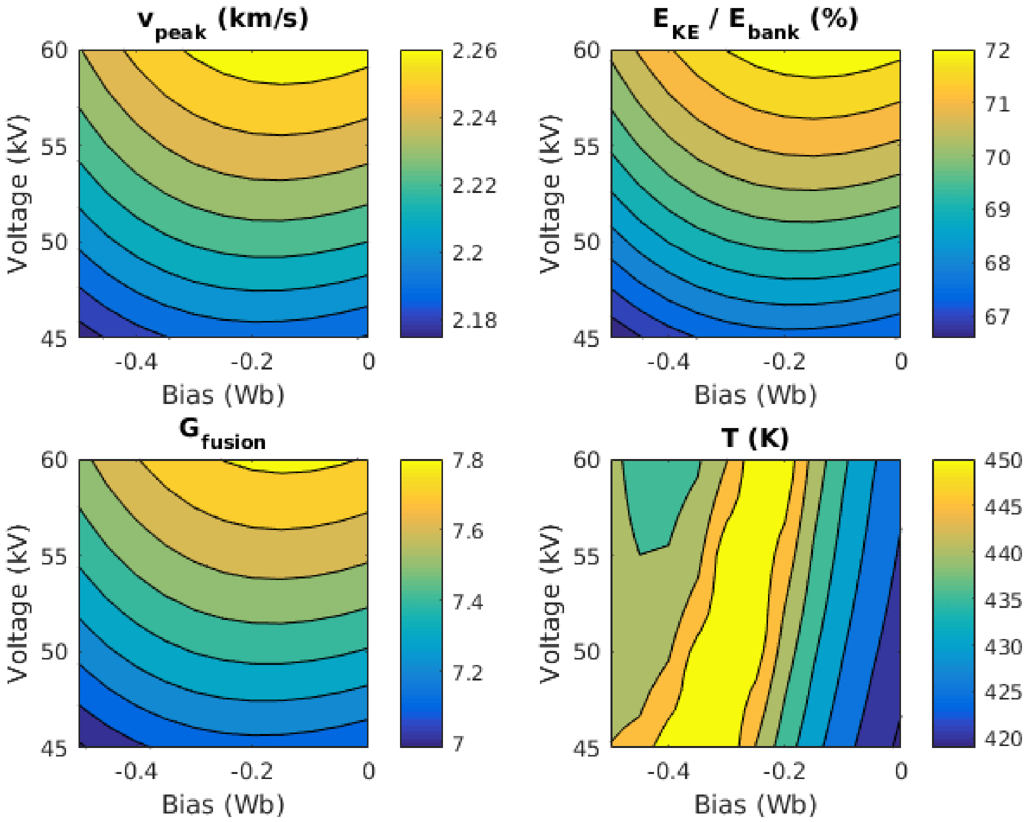

Figure 5.6: Liner performance as function of bank voltage and initial seed bias flux for the default configuration with liner thickness of 40 mil and stray multiplier of 0.375. (Top left) Results for peak liner velocity. (Top right) Results for energy coupling. (Bottom left) Results for the fusion gain. (Bottom right) Results for peak temperature.

From the result, it can be seen that for the analyzed design space, the peak liner velocity is approximately 2.2 km/sec with the energy coupling of 69%. The fusion gain is approximately around 7.4. The performance of the IDLC driver is satisfactory for almost any point in the design space, and to pick an optimum design point, engineering judgment must be made to weigh practicality of the design with its performance.

For one, it may not be desirable for the capacitor banks to operate at very high voltage, since it is more expensive and more difficult to work with. Generally, the capacitor that is used for pulsed operation in FDR must be able to withstand voltage reversal, and to ensure enough safety margin, the capacitor bank must be rated to handle twice the voltage that is required initially. This means more expensive capacitors are necessary, as they have to be rated for higher voltage conditions. Lower voltage is then desirable from the cost and the reliability viewpoint. The bank voltage of 50 kV is most likely a good engineering limit to place on the maximum operating voltage.

The performance of the IDLC driver with the capacitor bank voltage set to 50 kV, with the assumed liner thickness of 40 mil and the stray multiplier of 0.375 is shown in Fig. 5.7. It can be seen that performance change due to the initial bias is negligible at this condition. The estimated final magnetic field of the inner region is approximately 70 T for the initial bias lower than -0.3 Wb, so it is approaching mega-gauss field; for bias greater than -0.3 Wb, it shoots off to very large value.

Comparing the performance in Fig. 5.7, any negative bias flux can be chosen, since the performance change is negligible. However, since the choice of bias flux can effect the timing of the field strength reversal between the outer and the inner region, it has large consequence in the heating characteristic of the liner surface. Since the field reversal generally causes the inner surface of the liner to begin heating very rapidly due to the increase in the inner magnetic field due to flux compression process, delaying field reversal is useful in ensuring the liner to remain solid in the coasting phase of the liner implosion.

Fig. 5.8 shows the plot of the field reversal time and the collapse time for the various seed bias configuration. It can be seen that decreasing initial bias linearly increase the field reversal time, which corresponds to delay in heating of the liner due to increase in magnetic field of the inner region. The collapse time is generally the same for all initial bias, though there is small anomaly at bias of -0.3 Wb.

To prevent premature melting of the liner surface, it is desirable to delay the field reversal

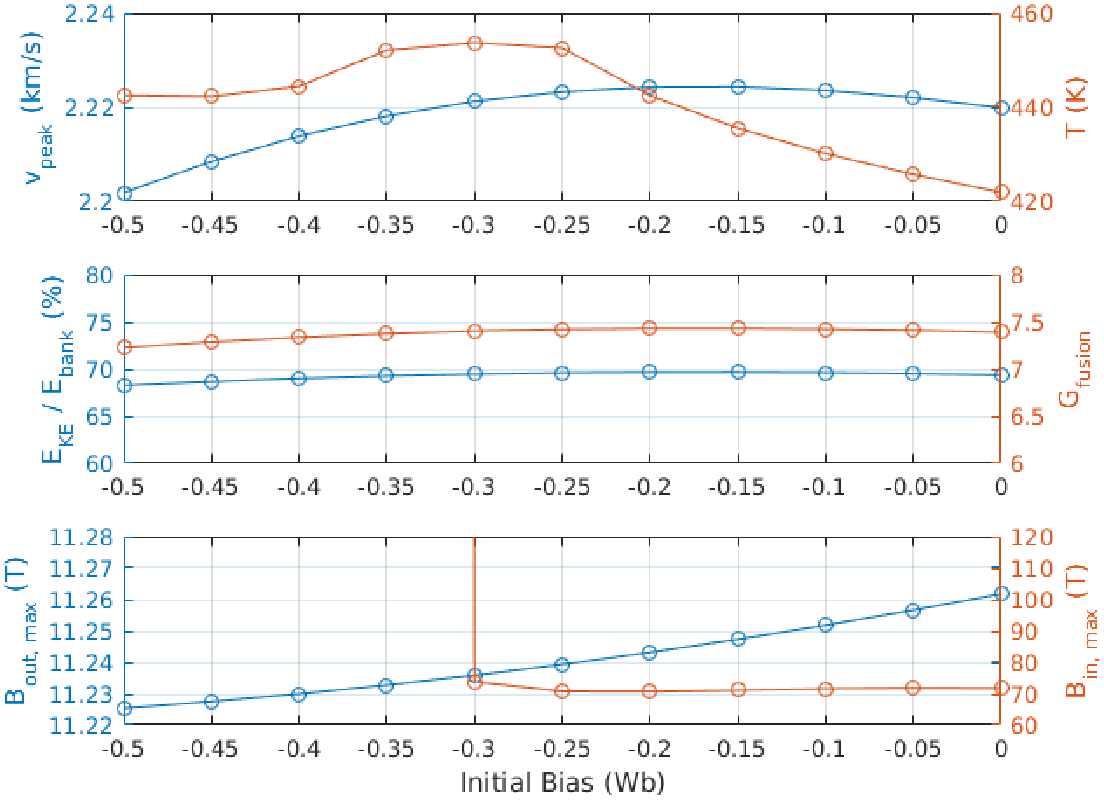

Figure 5.7: Liner performance with initial seed bias flux variation for the default configuration with bank energy of 50 kV, liner thickness of 40 mil, and stray multiplier of 0.375. (Top) Results for peak liner velocity and peak temperature. (Middle) Results for energy coupling and fusion gain. (Bottom) Peak magnetic field in outer and inner region.

such that heating in the inner surface does not begin until the liner dynamics is far in the flux compression phase. For this reason, lower bias flux is desired. However, from the optimization analysis, it was seen that liner performance optimize around -0.2 Wb. Thus, -0.2 Wb corresponds to the optimal condition for the liner compression performance.

The final optimized design point value for the IDLC driver is given in Ttable 5.3. The summary of the liner compression performance is given in Ttable 5.4. As it can be seen, through optimization, approximately 70% energy coupling was obtained. It can be seen

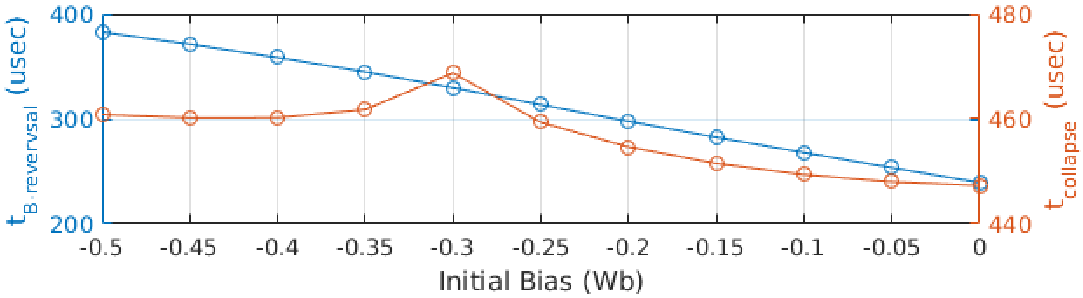

Figure 5.8: Field reversal time (left) and liner collapse time (right) for the 50 kV configuration for various initial bias flux.

that the final temperature of the liner is seen to be less than the melting temperature of the lithium liner (453.7 K), which suggests that until the very end of the liner implosion process (where the 1D Liner code is not valid), the liner remains solid, which is desirable from liner stability considerations (discussed in the next chapter). A reversal field of 0.425 T is obtained for this configuration, which suggests that the magnetic field in the inner region is low at the time of FRC injection, which is desirable such that no additional flux needs to be wasted to “push” the FRC inside the liner. The time dependent properties predicted by the 1D liner code for the optimized design is shown in Fig. 5.9 to Fig. 5.17.

Coil-Liner Geometry	
Parameter	**Optimized Value**
Driver Coil Radius	100 cm
Initial Liner Radius	99 cm
Liner Axial Length	15 cm
Liner Thickness	30 mil
Liner Material	Lithium
Liner Temperature	300 K
Initial Bias	-0.2 Wb

Circuit Configuration	
Parameter	**Optimized Value**
Bank Energy	1.8 MJ
Bank Voltage	50 kV
Bank Capacitance	1.44 mF
Bank Inductance	1.875 nH
Stray Inductance	7.5 nH
Stray Resistance	0.375 mΩ
Coil Resistance	0.5 mΩ

Table 5.3: Summary of the optimized design

Parameter	**Optimized Value**
Energy Coupling	69.7 %
Fusion Gain	7.43
Crowbar Time	73.2 µsec
Field Reversal Time	298 µsec
Collapse Time	455 µsec
Max B_{out}	11.2 T
Max B_{in}	70.7 T
$B_{reversal}$	0.425 T
Final Temperature	442 K

Table 5.4: Performance summary of the optimized design.

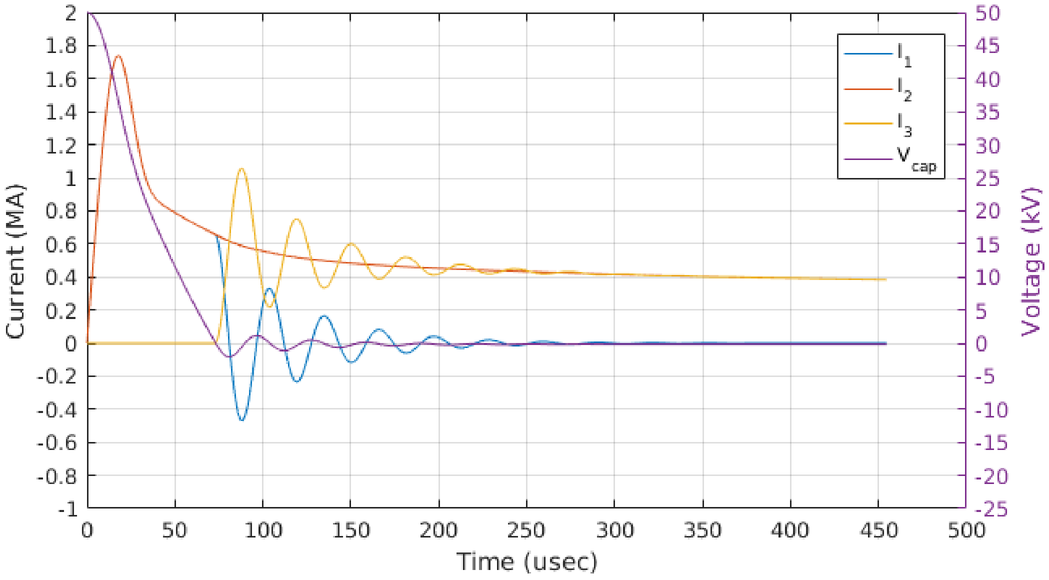

Figure 5.9: Time dependent circuit condition for the optimized design point

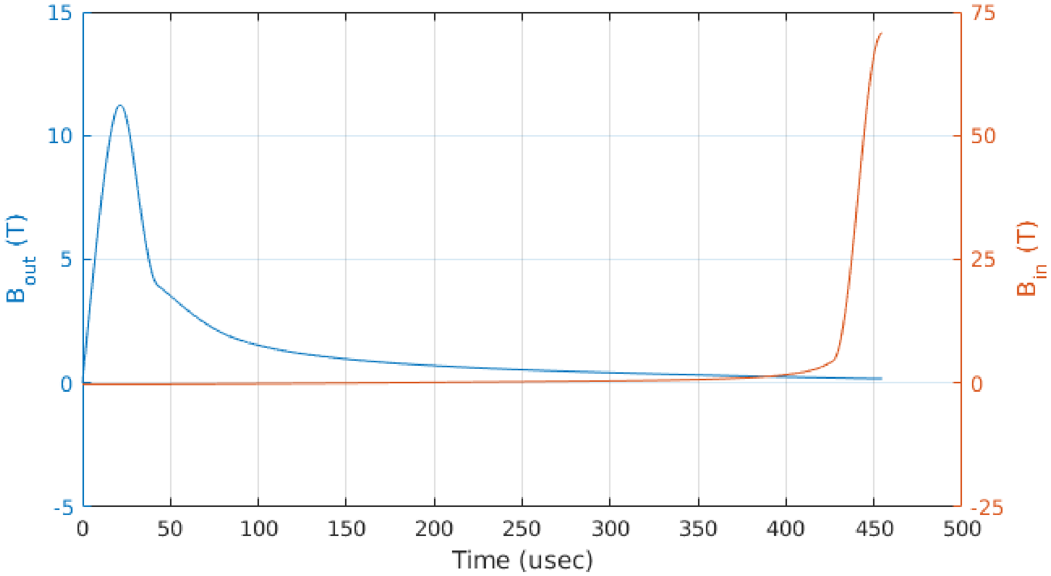

Figure 5.10: Time dependent magnetic field in outer (left) and inner (right) region for the optimized design point

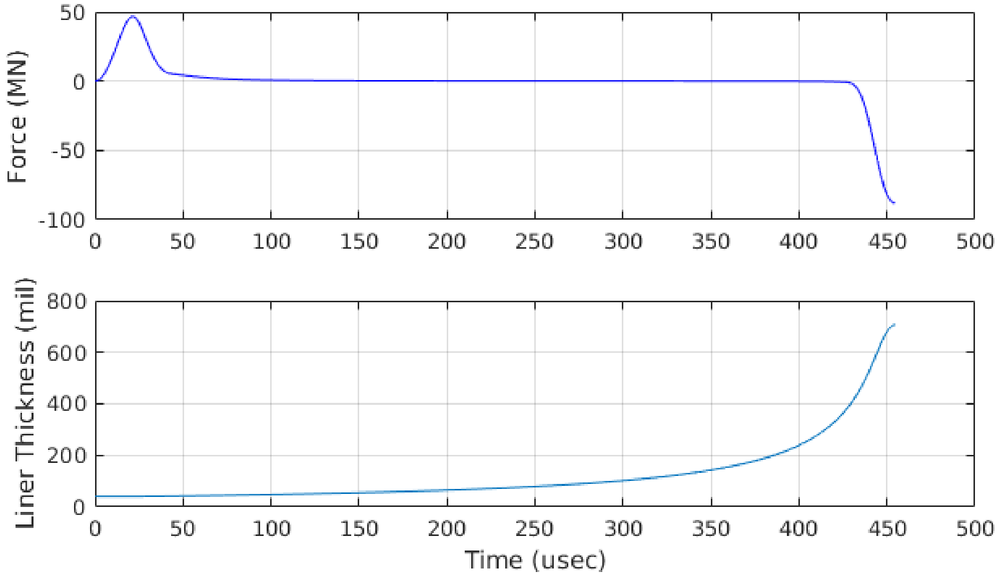

Figure 5.11: Time dependent magnetic force experienced by the liner (top) and time dependent liner thickness (bottom) for the optimized design point

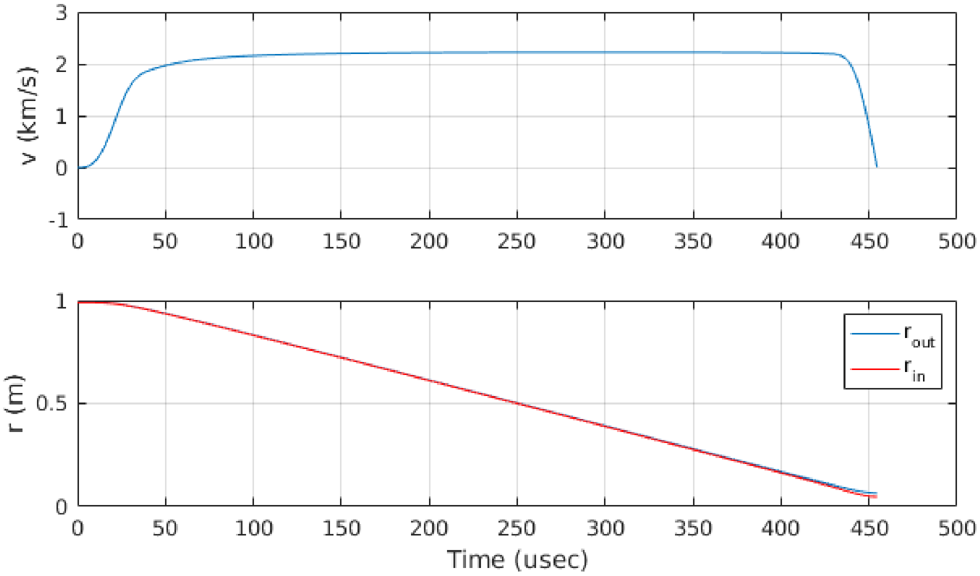

Figure 5.12: Time dependent liner velocity (top) and time dependent liner radius (bottom) for the optimized design point

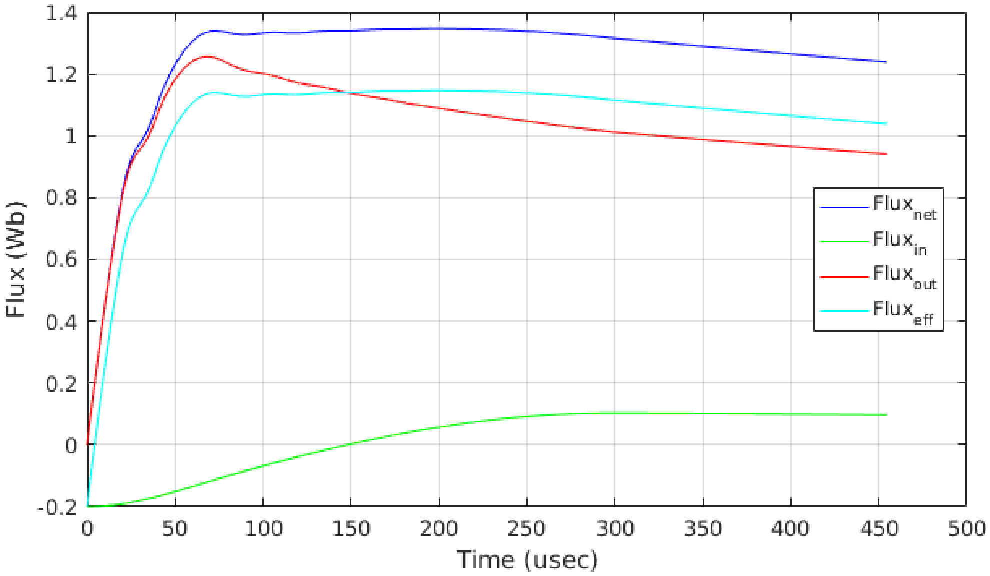

Figure 5.13: Time dependent magnetic flux evolution for the optimized design point

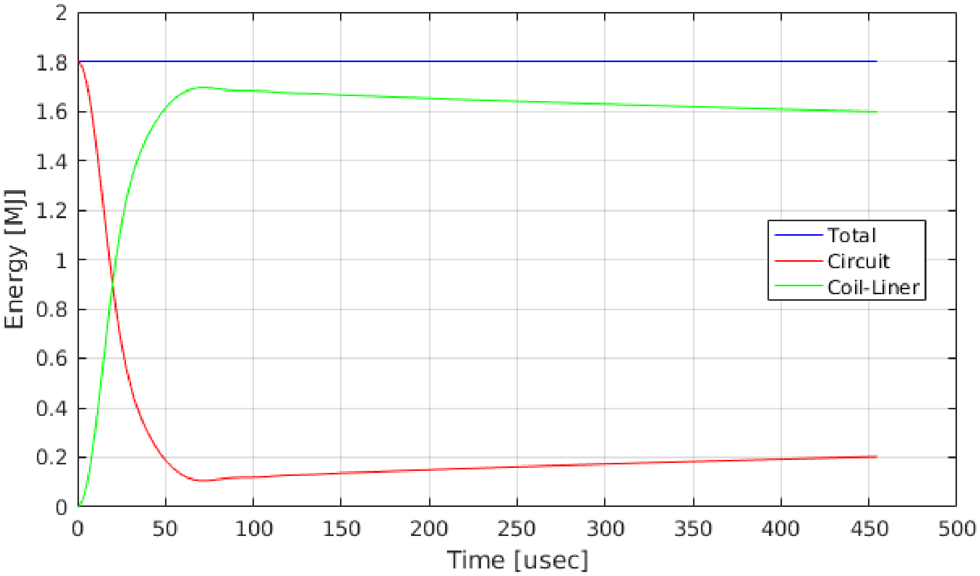

Figure 5.14: Time dependent total energy breakdown for the optimized design point

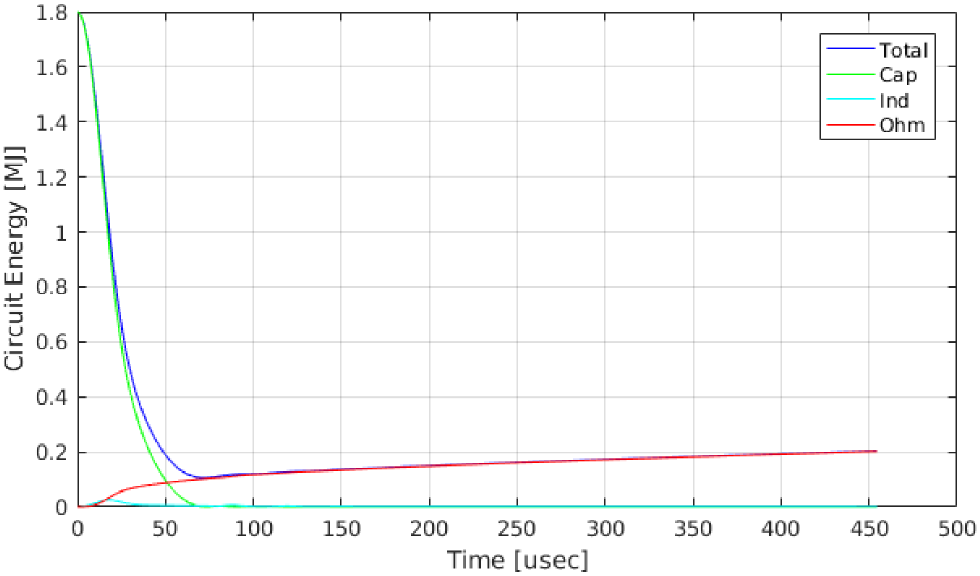

Figure 5.15: Time dependent circuit energy breakdown for the optimized design point

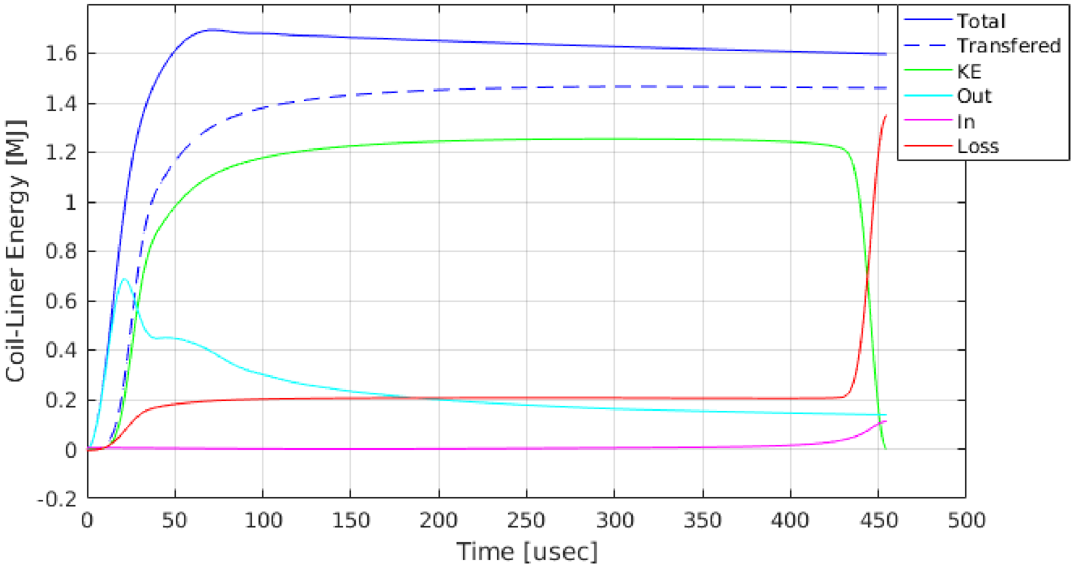

Figure 5.16: Time dependent coil-liner system energy breakdown for the optimized design point

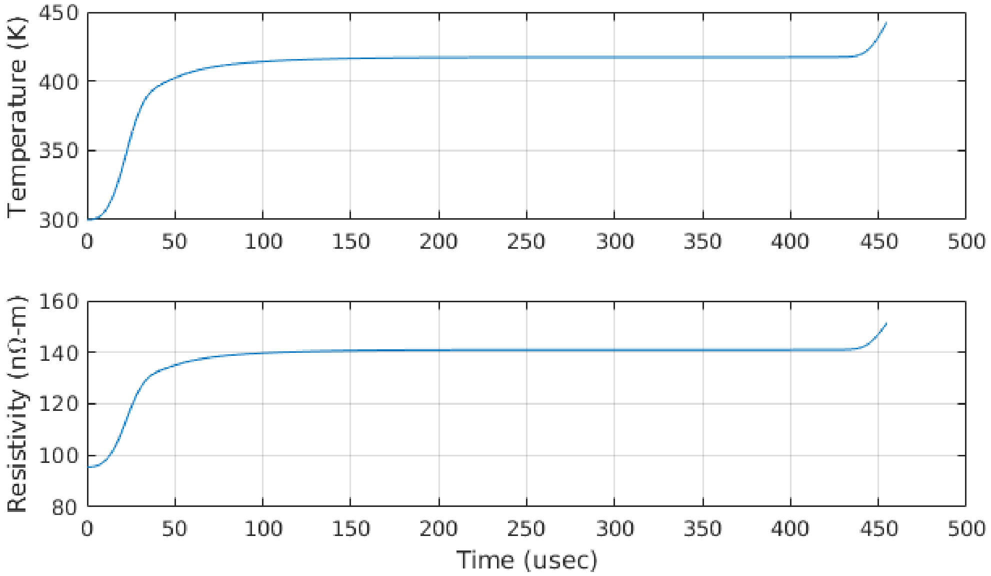

Figure 5.17: Time dependent liner temperature (top) and time dependent liner resistivity (bottom) for the optimized design point

Chapter 6

FEASIBILITY OF THE OPTIMIZED DESIGN

Feasibility of the optimized design of the liner compression driver system is discussed in this chapter. In particular, the liner implosion stability and the design requirements for the driver coil are analyzed to verify whether the current design can be implemented in practice.

6.1 Liner Implosion Stability

In order to ensure that the present design is applicable to the Fusion Driven Rocket (FDR), the stability of the liner during the implosion process needs to be considered. Three of the most important instability encountered in the liner implosion process are Rayleigh-Taylor instability, elastic-plastic instability (buckling instability), and barrel distortion. The liner implosion symmetry is also important for the effective FRC compression. All three instabilities are considered in this section, and mitigation strategy against these instabilities are discussed.

6.1.1 Rayleigh-Taylor Instability

The Rayleigh-Taylor instability is experienced in imploding liners, when there is a phase transition from solid to liquid phase on the liner inner surface at the end of the implosion process. At the end of the implosion, due to rapidly increasing magnetic field in the inner region, the inner surface of the liner will liquefy and vaporize, as the skin current causes intense heating of the liner surface [21,22]. Since during the final phase of the liner implosion, the liner is being decelerated by the rapidly increasing magnetic field in the inner region, the familiar hydrodynamic Rayleigh-Taylor instability is experienced, where the vaporized surface interacts with the massless “magnetic field fluid” [8].

To control Rayleigh-Taylor instability, it has been shown in the past by Turchi et al. that use of rotation can fully stabilize the liner against this instability mode [23]. Detailed theory on the stabilization of Rayleigh-Taylor modes has also been worked out by Turchi in ref [21] and ref [22]. By applying a finite rotation to the liner during or before the implosion process, Rayleigh-Taylor instability can be suppressed, and uniform layer of the stabilized liquid metal can be present in the inner surface of the liner, allowing for better conducting surface to confine the injected FRC [18].

It was also seen in the parametric analysis, that development of the Rayleigh-Taylor instability can be delayed by avoiding premature melting of the liner during the acceleration and coasting phase of the liner implosion. By delaying the reversal of the magnetic field magnitude at the liner interface, heating of the liner surface can be delayed, until the final deceleration phase. To accomplish this, it was seen that using initial negative bias in the inner region helps to reduce heating in the liner. The use of a negative bias also has an advantage of ensuring smaller trapped flux in the liner, such that injection of FRC is not obstructed by the the flux trapped in the liner.

6.1.2 Buckling Instability and Barrel Distortion

Buckling instability can be experienced by a solid liner in two stage of the implosion process. In the initial acceleration phase of the liner compression where the magnetic pressure is still small and the liner still retains its elastic property, liner can violate buckling stability criteria predicted from the liner elastic theory [14]. The second buckling instability occurs in the coasting and deceleration phase of the liner implosion process, where the circumference of the liner is reduced due to the radially inward momentum of the liner. In this phase, plastic stress that persist in the liner can cause violation of buckling stability criteria [22]. In both cases, buckling instability can cause cylindrical wall to fold into bellows and folds rather than increasing the thickness of the liner [14].

Since the liner implosion speed necessary for the FDR is of order of few km/sec, the first case of the instability is not encountered, since the magnetic pressure is applied so quickly that yield strength of the material is exceeded much quicker than the time required for elastic buckling instability to develop. However, the second case of the instability cannot be avoided, since the liner must spend significant time coasting in the FDR thruster, because the initial radius of the liner is typically much larger than the FRC injection radius.

The formation of the bellows is not detrimental to the success of the FDR and the fusion based on inductively driven liner compression (IDLC), since the bellows eventually collapse onto each other and they form a single solid shell that confine the FRC. Increased loss of magnetic flux due to the presence of bellows is also not a concern, since additional flux is added naturally through the FRC injection process. Thus, ability to control the formation and mode of the buckling instability is a key to ensure a good confinement of a FRC.

Barrel distortion is caused due to axial ends of the liner having lower stiffness than at the center, allowing the ends to fold radially inwards. For most cases, since the outer magnetic pressure is function of the shorted cross-section, the barrel distortion is naturally damped out, since more rapid increase in the radial location causes more rapid decay in the external magnetic pressure. Thus, barrel distortion is not the major problem for a successful liner compression, but ability to control its magnitude is desired to ensure a more controlled implosion process.

One way to control both the radial buckling and the barrel distortion in the liner during the liner implosion process is to introduce a small pleating (bends) in the liner. The effect of adding pleating has been studied in the past using ANSYS Explicit Dynamics® and was shown to give predictable folding pattern for the liner [15]. Alternatively, same effect can be realized when a small periodic modulation in liner thickness is present. This approach has an advantage over the pleating method in that only inner surface of the liner need to have a thickness modulation profile, while the outer surface of the liner can be kept smooth. Having outer surface of the liner smooth helps in the initial acceleration phase of the liner, and helps increase the coupling between the driver coil and the liner.

To verify the effect of the thickness modulation, ANSYS Explicit Dynamics® solver is used to determine the time dependent liner evolution. A temporal pressure profile is exported from the 1D liner code to the explicit dynamics solver (shown in Fig. 6.1). Aluminum liner is used for the testing purpose with mean radius of 14.5 cm, mean liner thickness of 30 mil, and axial length of 7.5 cm. Aluminum is modeled as a homogeneous linear elastic material with bilinear isotropic hardening model. Density of 2.77 g/cc, Young's modulus of 71 GPa, Poisson's ratio of 0.33, yield strength of 280 MPa, and tangent modulus of 500 MPa is used. The liner self-contact is assumed to be frictionless in the analysis.

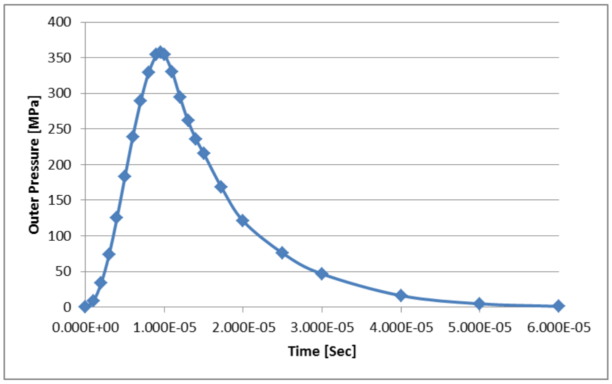

Figure 6.1: Temporal pressure profile applied to the external outer surface of the liner in ANSYS Explicit Dynamics® solver.

The resulting axial snapshot of the liner evolution that was calculated in ANSYS Explicit Dynamics® solver for the case without thickness modulation and with the thickness modulation is shown in Fig. 6.2. It can be seen from the figure that in the solid liner case, the liner experiences large barrel distortion during the compression process, as the ends of the liner folds radially inwards. The azimuthal buckling also occurs during the end of the implosion process with poor azimuthal symmetry in the buckling lines. On the other hand, for the case with the thickness modulation, the thickness modulation trips the liner into a fixed mode shape early in the compression process. The azimuthal symmetry is conserved during the implosion process, due to the early transition to a fixed mode shape defined by the periodicity of the thickness modulation. There are no barrel distortion for the modulated thickness case, since the development of the early mode shape allows for stiffer response against a barrel distortion.

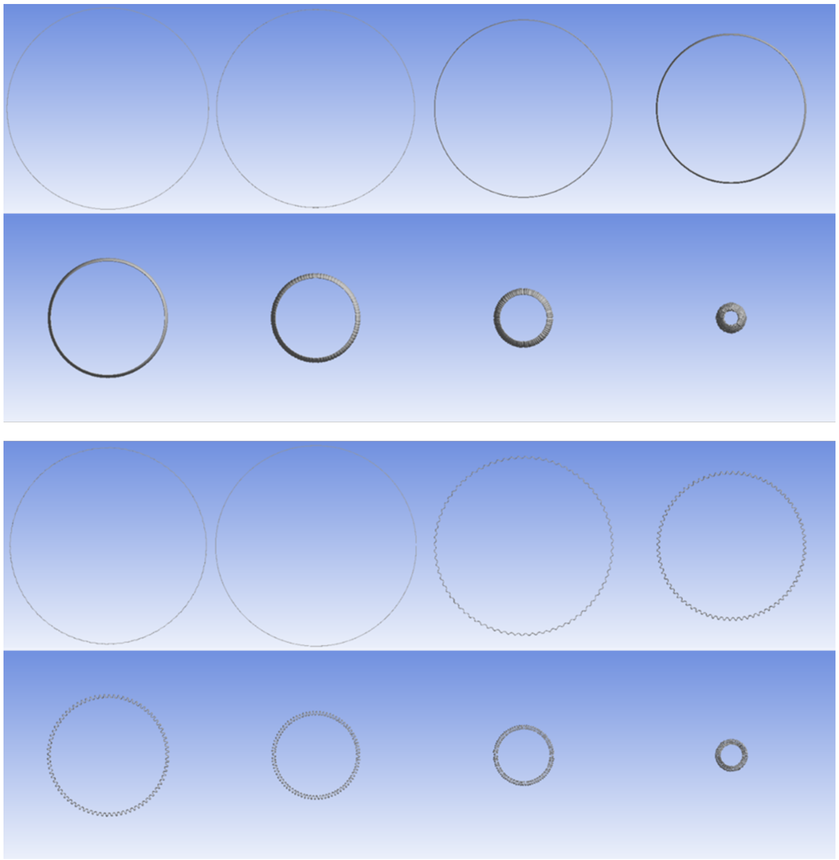

Figure 6.2: Cross-section of liner evolution as function of time (in ten µsec intervals starting at zero) for solid liner (top) and modulated liner (bottom). Liner has mean radius of 14.5 cm, mean liner thickness of 30 mil, and axial length of 7.5 cm. Modulation thickness with periodicity of 4.5° and modulation intensity of ±95.25 µm is used for modulated liner case.

Multiple modulation configurations were also tested in ANSYS Explicit Dynamics® solver to see how large of a modulation is necessary to obtain the desired symmetric folding pattern early in the liner implosion process. Sample configurations that gave decent results are shown in Table 6.1. From the analysis, it was seen that desired modulation intensity is approximately 10% of the liner thickness for the cases tested. If the modulation intensity is too high, then the liner experiences premature failure in the thinner region and the magnetic pressure can pierce through the liner surface. Using smaller modulation also gave acceptable results, but the effectiveness of early mode shape development was seen to diminish. From the analysis, the optimal periodicity of the modulation seemed to correspond to the mode number of the natural buckling pattern that develops in the case of the solid liner case.

A summary of the maximum kinetic energy and the conversion efficiency for the sample configurations is shown in Table 6.2. Result from the 1D liner code and from the solid liner case is also shown for comparison purposes. It can be seen that using modulated thickness not only helps against buckling instability and barrel distortion, but also helps in reducing the losses from the internal mechanical energy of the liner.

Configuration	**Modulation intensity [μm]**	**Modulation Angular Period [deg]**	**Modulation Geometry**
Case 1	95.25 (out) 0 (in)	1.5° (out) 5.7° (in)	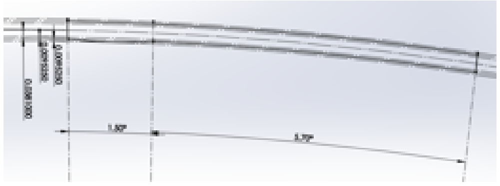
Case 2	95.25 (out) 0 (in)	0.75° (out) 2.85° (in)	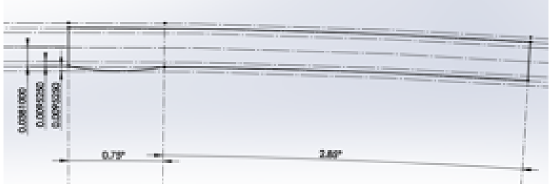
Case 3	95.25 (out) 95.25 (in)	1.8° (out) 1.8° (in)	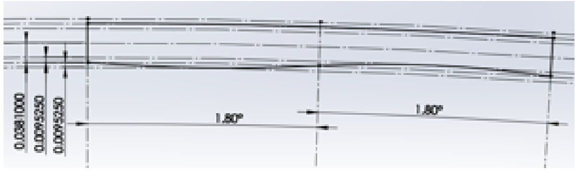
Case 4	95.25 (out) 95.25 (in)	2.25° (out) 2.25° (in)	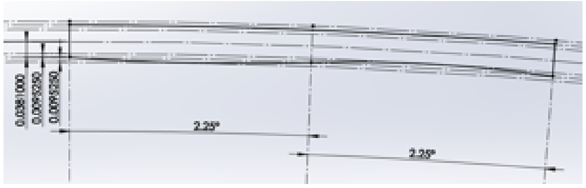

Table 6.1: Summary of liner modulation geometries for the cases tested

Configuration	**Liner Mass (g)**	**Work Done (kJ)**	**Max Kinetic Energy (kJ)**	**Conversion Efficiency (%)**	**Effective Velocity (m/s)**
1D Liner	144.23	370.61	370.61	100	2267.0
Solid	144.23	390.84	369.30	94.49	2263.0
Case 1	146.71	384.82	380.53	98.89	2277.6
Case 2	146.72	385.39	379.73	98.53	2275.1
Case 3	144.22	385.94	381.79	98.92	2301.0
Case 4	144.22	376.81	373.61	99.15	2285.3

Table 6.2: Comparison of the maximum kinetic energy and the conversion efficiency of the various modulated liner configurations

6.2 Design Requirements for Driver Coil

Due to significant magnetic field that develops in the shorted region, the design requirement for the driver coil must be considered. Namely, the structural and the thermal aspect of the driver coil design must be considered, since the shorted magnetic field that implode the liner also exerts significant magnetic pressure to the surface of the driver coil, and the Joule heating due to the mega-ampere current that flows in the driver coil produces heating at the driver coil inner surface.

6.2.1 Thermal Consideration

Assuming that the heating due to ohmic loss in the driver coil occurs only at the surface of the driver coil (due to skin-depth effects), then the heat release at the driver coil surface can be approximated using the formula by Shneerson as

$$q'(r_{wall}) = \vartheta \frac{B_m^2}{2\mu_0} \tag{6.1}$$

where $q'(r_{wall})$ is the volumetric heat released to the coil inner radius due to Joule heating, B_m is the peak magnetic field amplitude, and ϑ is a constant that depends on the pulse shape, where its value is equal to $\vartheta = 2.42$ if the pulse is half-wave of sinusoid and $\vartheta = 2.84$

if it can be expressed as $B_e = B_m(t/t_m)\exp(1 - t/t_m)$ [14]. Then, the temperature increase in the driver coil inner surface can be estimated to be

$$\Delta T = \vartheta \frac{B_m^2}{2\mu_0 C_v} \tag{6.2}$$

where C_v is the volumetric heat capacity.

Assuming that the driver coil is made of aircraft grade aluminum, aluminum 7075-T6, which has been used in the past liner compression experiments for FDR [18], the volumetric heat capacity is $C_v = 2.7 \times 10^6$ J/m^3-K. From the result of the optimized design, it was seen that the peak magnetic field in the shorted region is 11.24 T. From the obtained time dependent magnetic field profile for the optimum design, the pulse shape approximately has shape described by equation $B_e = B_m(t/t_m)\exp(1 - t/t_m)$. Thus, ϑ can be estimated to be $\vartheta = 2.84$. Under these assumptions, the heating in the driver coil surface can be estimated to be $\Delta T = 52.9$ K, which is not large enough to be a concern for the driver coil surface melting through, since the melting temperature of Aluminum 7075-T6 is approximately 750 K. Thus, as long as care is taken to allow enough time between the thruster pulses for the driver coil to cool off through conduction and radiation processes, then there should not be an issue associated with the driver coil melting for the optimized design.

Another potential issue related with heating of the driver coil is the thermoelastic effect on the driver coil inner surface. Again, using the thin skin layer thickness assumption, the thermoelastic stress in the driver coil inner surface can be estimated using the formula by Shneerson as

$$\sigma_{th} = \sigma_\phi(r_{wall}) = \sigma_z(r_{wall}) = -\frac{\alpha_0 E \Delta T}{(1 - \nu)} \tag{6.3}$$

where α_0 is the thermal expansion coefficient, E is the Young's modulus, and ν is the Poisson's ratio.

For Aluminum 7075-T6, the thermal expansion coefficient is typically $\alpha_0 = 23.6$ µ/K, the Young's modulus is $E = 71.7$ GPa, and the Poisson's ratio is $\nu = 0.33$. Thus, the expected thermoelastic stress on the driver coil inner surface is $\sigma_{th} = -133.6$ MPa, which is too large to be neglected. Thus, non-negligible thermoelastic stress is obtained, which means that in the structural consideration of the driver coil, the thermoelastic effect must be considered. Fortunately, the time of peak thermoelastic stress typically do not overlap with the time of peak mechanical stress due to the magnetic pressure [14]. This is due to the fact that the thermoelastic stress only develops after the heating has completed, which is near the end of the pulse, while the mechanical stress due to the magnetic pressure typically peaks at the time of the peak magnetic field, which occurs much earlier.

6.2.2 Structural Consideration

Due to the high magnetic field experienced in the shorted region, structural issues associated with the driver coil must be considered. Since loading due to the magnetic field only acts in a thin skin depth, $j \times B$ loading can be approximated as a surface magnetic pressure loading inside a driver coil cylinder. From definition of magnetic pressure

$$p_B = \frac{B^2}{2\mu_0} \tag{6.4}$$

one can calculate a peak magnetic loading on the driver coil surface of 50.3 MPa for the optimized design. One can see that this is not too significant of a loading on the driver coil, and there should not be significant issue dealing with magnetic field containment. Since time of peak magnetic field is 21.5 µsec for the optimized design point, the pulse time is sufficient short such that dynamic containment phenomena are expected to help reduce the effective peak stress experienced by the driver coil [8, 14]. Using the dynamic stress formula by Shneerson, the effective dynamic stress on the coil inner surface can be calculated to be

$$\sigma_m = \frac{p_B \tau_{eff}}{r_{wall}(\mathcal{R} - 1)\sqrt{\rho_m}} \tag{6.5}$$

where σ_m is the effective dynamic stress, τ_{eff} is the effective pulse time, $\mathcal{R} = r_{ext}/r_{wall}$ is the radius ratio of the outer radius of the driver coil to the inner radius, and ρ_m is the mass density.

Since the time of peak magnetic field is 21.5 µsec, the effective pulse time can be estimated to be $\tau_{eff} = 43$ µsec. Assuming Aluminum 7075-T6, mass density is $\rho_m = 2810$ kg/m^3. Assuming $\mathcal{R} = 1.25$, the effective dynamic stress at the coil inner surface can be calculated to be $\sigma_m = 163$ MPa, which is not an issue for Aluminum 7075-T6, which has typical yield strength value of 500 MPa.

To obtain the estimate for a worst possible condition, a linear elastic static assumption can be used to estimate the upper bound of the stress experienced in the coil. The solution to a thick cylinder with a pressure applied from the inside is well known, and the radial and the azimuthal stress at the driver coil inner surface (location of peak stress) can be calculated to be

$$\sigma_r = -p_B \tag{6.6}$$

$$\sigma_\phi = \frac{\mathcal{R}^2 + 1}{\mathcal{R}^2 - 1} p_B \tag{6.7}$$

where σ_r and σ_ϕ are the radial and azimuthal stress at the driver coil inner surface, respectively. For the case neglecting thermoelastic effects, the von Mises stress,

$$\sigma_v = \sqrt{\frac{1}{2}\left[(\sigma_\phi - \sigma_z)^2 + (\sigma_\phi - \sigma_r)^2 + (\sigma_z - \sigma_r)^2\right]} \tag{6.8}$$

can be calculated to gain effective stress at the driver coil inner surface.

Assuming $\sigma_z = 0$ and $\mathcal{R} = 1.25$, von Mises stress of $\sigma_v = 258$ MPa can be obtained, which is greater than the result calculated for the dynamic containment case, but still is roughly half of the yield value for Aluminum 7075-T6. Thus neglecting thermoelastic effect, it can be seen that by using a driver coil radius ratio of 1.25, driver coil should not fail.

Accounting for the case when the effect of thermoelastic stress and the mechanical stress happens to overlaps, the stress at the inner surface of the driver coil can be estimated to be

$$\sigma_r = -p_B \tag{6.9}$$

$$\sigma_\phi = \frac{\mathcal{R}^2 + 1}{\mathcal{R}^2 - 1} p_B + \sigma_{th} \tag{6.10}$$

$$\sigma_z = \sigma_{th} \tag{6.11}$$

which, again, assuming $\mathcal{R} = 1.25$, von Mises stress of $\sigma_v = 200$ MPa can be obtained.

As it can be seen, when the dynamics effects of the coil is accounted, lower radius ratio is potentially possible due to lower peak stress due to the dynamic containment effect that helps to reduce the peak effective load experienced by the driver coil. However, even static liner elastic calculation shows that the driver coil can handle the load, which is comforting. While a coil outer radius of 1.25 m is not desirable, it is still engineeringly feasible to construct such a driver coil and launch it into space. Thus, the magnetic field magnitude required to compress the liner is definitely containable by the driver coil using present technologies.

Chapter 7

CONCLUSION AND FUTURE PLANS

The 1D liner code was developed in this study to identify the optimum system configuration for the inductively driven liner compression (IDLC) driver system for the Fusion Driven Rocket (FDR). The results from the 1D liner code was verified against a commercial SPICE circuit code and a commercial structural explicit dynamic code, and it was verified that the 1D liner code correctly captures the liner dynamics excepts for the deceleration phase of the liner implosion, which is not crucial for this optimization study.

Using the 1D liner code, a parametric analysis was conducted to identify the optimum design point for the IDLC driver system for the FDR using the proposed dimension and configuration of the FDR. In the parametric analysis, it was determined that the liner thickness of 40 mil corresponded to the optimum mass for a lithium liner that gives the desired IDLC driver system performance. It was seen that maximizing capacitor voltage was crucial in improving the performance of the driver system for a fixed capacitive energy stored in the capacitor bank. A minimization of the stray inductance and resistance was also seen to be important for the tested configuration. A slightly negative seed bias flux was also seen to improve the performance of the IDLC driver coil. It was seen that the negative bias also reduced the chance of the liner melting during the acceleration and the coasting phase of the implosion process. The bank voltage of 50 kV and the initial seed bias of -0.2 Wb was identified as an optimal design point that is still engineeringly feasible. The energy coupling of 69.7 % and the estimated fusion gain of 7.43 was obtained from the optimized design for a fixed capacitor bank energy of 1.8 MJ.

Feasibility of the optimized design was also discussed, which offered solutions to ensure good liner implosion stability and symmetry. Some design requirements for driver coils were analyzed, and it was seen that the requirement for the driver coil is feasible with today's technology. Use of a liner rotation and a liner thickness variation is most likely necessary in practice to ensure good liner stability, but this is not a significant road block to the development of the FDR. Furthermore, while the high magnetic field and mega-ampere current flow does cause challenges to the design of driver coil, it should be possible to design a functioning driver coil without use of any exotic materials.

While the present model captures the initial acceleration phase of the liner compression well, it was seen that the deceleration phase of the implosion process is not captured well in the model. In order to capture the deceleration phenomena, more advanced equation of state model for liner must be considered, accounting for the liner compressibility, internal mechanical energy loss, and potential phase change. Furthermore, detailed interaction between the liner, magnetic field, and FRC must also be accounted in the model to capture the influence of the injected FRC to the dynamics of the liner compression. Improvements to the liner code is currently planned to couple a one-and-quarter dimension FRC transport code that can handle a moving boundary to study the effect of FRC and liner interaction to further the understanding of the physics of fusion based on IDLC and to obtain better estimate for the FDR performance.

BIBLIOGRAPHY

[1] S. G. Alikhanov, V. G. Belan, G. I. Budker, V. N. Ivanchenko, and G. N. Kichigin. Creation of megagauss fields by the method of magnetodynamic accumulation. *Soviet Atomic Energy*, 23(6), 1967.

[2] T. C. Chi. Electrical resistivity of alkali elements. *Journal of Physical and Chemical Reference Data*, 8(2), 1979.

[3] E. C. Cnare. Magnetic flux compression by magnetically imploded metallic foils. *Journal of Applied Physics*, 37(10), 1966.

[4] P. D. Desai, H. M. James, and C. Y. Ho. Electrical resistivity of aluminum and manganese. *Journal of Physical and Chemical Reference Data*, 13(4), 1984.

[5] B G. Drake. Human exploration of mars design reference architecture 5.0. Technical Report NASA/SP2009566, Mars Architecture Steering Group NASA Headquarters, July 2009.

[6] M. D. Griffin and J. R. French. *Space Vehicle Design.* AIAA education series. American institute of aeronautics and austronautics, 2004.

[7] R. G. Jahn. *Physics of Electric Propulsion.* Dover Publication Inc, 2006.

[8] H. Knoepfel. *Pulsed High Magnetic Fields: Physical Effects and Generation Methods concerning Pulsed Fields up to the Megaoersted Level.* North-Holland, London, 1970.

[9] Y. H. Matsuda, F. Herlach, S. Ikeda, and N. Miura. Generation of 600 t by electromagnetic flux compression with improved implosion symmetry. *Review of Scientific Instruments*, 73(12), 2002.

[10] R. A. Matula. Electrical resistivity of copper, gold, palladium, and silver. *Journal of Physical and Chemical Reference Data*, 8(4), 1979.

[11] N. Miura and H. Nojiri. Recent advances in megagauss physics. *Physica B: Condensed Matter*, 216(34):153 – 157, 1996. Proceedings of the International Workshop on Advances in High Magnetic Fields.

[12] A. Pancotti, J. Slough, D. Kirtley, M. Pfaff, C. Pihl, and G. Votroubek. Mission design architecture for the fusion driven rocket. In *48th AIAA Joint Propulsion Conference*, July 2012.

[13] A. Pancotti, J. Slough, and A. Shimazu. Mars mission trade studies and technology development of a 36 mw fusion rocket. In *Joint Conference of 30th International Symposium on Space Technology and Science, 34th International Electric Propulsion Conference, and 6th Nano-satellite Symposium*, July 2015.

[14] G. A. Shneerson, M. I. Dolotenko, and S. I. Krivosheev. *Strong and Superstrong Pulsed Magnetic Fields Generation*. Walter de Gruyter, Berlin/Boston, 2014.

[15] J. Slough, A. Pancotti, and D. Kirtley. Analysis of inductively driven liners for the generation of megagauss magnetic fields. In *Magnetic Field Generation and Related Topics (MEGAGUSS), 2012 14th International Conference on Megagauss*, Oct 2012.

[16] J. Slough, A. Pancotti, D. Kirtley, C. Pihl, and M. Pfaff. Nuclear propulsion through direct conversion of fusion energy: The fusion driven rocket (phase 1 final report) - NASA grant: NNX12AR39G, 2012.

[17] J. Slough, A. Pancotti, D. Kirtley, and G. Votroubek. Electromagnetically driven fusion propulsion. In *33rd International Electric Propulsion Conference*, October 2013.

[18] J. Slough, A. Pancotti, and A. Shimazu. The fusion driven rocket: Nuclear propulsion through direct conversion of fusion energy (phase 2 final report) - NASA grant: NNX12AR39G, 2015.

[19] D. Steinberg. *Equation of State and Strength Properties of Selected Materials*. UCRL-MA. Lawrence Livermore National Laboratory, 1996.

[20] S. Takeyama and E. Kojima. A copper-lined magnet coil with maximum field of 700t for electromagnetic flux compression. *Journal of Physics D: Applied Physics*, 44(42):425003, 2011.

[21] P. J. Turchi. Imploding liner compression on plasma: Concepts and issues. *IEEE Transactions on Plasma Science*, 36(1), 2008.

[22] P. J. Turchi. Liner stability problems for megagauss fusion. *IEEE Transactions on Plasma Science*, 43(1), 2015.

[23] P. J. Turchi, A. L. Cooper, R. Ford, and D. J. Jenkins. Rotational stabilization of an imploding liquid cylinder. *Phys. Rev. Lett.*, 36:1546–1549, Jun 1976.

Appendix A

MATLAB® IMPLEMENTATION OF THE 1D LINER CODE

A.1 liner.m

```
close all
clear all
clc

mu0 = pi*4e-7;

% Read in Run cases
[ss, circ, md, cl] = liner_startup('solver_setting.txt');

% Initialize
[circ, cl, E] = liner_init(circ, cl, md, ss.dpt);
t = zeros(1, ss.dpt);
dt = ss.tsc.dt;

% Counters and Loop Trips
BfieldReversal=false;
LagrangianAdaptive = false;
frc_trig = true;         % Set to false for FRC-Flux injection
   frc_flux = 10e-3;     % [Wb]
   frc_time = 70e-6;     % [sec]

% Data Stream
if ss.dts.case
    fprintf('n: %g;   dt: %g sec;   Time: %g sec;   R_out: %g mm\n', ...
        1, dt, t(1), cl.r.out(1)/1e-3)
end


for n = 2:ss.dpt

    t(n)=t(n-1)+dt;

    % Circuit Calculation
    circ = circ.solver(circ, dt, n, t(n));

    % Compute Energy Based on Result from Circuit Equation Solver
    E = solv_E_cbar(E, circ, dt, n);
```

```
% Static Liner Calculation
cl.flux.net(n) = circ.Ls(n-1)*circ.I2(n);
delta_flux = cl.flux.net(n) - cl.flux.net(n-1);
cl.flux.out(n) = cl.flux.out(n-1) + delta_flux;
cl.B.out(n) = cl.flux.out(n)*cl.CA(n-1);

% Static Breed-through Calculation
tau = cl.liner.L(n-1)/(cl.liner.R(n-1));

if cl.B.out(n) > cl.B.in(n-1)
    bt_flux = (dt/tau)*(cl.B.out(n)-cl.B.in(n-1))/cl.CA(n-1);
    cl.flux.out(n) = cl.flux.out(n) - bt_flux;
    cl.flux.in(n) = cl.flux.in(n-1) + bt_flux;

    cl.B.out(n) = cl.flux.out(n)*cl.CA(n-1);
    cl.B.in(n) = cl.flux.in(n)*cl.CB(n-1);
else
    bt_flux = (dt/tau)*(cl.B.out(n) - cl.B.in(n-1))/cl.CB(n-1);
    cl.flux.out(n) = cl.flux.out(n) - bt_flux;
    cl.flux.in(n) = cl.flux.in(n-1) + bt_flux;

    cl.B.out(n) = cl.flux.out(n)*cl.CA(n-1);
    cl.B.in(n) = cl.flux.in(n)*cl.CB(n-1);
end

% Temperature Calculation
cl.liner.I(n) = (cl.w/mu0)*(cl.B.out(n)-cl.B.in(n));
delta_U_therm = cl.liner.R(n-1)*(cl.liner.I(n)^2)*dt;

if cl.T(n-1) < md.tlq
    cl.T(n) = cl.T(n-1) + delta_U_therm/(md.sph*cl.m);
    if cl.T(n) >= md.tlq
        E.U_latent = (cl.T(n) - md.tlq)*(md.sph*cl.m);
        cl.T(n) = md.tlq;
    end
elseif cl.T(n-1) == md.tlq
    E.U_latent = E.U_latent + delta_U_therm;
    cl.T(n) = md.tlq;
    if E.U_latent > md.lhf*cl.m
        cl.T(n) = cl.T(n-1) ...
            + (E.U_latent - md.lhf*cl.m)/(md.sph*cl.m);
        E.U_latent = 0;
    end
elseif cl.T(n-1) > md.tlq && cl.T(n-1) < md.tvp
    cl.T(n) = cl.T(n-1) + delta_U_therm/(md.sph*cl.m);
    if cl.T(n) >= md.tvp
        E.U_latent = (cl.T(n) - md.tvp)*(md.sph*cl.m);
        cl.T(n) = md.tvp;
    end
```

```
elseif cl.T(n-1) == md.tvp
    E.U_latent = E.U_latent + delta_U_therm;
    cl.T(n) = md.tvp;
    if E.U_latent > md.lhv*cl.m
        cl.T(n) = cl.T(n-1) ...
            + (E.U_latent - md.lhv*cl.m)/(md.sph*cl.m);
        E.U_latent = 0;
    end
elseif cl.T(n-1) > md.tvp
    cl.T(n) = cl.T(n-1) + delta_U_therm/(md.sph*cl.m);
end

if cl.T(n) <= md.tlq
    cl.liner.rstv(n) = ppval(md.T1,cl.T(n));
elseif cl.T(n) > md.tlq
    cl.liner.rstv(n) = ppval(md.T2,cl.T(n));
end

if cl.case.vacuum
    cl.liner.rstv(n) = cl.liner.rstv(n-1);
end

% Dynamic Calculation
cl.p.out(n) = (cl.B.out(n)^2)/(2*mu0);
cl.p.in(n) = (cl.B.in(n)^2)/(2*mu0);

cl.F(n) = 2*pi*cl.w*(cl.p.out(n)*cl.r.out(n-1) ...
    - cl.p.in(n)*cl.r.in(n-1));
cl.a(n) = cl.F(n)/cl.m0;

if cl.case.vacuum
    cl.v(n) = 0;
else
    cl.v(n) = cl.v(n-1) + cl.a(n)*dt;
end

cl.r.out(n) = cl.r.out(n-1) - cl.v(n)*dt;
cl.r.in(n) = sqrt((cl.r.out(n)^2) - ((cl.r.out(1)^2)-(cl.r.in(1)^2)));
cl.th(n) = cl.r.out(n) - cl.r.in(n);

delta_KE = 0.5*cl.m0*(cl.v(n)^2 - cl.v(n-1)^2);

% Determine key parameters for the next step
circ.Ls(n) = ppval(cl.LSf,cl.r.out(n));
cl.liner.L(n) = ppval(cl.LLf,cl.r.out(n));

cl.CA(n) = ppval(cl.CAf,cl.r.in(n));
if cl.r.in(n)/cl.r.wall <=0.01
    cl.CB(n) = 1/(pi*cl.r.in(n)) + ppval(cl.CBf,0.01*cl.r.wall) ...
        - (0.01^2)/(pi*(cl.r.wall^2));
```

```
else
    cl.CB(n) = ppval(cl.CBf,cl.r.in(n));
end

E.sys.KE(n) = 0.5*cl.m0*cl.v(n)^2;
E.sys.out(n) = 0.5*(cl.flux.out(n)^2/circ.Ls(n));

delta_Ein = 0.5*(cl.flux.in(n)^2/cl.liner.L(n) ...
    - cl.flux.in(n-1)^2/cl.liner.L(n-1));

% Only carry out Energy balance if liner velocity is radially in
if cl.v(n) > 0
    if delta_KE > 0
        if cl.B.out(n) < cl.B.in(n)
            circ.Ra(n) = delta_KE ...
                - E.sysc.dL(n) + E.sysc.dL(n-1);
            delta_Ein = delta_Ein - delta_U_therm;
            E.sys.loss(n) = E.sys.loss(n-1);
        else
            circ.Ra(n) = delta_U_therm + delta_KE ...\
                - E.sysc.dL(n) + E.sysc.dL(n-1);
            E.sys.loss(n) = E.sys.loss(n-1) + delta_U_therm;
        end
    else
        if cl.B.out(n) < cl.B.in(n)
            delta_Eloss =  delta_KE + delta_U_therm;
            if delta_Eloss > 0
                delta_Ein = delta_Ein + delta_Eloss;
                E.sys.loss(n) = E.sys.loss(n-1);
            else
                E.sys.loss(n) = E.sys.loss(n-1) - delta_Eloss;
            end
        else
            E.sys.loss(n) = E.sys.loss(n-1) - delta_KE;
            circ.Ra(n) = delta_U_therm;
        end
    end
end

E.sys.in(n) = E.sys.in(n-1) + delta_Ein;
cl.flux.in(n) = sign(cl.flux.in(n))*sqrt(2*E.sys.in(n)*cl.liner.L(n));


E.sys.tot(n) = E.sys.out(n) + E.sys.in(n) + E.sys.KE(n) ...
    + E.sys.loss(n);

if circ.Ra(n)
    circ.Ra(n) = circ.Ra(n) - (E.circ.sys(n) - E.sys.tot(n));
    circ.Ra(n) = circ.Ra(n) / (dt*circ.I2(n)^2);
else
```

```
    E.sys.loss(n) = E.sys.loss(n) + (E.circ.sys(n) - E.sys.tot(n));
    E.sys.tot(n) = E.sys.out(n) + E.sys.in(n) + E.sys.KE(n) ...
        + E.sys.loss(n);
end

if BfieldReversal == false
    cl.liner.R(n) = cl.liner.rstv(n)*(pi/cl.w) ...
        * (cl.r.out(n)+cl.r.in(n))/(cl.r.out(n)-cl.r.in(n));
else
    SD = sqrt(cl.liner.rstv(n)/(pi*freq*mu0*(1+cl.liner.rstv(n))));
    if cl.th(n) > 2*SD
        cl.liner.R(n) = cl.liner.rstv(n)*(pi/cl.w) ...
            *(2*cl.r.in(n)+2*SD)/(2*SD);
        cl.m = md.den*pi*((cl.r.in(n)+2*SD)^2-cl.r.in(n)^2)*cl.w;
    else
        cl.liner.R(n) = cl.liner.rstv(n)*(pi/cl.w) ...
            * (cl.r.out(n)+cl.r.in(n))/(cl.r.out(n)-cl.r.in(n));
    end
end

if t(n) > frc_time && ~frc_trig
    frc_trig = true;
    delta_Ein = 0.5*((cl.flux.in(n)+frc_flux)^2/cl.liner.L(n) ...
        - cl.flux.in(n)^2/cl.liner.L(n));
    E.sys.in(n) = E.sys.in(n) + delta_Ein;
    cl.flux.in(n) = cl.flux.in(n) + frc_flux;

    E.sys.tot(n) = E.sys.tot(n) + delta_Ein;
    E.circ.sys(n) = E.circ.sys(n) + delta_Ein;
    fprintf('FRC Injected\n')
end


% Correction to magnetic field due to dynamic liner change
cl.B.out(n) = cl.flux.out(n)*cl.CA(n);
cl.B.in(n) = cl.flux.in(n)*cl.CB(n);

if ss.tsc.case
    if n > 2
        if abs(cl.B.in(n) - cl.B.in(n-1)) > ss.tsc.dltB
            dt = dt*(1-ss.tsc.dltT);
            n = n-1; %#ok<FXSET>
            LagrangianAdaptive = true;
        else
            dt = dt*(1+ss.tsc.dltT);
            LagrangianAdaptive = false;
        end
        if dt > ss.tsc.dtmx
            dt = ss.tsc.dtmx;
        end
```

```
        if dt < ss.tsc.dtmn
            dt = ss.tsc.dtmn;
        end
    end
end

% B-Field Strength reversal Check
if ~cl.case.vacuum
    if LagrangianAdaptive == false
        if BfieldReversal == false
            if cl.v(n) > 0
                if cl.B.in(n) >= cl.B.out(n)
                    BfieldReversal = true;
                    cl.t_Brev = t(n);
                    cl.B.rev = 0.5*(cl.B.in(n)+cl.B.out(n));
                    freq = cl.v(n)/(2*(cl.r.out(n)+cl.r.in(n)));
                end
            end
        end
    end
end


% End condition
if LagrangianAdaptive == false
    if isreal(cl.r.out) == false
        fprintf('Warning: Imaginary number detected.\n');
    end
    if  cl.v(n) < 0 && t(n) > 2e-5
        fprintf('Normal Completion of Analysis: Liner bounced back\n');
        break
    elseif cl.T(n) > md.Tmx
        fprintf(['Error: Maximum allowed Temperature Reached. ', ...
            'Analysis Terminated.\n']);
        break
    elseif cl.T(n) > md.tvp
        fprintf('Error: Liner vaporized. Analysis Terminated.\n');
        break
    elseif isnan(cl.r.out(n))
        fprintf('Error: NaN Detected. Analysis Terminated.\n');
        break
    end
end


% Data stream
if ss.dts.case
    if LagrangianAdaptive == false
        if mod(n,ss.dts.psp)-1 == 0
            fprintf(['n: %g;   dt: %g sec;   Time: %g sec;   ', ...
```

```
                    'R_out: %g mm;    R_in: %g mm;    B_in %g T\n'], ...
                    n, dt, t(n), cl.r.out(n)/1e-3, cl.r.in(n)/1e-3, ...
                    cl.B.in(n))
            end
        end
    end
end

E.tot.tot = E.tot.circ + E.sys.tot;



%% Command Window Output %%

fprintf('t_crowbar:     %g us\n',circ.cbtime/1e-6)
fprintf('Initial Bias:  %g Wb\n', cl.flux.in(1))
fprintf('Collapse Time: %g usec\n',t(n-1)/1e-6)
fprintf('t_reversal:    %g usec\n',cl.t_Brev/1e-6)
fprintf('Maximum B_in:  %g T\n', max(cl.B.in))
fprintf('Maximum Speed: %g m/s\n', max(cl.v))
fprintf('Final r_in:    %g mm\n',min(cl.r.in(1:n-1)*1000))
fprintf('Final thick:   %g mm\n',max(cl.th(1:n-1)*1000))
fprintf('KE/Bank:       %g %%\n',100*max(E.sys.KE)/E.circ.C(1))
fprintf('Final Temp:    %g K\n',cl.T(n-1))
fprintf('Final Flux_in: %g Wb\n',cl.flux.in(n-1))
fprintf('Gain: %g\n', 4.3e-8 * sqrt(cl.m0) * (max(E.sys.KE)^(11/8)))

%% Plots %%

plot_liner(t, circ, cl, E, n);
```

A.2 solv_circ_cbar.m

```
function circ = solv_circ_cbar(circ, dt, n, time)
% Solves the crowbar circuit for 1D Liner Code
%    circ = SOLV_CIRC_CBAR2(circ, dt, n, time) returns updated structure
%    circ with circuit parameter at current time step.
%
%
% Interpolate time dependent circuit quantities using previous step info
%    This value is used only for the circuit calculation. This value
%    should be updated later with true value.

% Bootstrap Calculation for case when n = 2
if (n == 2)
    % Compute local variable for the circuit calculation
    Rtot = circ.R1 + circ.R2 + circ.Rc;
    Ltot = circ.L1 + circ.L2 + circ.Ls(1);

    % Solve circuit equation for global circuit quantities
    circ.I1(2) = circ.Vc(1)/(Rtot + Ltot/dt);
    circ.I2(2) = circ.I1(2);

    circ.Vc(2) = circ.Vc(1) - (dt/circ.C)*circ.I1(2);

    return
end

% Solve circuit equation for global circuit quantities
if ~circ.cbtrig
    R_tot = circ.Ra(n-1) + circ.Rc + circ.R1 + circ.R2;
    L_tot = [circ.Ls(n-1) + circ.L2 + circ.L1, ...
        circ.Ls(n-2) + circ.L2 + circ.L1];
    tmp1 = circ.C*dt*circ.Vc(n-1) + circ.C*circ.I1(n-1)*L_tot(1);
    tmp2 = dt^2 + circ.C*R_tot*dt + 2*circ.C*L_tot(1) - circ.C*L_tot(2);

    circ.I1(n)  = tmp1 / tmp2;
    circ.I2(n)  = circ.I1(n);
    circ.Vc(n) = circ.Vc(n-1) - circ.I1(n)*dt/circ.C;

    % Check if the crowbar switch should be activated
    if circ.Vc(n) <= 0
        circ.cbtrig = true;
        circ.cbtime = time;
    end
else
    tmp13 = circ.C*(circ.L2+circ.Ls(n-1)+circ.L3)*circ.I2(n-1) ...
        - circ.C*circ.L3*circ.I1(n-1);
    tmp11 = -circ.C*circ.R3*dt-circ.C*circ.L3;
```

```
    tmp12 = circ.C*dt*(circ.R2+circ.Rc + circ.Ra(n-1)+circ.R3) ...
        + circ.C*(circ.L2+circ.L3+2*circ.Ls(n-1)-circ.Ls(n-2));

    tmp23 = circ.C*dt*circ.Vc(n-1) + circ.C*circ.L1*circ.I1(n-1) ...
        + circ.C*(circ.L2+circ.Ls(n-1))*circ.I2(n-1);
    tmp21 = dt^2 + circ.C*dt*circ.R1 + circ.C*circ.L1;
    tmp22 = circ.C*dt*(circ.R2+circ.Rc+circ.Ra(n-1)) ...
        + circ.C*(circ.L2+2*circ.Ls(n-1)-circ.Ls(n-2));

    circ.I1(n) = (tmp13*tmp22 - tmp12*tmp23)/(tmp11*tmp22 - tmp12*tmp21);
    circ.I2(n) = (tmp11*tmp23 - tmp13*tmp21)/(tmp11*tmp22 - tmp12*tmp21);
    circ.I3(n) = circ.I2(n) - circ.I1(n);

    circ.Vc(n) = circ.Vc(n-1) - circ.I1(n)*dt/circ.C;
end

return
```

A.3 solv_E_cbar.m

```
function E = solv_E_cbar(E, circ, dt, n)

% Computed Circuit Element Energy
E.circ.C(n) = 0.5*circ.C*(circ.Vc(n)^2);
E.circ.R1(n) = E.circ.R1(n-1) + circ.I1(n)^2*circ.R1*dt;
E.circ.R2(n) = E.circ.R2(n-1) + circ.I2(n)^2*circ.R2*dt;
E.circ.R3(n) = E.circ.R3(n-1) + circ.I3(n)^2*circ.R3*dt;
E.circ.Rc(n) = E.circ.Rc(n-1) + circ.I2(n)^2*circ.Rc*dt;
E.circ.L1(n) = 0.5*circ.L1*(circ.I1(n)^2);
E.circ.L2(n) = 0.5*circ.L2*(circ.I2(n)^2);
E.circ.L3(n) = 0.5*circ.L3*(circ.I3(n)^2);

% Total Circuit Energy by Component
E.circ.Ltot(n) = E.circ.L1(n) + E.circ.L2(n) + E.circ.L3(n);
E.circ.Rtot(n) = E.circ.R1(n) + E.circ.R2(n) + E.circ.R3(n) + E.circ.Rc(n);

% Total Energy Stored in the Circuit
E.tot.circ(n) = E.circ.C(n) + E.circ.Ltot(n) + E.circ.Rtot(n);


% Coil-Liner System Energy Predicted by Circuit as Circuit Component
E.sysc.L(n)  = 0.5*circ.Ls(n-1)*(circ.I2(n)^2);
if n > 2
    E.sysc.dL(n) = E.sysc.dL(n-1) ...
        + 0.5*(circ.I2(n)^2)*(circ.Ls(n-1)-circ.Ls(n-2));
end
E.sysc.R(n) = E.sysc.R(n-1) ...
    + 0.5*dt*circ.Ra(n-1)*(circ.I2(n)^2 + circ.I2(n-1)^2);

% Total System Energy Based on Energy Conservation
E.circ.sys(n) = E.circ.sys(n-1) + (E.tot.circ(n-1) - E.tot.circ(n));

% Circuit Energy Error
E.error(n) = E.circ.sys(n) - E.sysc.L(n) - E.sysc.dL(n) - E.sysc.R(n);

end
```

A.4 *liner_startup.m*

```
function [ss, circ, md, cl] = liner_startup(solvfile)
% LINER_STARTUP   Startup script for 1D liner code
%    [ss, circ, md, cl] = LINER_STARTUP() returns structure arrays ss,
%    circ, md, cl, which has information about solver setting, circuit,
%    material data, and coil-liner system data respectively.
%
%    See also LinerCompression

% Import Solver Setting
ss = solvdata_import(solvfile);

% Import Circuit Data and Initialize
circ = circ_import(ss.ccf, ss.dpt);

% Import Material Data
md = matdata_import(ss.mdf);

% Import Coil Liner System Configuration
cl = cl_import(ss.clf, ss.dpt);


%Plot Imported Data for Verification
if (cl.case.plt)
    r_temp = linspace(0, cl.r.out(1));
    T_temp1 = linspace(0, md.tlq, 100);
    T_temp2 = linspace(md.tlq, md.Tmx, 100);

    figure(50)
    subplot(2,2,1)
    plot(r_temp, ppval(cl.LSf, r_temp)/1e-9, 'b-', ...
        cl.rwLS(:,1)*cl.r.wall, cl.rwLS(:,2), 'bo')
    hold on
    plot(r_temp, ppval(cl.LLf, r_temp)/1e-9, 'g-', ...
        cl.rwLL(:,1)*cl.r.wall, cl.rwLL(:,2), 'go')
    hold off
    xlabel('r [m]')
    ylabel('L [nH]')
    legend('L_{sys} Fit', 'L_{sys} Data', ...
        'L_{liner} Fit', 'L_{liner} Data', ...
        'Location', 'Best')

    subplot(2,2,3)
    plot(r_temp, ppval(cl.CAf, r_temp), 'b-', ...
        cl.rwCA(:,1)*cl.r.wall, cl.rwCA(:,2), 'bo')
    hold on
    plot(r_temp, ppval(cl.CBf, r_temp), 'g-', ...
```

```
        cl.rwCB(:,1)*cl.r.wall, cl.rwCB(:,2), 'go')
    hold off
    ylim([0,max(cl.rwCA(:,2))])
    xlabel('r [m]')
    ylabel('Field-Flux Parameter [T/Wb]')
    legend('C_A Fit', 'C_A Data', 'C_B Fit', 'C_B Data', ...
        'Location', 'Best')

    subplot(2,2,[2,4])
    plot(T_temp1,ppval(md.T1,T_temp1), 'b-', ...
        md.rw1(:,1), md.rw1(:,2), 'bo', ...
        T_temp2,ppval(md.T2,T_temp2), 'b-', ...
        md.rw2(:,1), md.rw2(:,2), 'bo')
    xlabel('T [K]')
    ylabel('Resistivity [Ohm-m]')
    legend('Fit', 'Data', 'Location', 'Best')

    drawnow
end
```

A.5 solvdata_import.m

```
function out = solvdata_import(file)
% SOLVDATA_IMPORT   Import solver setting for 1D liner code
%    out = SOLVDATA_IMPORT(file) returns structure array with solver
%    configuration information stored in text file.
%
%    See also liner_1d, matdata_import

fileID = fopen(file);

% Skip 2 lines
for i = 1:2
    fgetl(fileID);
end

% Import Time step control case
out.tsc.case = logical(sscanf(fgetl(fileID), '%*s %u'));

% Import Data stream case
out.dts.case = logical(sscanf(fgetl(fileID), '%*s %u'));

fgetl(fileID); % Skip a line

% Import Max allowed data points
out.dpt = sscanf(fgetl(fileID), '%*s %u');

% Import Circuit Configuration File Name
out.ccf = sscanf(fgetl(fileID), '%*s %s');

% Import Material Data File Name
out.mdf = sscanf(fgetl(fileID), '%*s %s');

% Import Coil-Liner system configuration file
out.clf = sscanf(fgetl(fileID), '%*s %s');

fgetl(fileID); % Skip a line

% Import Time step
out.tsc.dt = sscanf(fgetl(fileID), '%*s %f');

% Import Lagrangian Time Step Control Configuration
if (out.tsc.case)
    out.tsc.dtmx = sscanf(fgetl(fileID), '%*s %f');
    out.tsc.dtmn = sscanf(fgetl(fileID), '%*s %f');
    out.tsc.dltB = sscanf(fgetl(fileID), '%*s %f');
    out.tsc.dltT = sscanf(fgetl(fileID), '%*s %f');
end
```

```
% Import Terminal Data stream configuration
if (out.dts.case)
    fgetl(fileID);
    out.dts.psp = sscanf(fgetl(fileID), '%*s %u');
end

fclose(fileID);
end
```

A.6 circ_import.m

```
function out = circ_import(file, datapoints)
% CIRC_IMPORT   Import circuit setting and initialize for 1D liner code
%    out = CIRC_IMPORT(file, datapoints) returns structure array with
%    circuit data initialized with the imported data stored in text file.
%    Arrays are initialized with empty array with length datapoints.
%
%    See also liner_1d, matdata_import

fileID = fopen(file);

% Skip 2 lines
for i = 1:2
    fgetl(fileID);
end

% Import Circuit Solver Function Name
circ_solver = sscanf(fgetl(fileID), '%*s %s');
out.solver = eval(['@', circ_solver]);

if strncmp(circ_solver, 'solv_circ_cbar', 14)
    % Initialize Required Trigger and Arrays
    out.cbtrig = false;
    out.cbtime = 0;
    out.I1 = zeros(1,datapoints);
    out.I2 = zeros(1,datapoints);
    out.I3 = zeros(1,datapoints);
    out.Vc = zeros(1,datapoints);
    out.Ls = zeros(1,datapoints);
    out.Ra = zeros(1,datapoints);

    fgetl(fileID); % Skip a line

    out.Vc(1) = sscanf(fgetl(fileID), '%*s %f') * 1e3;
    out.C     = sscanf(fgetl(fileID), '%*s %f') * 1e-6;
    fgetl(fileID); % Skip a line
    out.R1    = sscanf(fgetl(fileID), '%*s %f') * 1e-3;
    out.R2    = sscanf(fgetl(fileID), '%*s %f') * 1e-3;
    out.R3    = sscanf(fgetl(fileID), '%*s %f') * 1e-3;
    out.Rc    = sscanf(fgetl(fileID), '%*s %f') * 1e-3;
    fgetl(fileID); % Skip a line
    out.L1    = sscanf(fgetl(fileID), '%*s %f') * 1e-9;
    out.L2    = sscanf(fgetl(fileID), '%*s %f') * 1e-9;
    out.L3    = sscanf(fgetl(fileID), '%*s %f') * 1e-9;

end
```

```
fclose(fileID);
end
```

A.7 matdata_import.m

```
function out = matdata_import(file)
% MATDATA_IMPORT   Import material data for 1D liner code
%    out = MATDATA_IMPORT(file) returns structure array with material
%    information stored in text file.
%
%    See also LinerCompression

fileID = fopen(file);

out.material = fgetl(fileID);   % Import Material Name
fgetl(fileID);                  % Skip a line

phase = sscanf(fgetl(fileID),'%*s %u');     % Number of Phase data

out.den = sscanf(fgetl(fileID), '%*s %f');  % Density
out.sus = sscanf(fgetl(fileID), '%*s %f');  % M. Susceptibility
out.tlq = sscanf(fgetl(fileID), '%*s %f');  % Melting Temperature
out.tvp = sscanf(fgetl(fileID), '%*s %f');  % Vaporization Temperature
out.lhf = sscanf(fgetl(fileID), '%*s %f');  % Latent Heat of Fusion
out.lhv = sscanf(fgetl(fileID), '%*s %f');  % Latent Heat of Vaporization
out.sph = sscanf(fgetl(fileID), '%*s %f');  % Specific Heat

% Skip 3 lines
for i = 1:3
    fgetl(fileID);
end

% Extract Temperature Dependent Resistivity Data
for i = 1:phase
    arr_size = 100;
    data = zeros(arr_size,2);
    for j = 1:arr_size
        if feof(fileID)
            data = data(1:j-1,:);
            break
        end

        temp = sscanf(fgetl(fileID), '%f %f');

        if isempty(temp)
            data = data(1:j-1,:);
            break
        end

        data(j,:) = temp;
    end
```

```
    out.(['T',num2str(i)]) = pchip(data(:,1),data(:,2));
    out.(['rw',num2str(i)]) = data;

    % Skip 2 lines
    fgetl(fileID); fgetl(fileID);
end

out.Tmx = max(out.(['rw',num2str(i)])(:,1));
out.Tmn = min(out.rw1(:,1));

fclose(fileID);

end
```

A.8 cl_import.m

```
function out = cl_import(file, datapoints)
% CL_IMPORT   Import Coil-Liner setting and initialize for 1D liner code
%    out = CL_IMPORT(file, datapoints) returns structure array with
%    Coil-Liner system data initialized with the imported data stored in
%    text file. Arrays are initialized with empty array with length
%    datapoints.
%
%    See also liner_1d, solvdata_import, matdata_import

% Initialize
out.r.out = zeros(1,datapoints);
out.r.in  = zeros(1,datapoints);
out.th  = zeros(1,datapoints);
out.v = zeros(1,datapoints);
out.F  = zeros(1,datapoints);
out.CA  = zeros(1,datapoints);
out.CB  = zeros(1,datapoints);
out.T = zeros(1, datapoints);
out.sys.L = zeros(1, datapoints);
out.liner.I = zeros(1,datapoints);
out.liner.R = zeros(1,datapoints);
out.liner.L = zeros(1,datapoints);
out.liner.rstv = zeros(1,datapoints);
out.flux.out = zeros(1,datapoints);
out.flux.in = zeros(1,datapoints);
out.B.out = zeros(1,datapoints);
out.B.in = zeros(1,datapoints);


fileID = fopen(file);

% Skip 2 lines
for i = 1:2
    fgetl(fileID);
end

% Import Vacuum Case Setting
out.case.vacuum = logical(sscanf(fgetl(fileID), '%*s %u'));

% Import Thermal Resistivity Setting
out.case.TdepR = logical(sscanf(fgetl(fileID), '%*s %u'));

% Import System Inductance Setting
out.case.Lsys = logical(sscanf(fgetl(fileID), '%*s %u'));

% Import Liner Inductance Setting
```

```
out.case.Llin = logical(sscanf(fgetl(fileID), '%*s %u'));

% Import Flux-Field System Coefficient Setting
out.case.ffsys = logical(sscanf(fgetl(fileID), '%*s %u'));

% Import Flux-Field Liner Coefficient Setting
out.case.fflin = logical(sscanf(fgetl(fileID), '%*s %u'));

% Import Plotting option for imported data
out.case.plt = logical(sscanf(fgetl(fileID), '%*s %u'));

fgetl(fileID);  % Skip a Line

% Import Coil Liner System Geometry
out.r.wall = sscanf(fgetl(fileID), '%*s %f') / 100;     % Wall Radius
out.r.out(1) = sscanf(fgetl(fileID), '%*s %f') / 100;   % Initial R_out
out.th(1) = sscanf(fgetl(fileID), '%*s %f') * 25.4e-6;  % Initial Thickness
out.w = sscanf(fgetl(fileID), '%*s %f') /100;                % Liner Length

out.r.in(1) = out.r.out(1) - out.th(1);

fgetl(fileID);  % Skip a Line

% Import Initial Condition
out.T(1) = sscanf(fgetl(fileID), '%*s %f');          % Initial Temperature
out.flux.in(1) = sscanf(fgetl(fileID), '%*s %f');    % Initial Inner Bias

if feof(fileID)
    return
end

fgetl(fileID);  % Skip a Line

if (out.case.Lsys)
    % Skip 3 lines
    for i = 1:3
        fgetl(fileID);
    end

    arr_size = 100;
    data = zeros(arr_size,2);
    for j = 1:arr_size
        if feof(fileID)
            data = data(1:j-1,:);
            break
        end

        temp = sscanf(fgetl(fileID), '%f %f');

        if isempty(temp)
```

```
            data = data(1:j-1,:);
            break
        end

        data(j,:) = temp;
    end

    out.LSf = pchip(data(:,1)*out.r.wall,data(:,2)*1e-9);
    out.rwLS = data;
end

if (out.case.Llin)
    % Skip 3 lines
    for i = 1:3
        fgetl(fileID);
    end

    arr_size = 100;
    data = zeros(arr_size,2);
    for j = 1:arr_size
        if feof(fileID)
            data = data(1:j-1,:);
            break
        end

        temp = sscanf(fgetl(fileID), '%f %f');

        if isempty(temp)
            data = data(1:j-1,:);
            break
        end

        data(j,:) = temp;
    end
    out.LLf = pchip(data(:,1)*out.r.wall,data(:,2)*1e-9);
    out.rwLL = data;
end

if (out.case.ffsys)
    % Skip 3 lines
    for i = 1:3
        fgetl(fileID);
    end

    arr_size = 100;
    data = zeros(arr_size,2);
    for j = 1:arr_size
        if feof(fileID)
            data = data(1:j-1,:);
            break
```

```
        end

        temp = sscanf(fgetl(fileID), '%f %f');

        if isempty(temp)
            data = data(1:j-1,:);
            break
        end

        data(j,:) = temp;
    end
    out.CAf = pchip(data(:,1)*out.r.wall,data(:,2));
    out.rwCA = data;
end

if (out.case.fflin)
    % Skip 3 lines
    for i = 1:3
        fgetl(fileID);
    end

    arr_size = 100;
    data = zeros(arr_size,2);
    for j = 1:arr_size
        if feof(fileID)
            data = data(1:j-1,:);
            break
        end

        temp = sscanf(fgetl(fileID), '%f %f');

        if isempty(temp)
            data = data(1:j-1,:);
            break
        end

        data(j,:) = temp;
    end
    out.CBf = pchip(data(:,1)*out.r.wall,data(:,2));
    out.rwCB = data;
end
```

A.9 liner_init.m

```
function [circ, cl, E] = liner_init(circ, cl, md, datapoints)
% LINER_INIT   Initialize for 1D liner code
%    [circ, cl] = LINER_INIT(circ, cl, md, ss) Initialize circ and cl
%    structure array for time dependent calculations.
%
%    See also liner_1d

cl.m0 = md.den * pi * (cl.r.out(1)^2 - cl.r.in(1)^2) * cl.w;
cl.m = cl.m0;

if cl.T(1) <= md.tlq
    cl.liner.rstv(1) = ppval(md.T1, cl.T(1));
elseif cl.T(1) > md.tlq
    cl.liner.rstv(1) = ppval(md.T2, cl.T(1));
end

circ.Ls(1) = ppval(cl.LSf, cl.r.out(1));
cl.liner.L(1) = ppval(cl.LLf, cl.r.out(1));
cl.liner.R(1) = cl.liner.rstv(1) * (pi/cl.w) * (cl.r.out(1)+cl.r.in(1)) ...
    / (cl.r.out(1)-cl.r.in(1));
cl.CA(1) = ppval(cl.CAf,cl.r.out(1));
if (cl.r.in(1)/cl.r.wall <= 0.01)
    cl.CB(1) = 1/(pi*cl.r.in(1)) + ppval(cl.CBf,0.01*cl.r.wall) ...
        - (0.01^2)/(pi*(cl.r.wall^2));
else
    cl.CB(1) = ppval(cl.CBf, cl.r.in(1));
end
cl.B.in(1) = cl.flux.in(1) * cl.CB(1);

circ.Ra(1) = 0;


% Energy
E.tot.circ = zeros(1,datapoints);
E.tot.tot = zeros(1,datapoints);
E.tot.sys = zeros(1,datapoints);

E.circ.C = zeros(1,datapoints);
E.circ.R1 = zeros(1,datapoints);
E.circ.R2 = zeros(1,datapoints);
E.circ.R3 = zeros(1,datapoints);
E.circ.Rc = zeros(1,datapoints);
E.circ.L1 = zeros(1,datapoints);
E.circ.L2 = zeros(1,datapoints);
E.circ.L3 = zeros(1,datapoints);
```

```
E.sys.KE = zeros(1,datapoints);
E.sys.out = zeros(1,datapoints);
E.sys.in = zeros(1,datapoints);
E.sys.loss = zeros(1,datapoints);
E.sys.an = zeros(1,datapoints);
E.sys.tot = zeros(1,datapoints);

E.sysc.dL = zeros(1,datapoints);
E.sysc.L = zeros(1,datapoints);
E.sysc.R = zeros(1,datapoints);

E.error = zeros(1,datapoints);

E.circ.C(1) = 0.5*circ.C*(circ.Vc(1)^2);
E.tot.circ(1) = E.circ.C(1);
E.sys.in(1) = 0.5 * cl.flux.in(1)^2 / cl.liner.L(1);
E.tot.sys(1) = E.sys.in(1);
E.tot.tot(1) = E.tot.sys(1) + E.tot.circ(1);

E.sys.dKE = zeros(1,datapoints);
E.circ.sys = zeros(1,datapoints);

end
```

A.10 plot_liner.m

```
function plot_liner(t, circ, cl, E, n)
figure(1)
[AX,H1,H2] = plotyy([t(1:n-1)',t(1:n-1)', t(1:n-1)'], ...
    [circ.I1(1:n-1)', circ.I2(1:n-1)', circ.I3(1:n-1)'], ...
    [t(1:n-1)'], [circ.Vc(1:n-1)']);
set(get(AX(1),'Ylabel'),'String','Current (A)')
set(get(AX(2),'Ylabel'),'String','Voltage (V)')
xlabel('Time (s)')
set(H1(1), 'DisplayName','I_{1}')
set(H1(2), 'DisplayName','I_{2}')
set(H1(3), 'DisplayName','I_{3}')
set(H2(1), 'DisplayName','V_{cap}')
set(AX(1), 'YLim',[-16e5 32e5])
set(AX(2), 'YLim',[-40e3 80e3])
legend(gca,'show')
grid on

figure(2)
subplot(2,1,1)
plot(t(1:n-1),cl.F(1:n-1),'b-')
xlabel('Time [sec]')
ylabel('Force [N]')
grid on

subplot(2,1,2)
plot(t(1:n-1), cl.th(1:n-1))
xlabel('Time (s)');
ylabel('Liner Thickness (m)');
grid on


figure(3)
subplot(3,1,1)
plot(t(1:n-1), cl.a(1:n-1))
xlabel('Time (s)');
ylabel('Liner Acceleration (m/s^2)');
grid on

subplot(3,1,2)
plot(t(1:n-1), cl.v(1:n-1))
xlabel('Time (s)');
ylabel('Liner Velocity (m/s)');
grid on

subplot(3,1,3)
plot(t(1:n-1), cl.r.out(1:n-1), 'DisplayName','r_{out}')
```

```
hold all
plot(t(1:n-1), cl.r.in(1:n-1), '-r', 'DisplayName','r_{in}')
% hold off
xlabel('Time (s)');
ylabel('Liner Radius (m)');
legend(gca,'show')
grid on


figure(4)
subplot(3,1,1)
plot(t(1:n-1), cl.p.out(1:n-1), 'b-','DisplayName','p_{out}')
hold all
plot(t(1:n-1), cl.p.in(1:n-1), 'r-','DisplayName','p_{in}')
xlabel('Time (s)');
ylabel('Magnetic Pressure (Pa)');
legend(gca,'show')
grid on

subplot(3,1,2)
plot(t(1:n-1),cl.B.out(1:n-1), '-b', 'DisplayName','B_{out}')
hold all
plot(t(1:n-1),cl.B.in(1:n-1), '-g', 'DisplayName','B_{in}')
xlabel('Time (s)');
ylabel('B-field (T)');
legend(gca,'show')
grid on

subplot(3,1,3)
plot(t(1:n-1),cl.liner.I(1:n-1), '-b', 'DisplayName','I_{liner}')
xlabel('Time (s)');
ylabel('Current (A)');
legend(gca,'show')
grid on

figure(6)
subplot(2,1,1)
plot(t(1:n-1), cl.T(1:n-1))
ylabel('Temperature (K)')
xlabel('Time (s)')
grid on
subplot(2,1,2)
plot(cl.T(1:n-1),cl.liner.rstv(1:n-1))
xlabel('Temperature (K)')
ylabel('Resistivity (Ohm-m)')
grid on

figure(7)
plot(t(1:n-1),cl.flux.net(1:n-1), 'b-','DisplayName','Flux_{net}')
hold all
```

```
plot(t(1:n-1),cl.flux.in(1:n-1), 'g-','DisplayName','Flux_{in}')
plot(t(1:n-1),cl.flux.out(1:n-1), 'r-','DisplayName','Flux_{out}')
plot(t(1:n-1),cl.flux.in(1:n-1)+cl.flux.out(1:n-1), 'c-','DisplayName','Flux_{eff}')
xlabel('Time (sec)');
ylabel('Flux (Wb)');
legend(gca,'show')
grid on

figure(8)
plot(t(1:n-1),E.sys.loss(1:n-1),'r-','DisplayName','E_{loss}')
hold all
plot(t(1:n-1),E.tot.tot(1:n-1),'b-','DisplayName','E_{tot}')
plot(t(1:n-1),E.tot.sys(1:n-1), 'b:', 'DisplayName', 'E_{tot-sys}')
plot(t(1:n-1),E.tot.circ(1:n-1), 'b--', 'DisplayName', 'E_{tot-circ}')
plot(t(1:n-1),E.circ.sys(1:n-1), 'r--', 'DisplayName', 'E_{circ-sys}')
plot(t(1:n-1),E.sys.KE(1:n-1),'g-','DisplayName','E_{KE}')
plot(t(1:n-1),E.sys.in(1:n-1),'g-.','DisplayName','E_{in}')
plot(t(1:n-1),E.circ.Ltot(1:n-1),'m-','DisplayName','E_{ind}')
plot(t(1:n-1),E.circ.Rtot(1:n-1),'y-','DisplayName','E_{ohm}')
plot(t(1:n-1),E.circ.C(1:n-1),'k-','DisplayName','E_{cap}')
plot(t(1:n-1),E.sysc.dL(1:n-1),'m-.','DisplayName','E_{deltaL}')
xlabel('Time [sec]','fontsize',14)
ylabel('Energy [J]','fontsize',14)
legend(gca,'show')
grid on

drawnow

figure(9)
plot(t(1:n-1), 100*(E.circ.sys(1:n-1) - E.sys.tot(1:n-1)) ...
    ./E.tot.tot(1:n-1), 'b-')
hold on
plot(t(1:n-1), 100*E.error(1:n-1)./E.tot.tot(1:n-1), 'r-')
plot(t(1:n-1), 100*(1 - E.tot.tot(1:n-1)./E.tot.tot(1)), 'g-')
hold off
xlabel('Time [sec]','fontsize',14)
ylabel('Energy Error [%]','fontsize',14)
legend('Sys-Energy Error', 'Circuit Error', 'Total Energy Error')
grid on

figure(10)
plot(t(1:n-1), E.circ.sys(1:n-1), 'b-')
hold on
plot(t(1:n-1), E.sys.tot(1:n-1), 'g-')
hold off
xlabel('Time [sec]','fontsize',14)
ylabel('System Energy [J]','fontsize',14)
legend('E Convervation', 'System Internal')
grid on
```

```
figure(11)
plot(t(1:n-1), E.sysc.dL(1:n-1), 'b-')
hold on
plot(t(1:n-1), E.sys.KE(1:n-1), 'g-')
hold off
xlabel('Time [sec]','fontsize',14)
ylabel('Energy [J]','fontsize',14)
legend('dL', 'KE')
grid on

figure(12)
plot(t(1:n-1)/1e-6,E.tot.tot(1:n-1)/1e6,'b-','DisplayName','Total')
hold on
plot(t(1:n-1)/1e-6,E.tot.circ(1:n-1)/1e6, 'r-', 'DisplayName', 'Circuit')
plot(t(1:n-1)/1e-6,E.sys.tot(1:n-1)/1e6, 'g-', 'DisplayName', 'Coil-Liner')
hold off
xlabel('Time [usec]')
ylabel('Energy [MJ]')
title('Summary of Total Energies')
legend(gca,'show')
grid on

figure(13)
plot(t(1:n-1)/1e-6, E.sys.tot(1:n-1)/1e6, 'b-', 'DisplayName', 'Total')
hold on
plot(t(1:n-1)/1e-6, (E.sys.tot(1:n-1) - E.sys.out(1:n-1))/1e6, 'b--', ...
    'DisplayName', 'Transfered')
plot(t(1:n-1)/1e-6, E.sys.KE(1:n-1)/1e6, 'g-', 'DisplayName', 'KE')
plot(t(1:n-1)/1e-6, E.sys.out(1:n-1)/1e6, 'c-', 'DisplayName', 'Out')
plot(t(1:n-1)/1e-6, E.sys.in(1:n-1)/1e6, 'm-', 'DisplayName', 'In')
plot(t(1:n-1)/1e-6, E.sys.loss(1:n-1)/1e6, 'r-', 'DisplayName','Loss')
hold off
xlabel('Time [usec]','fontsize',14)
ylabel('Coil-Liner Energy [MJ]','fontsize',14)
legend(gca, 'show')
grid on

figure(14)
plot(t(1:n-1)/1e-6, E.tot.circ(1:n-1)/1e6, 'b-', 'DisplayName', 'Total')
hold on
plot(t(1:n-1)/1e-6, E.circ.C(1:n-1)/1e6, 'g-', 'DisplayName', 'Cap')
plot(t(1:n-1)/1e-6, E.circ.Ltot(1:n-1)/1e6, 'c-', 'DisplayName', 'Ind')
plot(t(1:n-1)/1e-6, E.circ.Rtot(1:n-1)/1e6, 'r-', 'DisplayName','Ohm')
hold off
xlabel('Time [usec]','fontsize',14)
ylabel('Circuit Energy [MJ]','fontsize',14)
legend(gca, 'show')
grid on

end
```

Appendix B

EXAMPLE INPUT FILES FOR 1D LINER CODE

B.1 solver_setting.txt

```
Solver Configuration File
% -----------------------------------------
Time_step_control: 1
Terminal_Datastream: 1
% -----------------------------------------
Max_datapoints: 40000
Circuit_file: circuit_setting.txt
Material_file: Al1100Data.txt
Coil_Liner_file: coil_liner_setting.txt
% -----------------------------------------
dt: 0.5e-8 [sec]
dtmax: 0.5e-8 [sec]
dtmin: 1e-23 [sec]
deltaB: 0.1 [T]
deltaT: 0.5 [%]
% -----------------------------------------
DisplaySpacing: 200
```

B.2 circuit_setting.txt

```
Circuit Configuration File
% ------------------------------------------
Circuit_Solver: solv_circ_cbar
% ------------------------------------------
Bank_Voltage: 40 [kV]
Bank_Capacitance: 2250 [uF]
% ------------------------------------------
Resistance_1: 1.0000 [mOhm]
Resistance_2: 1.0000 [mOhm]
Resistance_3: 1.0000 [mOhm]
Resistance_c: 0.5000 [mOhm]
% ------------------------------------------
Inductance_1: 25   [nH]
Inductance_2: 20   [nH]
Inductance_3: 20 [nH]
```

B.3 LiData.txt

```
Aluminum 1100
% --------------------------------------------
Phase: 2
Mass_Density: 535  [kg/m^3]
M_Susceptibility: 2.1e-5 []
Temp_Liquid: 453.7 [K]
Temp_Vapor: 1615 [K]
Latent_Heat_Fusion: 422000 [J/kg]
Latent_Heat_Vapor: 19600000    [J/kg]
Specific_Heat: 3570 [J/kg-K]
% --------------------------------------------
Temp [k] restv [ohm/m]
% --------------------------------------------
1 7.24E-11
2 7.24E-11
3 2.75E-11
4 7.27E-11
5 7.30E-11
6 7.35E-11
7 7.40E-11
8 7.45E-11
9 7.51E-11
10 7.60E-11
11 7.73E-11
12 7.92E-11
13 8.17E-11
14 8.49E-11
15 8.89E-11
16 9.36E-11
18 1.06E-10
20 1.22E-10
25 1.85E-10
30 3E-10
35 4.7E-10
40 7.4E-10
45 1.09E-09
50 1.62E-09
60 3.45E-09
70 6.36E-09
```

```
80 0.00000001
90 1.36E-08
100 1.73E-08
150 3.72E-08
200 5.71E-08
250 7.65E-08
273.15 8.53E-08
293 9.28E-08
300 9.55E-08
350 1.145E-07
400 0.000000134
450 1.544E-07
453.7 1.559E-07
% --------------------------------------------
Temp [k] restv [ohm/m]
% --------------------------------------------
453.7 0.000000248
500 2.633E-07
600 2.934E-07
700 0.000000321
800 3.471E-07
900 3.722E-07
1000 3.922E-07
1100 4.213E-07
1200 4.461E-07
1300 4.741E-07
1400 4.997E-07
1500 0.00000053
1600 5.634E-07
1700 6.003E-07
```

B.4 coil_liner_setting.txt

```
Coil-Liner System Configuration File
% ------------------------------------------
Vacuum_Case: 0
Thermal_rstv: 1
Inductance_sys: 1
Inductance_liner: 1
Flux_field_sys: 1
Flux_field_liner: 1
plot_import_data: 0
% ------------------------------------------
r_wall: 15 [cm]
r_out: 14.5 [cm]
thickness: 30 [mil]
width: 15 [cm]
% ------------------------------------------
Temperature: 300 [K]
InnerBias: 0 [Wb]
% ------------------------------------------
% Data for System Inductance
r_out/r_wall Inductance [nH]
% ------------------------------------------
0.983333333 37.14394
0.966666667 59.24958
0.950000000 77.46428
0.933333333 93.06807
0.900000000 121.5405
0.866666667 142.8396
0.800000000 178.4958
0.733333333 204.7758
0.666666667 226.9295
0.533333333 256.3855
0.400000000 275.5054
0.266666667 286.7861
0.133333333 293.1707
0.000000000 287.2310
% ------------------------------------------
% Data for Liner Inductance
r_out/r_wall Inductance [nH]
% ------------------------------------------
```

```
0.983333333 313
0.966666667 304
0.950000000 297
0.933333333 289
0.900000000 273
0.866666667 258
0.800000000 227
0.733333333 199
0.666666667 170
0.533333333 118
0.400000000 72.9
0.266666667 35.1
0.133333333 7.65
0.000000000 0.00
% ------------------------------------------
% Data for shorted Field-Flux Coefficient
r_out/r_wall Field-Flux [T/Wb]
% ------------------------------------------
0.983333333 427.631604
0.966666667 215.9688288
0.950000000 145.5312086
0.933333333 110.3283664
0.900000000 75.09558457
0.866666667 57.42549833
0.800000000 39.56074934
0.733333333 30.38224844
0.666666667 23.95810844
0.533333333 16.16647098
0.400000000 10.56584222
0.266666667 6.424762755
0.133333333 3.902968395
0.066666667 3.122950588
0.033333333 2.896153239
0.013333333 2.834194432
0.006666667 2.82696229
0.000000000 2.528298491
% ------------------------------------------
% Data for Liner Field-Flux Coefficient
r_out/r_wall Field-Flux [T/Wb]
% ------------------------------------------
0.983333333 31.82061404
```

```
0.966666667 32.54636129
0.950000000 33.30505271
0.933333333 34.09888323
0.900000000 35.8017565
0.866666667 37.67695864
0.800000000 42.05612139
0.733333333 47.52808302
0.666666667 54.54479507
0.533333333 76.61739346
0.400000000 123.0351306
0.333333333 168.8666166
0.266666667 252.0643689
0.200000000 428.4219391
0.133333333 915.3818553
0.100000000 1576.84563
0.083333333 2231.278158
0.066666667 3422.044175
0.033333333 13151.3015
0.023333333 26519.51915
0.013333333 80321.75717
0.010000000 142325.5027
0.006666667 319285.3739
```